Rolf Bjordal
Henrik Rekdal Eidheim

Assessment of Dynamic Properties of Five Multi-Storey CLT Buildings in Operational Conditions

Master's thesis

NTNU
Norwegian University of
Science and Technology

Rolf Bjordal
Henrik Rekdal Eidheim

Assessment of Dynamic Properties of Five Multi-Storey CLT Buildings in Operational Conditions

NTNU
Norwegian University of
Science and Technology

Department of Structural Engineering
Faculty of Engineering
NTNU- Norwegian University of Science and Technology

MASTER'S THESIS 2022

SUBJECT AREA:	DATE:	NO. OF PAGES:
Timber structures, Dynamics	June, 11th 2022	159

TITLE:

Assessment of Dynamic Properties of Five Multi-Storey CLT Buildings in Operational Conditions
Vurdering av dynamiske egenskaper til fem fleretasjes massivtrebygninger i drift

BY:

Rolf Bjordal & Henrik Rekdal Eidheim

SUMMARY:

The goal of this master's thesis is to evaluate the dynamic properties of five multi-storey Cross Liminated Timber (CLT) buildings. The chosen buildings for this thesis are the five 9-storey student housings at Moholt, Trondheim. There are rarely five identical buildings in CLT, so this is a unique possibility. The buildings are in operational conditions and subjected to ambient vibration. The buildings are measured, which results in acceleration time series. In these acceleration time series, it is possible to obtain dynamic properties with Operational Modal Analysis (OMA). The dynamic properties are compared to a prepared numerical model.

The use of four Kistler accelerometers has measured the buildings. The measured data is analysed with OMA, specifically the Data-Driven Stochastic Subspace Identification (DD-SSI). From this, dynamic properties are obtained; natural frequencies, damping, and mode shapes. These methods use output-only identification, where the acceleration data is the output.

A numerical model is established to compare with the measured data. The numerical model is designed with the FE-software Abaqus. From Abaqus, the natural frequencies and mode shape are extracted. The numerical model is changed and iterated based on the comparisons to find a solution that matches best.

The peak acceleration is a critical value in tall timber buildings. Due to the material properties of timber compared to steel and concrete, tall timber buildings are easier subjected to uncomfortable accelerations. ISO10137 [1] has recommendations for peak accelerations that a building should satisfy. In addition to measured peak accelerations, calculations of peak acceleration based on NS-EN 1991-1-4 [2] are conducted and compared with the recommendation in ISO10137.

The work done in this thesis shows no significant deviations in the dynamic properties obtained from the experimental results between the five buildings. Peak accelerations fluctuate more between the buildings, most likely because of a difference in wind load. The calculated peak accelerations were significantly higher than the measured ones, but all values were well within the recommendation in ISO10137. The numerical model was able to replicate the experimental to a satisfying degree, but it was not an exceptional representation.

RESPONSIBLE TEACHER:	Kjell Arne Malo
SUPERVISOR(S):	Kjell Arne Malo, Saule Tulebekova
CARRIED OUT AT:	Department of Structural Engineering, NTNU

Preface

This master's thesis is completed during the spring semester of 2022 and marks the end of the two-year master's program in Civil and Environmental Engineering at NTNU in Trondheim. The work presented is the result of 20 weeks of work and corresponds to 30 credits.

The master's thesis is carried out at the Department of Structural Engineering under the Faculty of Engineering Science and Technology at NTNU. The framework of the assignment was proposed to us by the Department, with similar experiments on other buildings conducted in the past. During the process, measurement equipment, data processing, and numerical software have been used. Having no earlier experiences with the former two, a steep learning curve is now starting to show results.
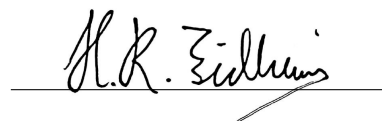
Our supervisors have been of great help, and this thesis would not be possible without them. Kjell Arne Malo for valuable guidance and support both in person and in the progress of the work. Saule Tulebekova, for a thorough help with the measurement equipment, data processing, numerical model, and everything in between.

Finally, we are grateful to the Student Welfare Organisation in Trondheim for their collaboration and letting their buildings be the object of research and Woodplan for their cooperation and helpfulness with the structural system.

For future research, we gladly allow all material from this thesis to be used and hope that it can contribute to a future with more timber.

Rolf Bjordal

Henrik Rekdal Eidheim

Trondheim, 10th June 2022

Abstract

The goal of this master's thesis is to evaluate the dynamic properties of five multi-storey Cross Laminated Timber (CLT) buildings. The chosen buildings for this thesis are the five 9-storey student housings at Moholt, Trondheim. There are rarely five identical buildings in CLT, so this is a unique possibility. The buildings are in operational conditions and subjected to ambient vibration. The buildings are measured, which results in acceleration time series. In these acceleration time series, it is possible to obtain dynamic properties with Operational Modal Analysis (OMA). The dynamic properties are compared to a prepared numerical model.

The use of four Kistler accelerometers has measured the buildings. The measured data is analysed with OMA, specifically the Data-Driven Stochastic Subspace Identification (DD-SSI). From this, dynamic properties are obtained; natural frequencies, damping, and mode shapes. These methods use output-only identification, where the acceleration data is the output.

A numerical model is established to compare with the measured data. The numerical model is designed with the FE-software Abaqus. From Abaqus, the natural frequencies and mode shape are extracted. The numerical model is changed and iterated based on the comparisons to find a solution that matches best.

The peak acceleration is a critical value in tall timber buildings. Due to the material properties of timber compared to steel and concrete, tall timber buildings are easier subjected to uncomfortable accelerations. ISO10137 [1] has recommendations for peak accelerations that a building should satisfy. In addition to measured peak accelerations, calculations of peak acceleration based on NS-EN 1991-1-4 [2] are conducted and compared with the recommendation in ISO10137.

The work done in this thesis shows no significant deviations in the dynamic properties obtained from the experimental results between the five buildings. Peak accelerations fluctuate more between the buildings, most likely because of a difference in wind load. The calculated peak accelerations were significantly higher than the measured ones, but all values were well within the recommendation in ISO10137. The numerical model was able to replicate the experimental to a satisfying degree, but it was not an exceptional representation.

Sammendrag

Målet med denne masteroppgaven er å evaluere de dynamiske egenskapene til en fleretasjes massivtrebygning. De valgte bygningene for denne oppgaven er de fem 9-etasjers studenthyblene på Moholt, Trondheim. Det er sjeldent fem identiske bygninger i massivtre, så dette er en unik mulighet. Bygningene er målt under driftsmessige forhold og utsatt for laster fra omgivelsene. Målingene resulterer i akselerasjonsdataserier. Med disse akselerasjonsseriene er det mulig å finne de dynamiske egenskapene. De dynamiske egenskapene sammenlignes med en utarbeidet numerisk modell.

For å måle bygningene er det brukt fire Kistler-akselerometre. De målte dataene er analysert ved hjelp av Operational Modal Analysis (OMA), mer spesifikt Data-Driven Stochastic Subspace Identification (DD-SSI). Disse metodene identifiserer de dynamiske egenskapene kun ved hjelp av utdata. Ved hjelp av denne metoden er naturlige frekvenser, demping og svingformer funnet.

En numerisk modell er etablert for å sammenligne med de målte verdiene. Den numeriske modellen er designet med FE-programvaren Abaqus. Fra Abaqus hentes de naturlige frekvensene og svingformene. Den numeriske modellen endres og itereres basert på MAC-sammenligningene for å finne en løsning som representer bygningene best.

Toppakselerasjonen er en kritisk verdi i høye trebygg. På grunn av materialegenskapene til tre sammenlignet med stål og betong, er de mer utsatt for ubehagelige akselerasjoner. ISO 10137 [1] har anbefalinger for toppakselerasjoner som et bygg bør tilfredsstille. Toppakselerasjonen fra de eksperimentelle dataene målt i bygningene er sammenlignet med anbefalingen i ISO 10137. I tillegg er toppakselerasjoner beregnet basert på prosedyrer i Eurokoden [2] for å sammenligne med målte akselerasjoner og anbefalingen i ISO10137.

Arbeidet som er gjort i denne oppgaven viser ingen signifikante avvik i de dynamiske egenskapene mellom de fem bygningene. Toppakselerasjoner varierer mer mellom bygningene, mest sannsynlig på grunn av en forskjell i vindbelastning. De beregnede toppakselerasjonene var betydelig høyere enn de målte, men alle verdier var godt innenfor anbefalingen i ISO10137. Den numeriske modellen var i stand til å gjenskape det eksperimentelle i en tilfredsstillende grad, men det var ikke en eksepsjonell representasjon.

List of Abbreviations

ADC Analog-to-Digital Converter. 39

BC Boundary conditions. 70

CLT Cross Laminated Timber. ii, 1

Cov-SSI Covariance Driven Stochastic Subspace Identification. 60

cRIO CompactRIO. 31

DC Direct Current. 60

DD-SSI Data-Driven Stochastic Subspace Identification. ii, iii, 19

DOF Degree of Freedom. 11

EMA Experimental Modal Analysis. 10

EWP Engineered Wood Products. 4

FEA Finite Element Analysis. 45

FFT Fast Fourier Transform. 27

FIR Finite Impulse Response. 41

FPGA Field-Programmable Gate Array. 31

Glulam Glued Laminated Timber. 1

I/O module Input Output Module. 31

MAC Modal Assurance Criterion. 24

MDOF Multi Degree of Freedom. 11

MPCW Weighted Modal Phase Collinearity. 23

NTNU Norwegian University of Science and Technology. 1

ODS Operational Deflection Shapes. 10

OMA Operational Modal Analysis. ii, iii, 10

PSD Power Spectral Density. 3, 20

SD Standard Deviation. 56

SHM Structural Health Monitoring. 11

SiT Student Welfare Organisation in Trondheim. 2

SSD Solid State Drive. 31

SSI Stochastic Subspace Identification. 16

SVD Singular Value Decomposition. 19

tdms Technical Data Management Streaming. 41

ZOH Zero Order Hold. 15

List of Symbols

Operational Modal Analysis

$\mathbf{M}$; $\mathbf{C}$; $\mathbf{K}$	System Mass-, Damping, and Stiffness matrix
$\boldsymbol{f}(\mathrm{t})$	Force vector
$\boldsymbol{y}$; $\boldsymbol{y}_k$	Continuous- and Discrete time output vector
$\boldsymbol{q}$	Amplitude
ω_n	Natural frequency
ω_d	Damped natural frequency
ξ	Modal damping ratio
ϕ_n	Eigenvector
$\bar{\mathbf{B}}$	Location matrix of inputs
$\boldsymbol{u}(t)$	Discrete time variations of sampled input
$\boldsymbol{s}(t)$; $\boldsymbol{s}_k$	Continuous- and Discrete time state vector
$\boldsymbol{I}$	Identity matrix
$\mathbf{A}_c$; $\mathbf{A}$	Continuous- and Discrete time state matrix
$\mathbf{B}_c$; $\mathbf{B}$	Continuous- and Discrete time input matrix
$\mathbf{C}_a$; $\mathbf{C}_y$; $\mathbf{C}_d$	Displacement-, Velocity, and acceleration output location matrices
$\mathbf{C}_c$; $\mathbf{C}$	Continuous- and Discrete time output matrix
$\mathbf{D}_c$; $\mathbf{D}$	Continuous- and Discrete time direct transmission matrix
$\boldsymbol{v}_k$; $\boldsymbol{w}_k$	Measurement- and Process noise
$E\ []$	Expected value operator
$\mathbf{Q}^{ww}$; $\mathbf{S}^{wv}$; $\mathbf{R}^{vv}$	Covariance matrices of process- and measurement noise
ε_k	State prediction error
$\hat{\boldsymbol{s}}_k$	Kalman state estimate at time instant k

$\hat{\boldsymbol{y}}_k$	Predicted measurements matrix
$\boldsymbol{e}_k$	Innovation
$\mathbf{P}_k$	Algebraic Riccati equation / steady state Kalman state covariance matrix
$\mathbf{K}_k$	Steady state Kalman gain
$\mathbf{Y}_p$; $\mathbf{Y}_f$	Matrices of past- and future outputs
$\mathbf{Y}_p^+$; $\mathbf{Y}_f^-$	Matrices of past- and future outputs with one block row added / removed
$\mathbf{P}_i$	Projection matrix of future outputs onto past outputs
$\mathbf{L}$; $\mathbf{Q}$	Lower triangular matrix and orthonormal matrix in $\mathbf{LQ}$ decomposition
$\mathbf{U}_1$; $\boldsymbol{\Sigma}_1$; $\mathbf{V}_1$	Matrices in the Singular Value Decomposition
$\mathbf{O}_i$	Observability matrix
$\mathbf{O}_1^\uparrow$	Observability matrix with last l rows deleted
$\mathbf{O}_i^+$	Observability matrix with one block row added
$\hat{\mathbf{S}}_i$	Kalman filter state space sequence
ρ_w; ρ_v	Kalman filter residuals matrices
Δt	Sampling period
t_k	Time step
$\mathbf{z}(t)$	Whitened data

Data Processing

f_a	Alias frequency
f_c	Cut-off limit of filtered frequency
f_N	Nyquist frequency
f_s	Sampling frequency
$f_{N,dec}$	New Nyquist frequency after decimation
$f_{s,dec}$	Decimated sampling frequency
Q	Decimation factor

Table of Contents

List of Tables

List of Figures

Chapter 1

Introduction

Today, the world is experiencing a trend of change toward a greener and more eco-friendly earth. As global warming continues to cause increasingly significant problems, reducing global emissions is viewed as an important solution. In most industries, there is now an increasingly focus on how to achieve this. There are several ways to help with this in the construction industry. Thanks to new and better technology, this goal is now more achievable than before. One of these solutions is timber structures.

Timber structures are nothing new and have been used for centuries, but high rise timber structures have been rare and limited by past technology. There have been several challenges that have prevented this. Limitations in material technology and structural properties created challenges that can be solved today, with more and higher timber buildings being built. Driven forward by new load-bearing materials in Cross Laminated Timber (CLT) and Glued Laminated Timber (Glulam) combined with research about the challenges, developers now have a great alternative to the traditional materials steel and concrete for high-rise buildings.

1.1   Choice of subject

Dynamic properties in tall timber buildings have been the subject of theses and papers for the last decade at NTNU. It is important to continue working with dynamic properties in tall timber buildings to understand better how the buildings behave with different configurations under several conditions. Thus improving knowledge for future civil engineers and making it possible to build more efficient and higher structures in timber.

In this master's thesis, the subject is to study the dynamic behaviour of five almost identical high-rise buildings made of CLT during operational conditions. The thesis was proposed by the Department of Structural Engineering at the Norwegian University of Science and Technology (NTNU). NTNU has contributed with equipment, script codes, and guidance. Research by NTNU has been conducted on several of

Norway's tallest timber buildings. For an interested reader, earlier work is accessible for the Glulam building Treet in Bergen [3], [4], CLT building Smørbukklia in Tromsø [5], and the tallest timber building in the world Mjøstårnet in Brummundal [6]. The earlier work at NTNU included research on Moholt 50|50, but only one building was measured during the later stages of the construction phase [4]. The buildings at Moholt are still interesting because there are five similar buildings at the same spot, and they are now in operational conditions. With tall timber buildings, it is infrequent, if not unique, to have the opportunity to compare five this similar buildings.

1.2 Moholt student village

Moholt student village is one of many student housings provided by the Student Welfare Organisation in Trondheim (SiT). It is located at Moholt in the southeastern part of Trondheim and is Trondheim's largest student village [7]. The village consists of numerous buildings, mostly in bricks, in which the first students were accommodated in 1965. The newest addition to the building mass is the project dubbed Moholt 50|50.

1.2.1 Moholt 50|50

Figure 1.1: Overview Moholt Allmenning. Reproduced with permission [8] Photo: Frode Vigtil

In recognition of the 50th anniversary of the Moholt student village, the Moholt 50|50 project was completed in December of 2016. It consists of five Y-shaped towers which primarily house students and a two-story hub in the centre which houses a library. The towers consist of nine storeys and a basement, where the top eight storeys are made of CLT, and the ground storey and basement are made of concrete. All five towers are identical from the second storey and up. The concrete storeys have different interior layouts from tower to tower depending on which function it houses, which varies from training facilities, stores, apartments, launderette, and medical offices.

An Austrian company, named Woodplan, was involved in the design process of Moholt 50|50. They were also involved in this process, and submitted information, plan views, and answered question about details in the buildings.

1.3   Structure of thesis

This thesis covers multiple different topics. The second chapter contains timber theory. This includes general information about timber, but the chapter is directed toward multi-storey CLT buildings. The third chapter explains the method used to measure the buildings and the hardware used in this process, including the challenges and solutions. In the fourth chapter, there is the theory behind OMA and its implementation for the Moholt buildings. The fifth chapter describes data processing, with a presentation of pitfalls and how they were avoided in this thesis. The sixth chapter describes why and how the numerical model is designed. There is information about the buildings' elements and materials in this chapter. The seventh chapter is designated for the experimental result. It includes natural frequencies, Power Spectral Density (PSD), damping, peak accelerations, and mode shapes. The eighth chapter presents the results from the numerical model and Eurocode calculations. This chapter includes natural frequencies, peak accelerations, and theoretical and numerical mode shapes with illustrations. The ninth chapter discusses the thesis, what can be concluded, and which uncertainties are left. The tenth and last chapter is the conclusion, with some ideas for further work.

Chapter 2

Timber

Timber is a material with a wide range of applications. Timber is a historically significant material, but the industrial revolution led to steel and concrete superseding timber as the preferred material. However, timber has been significantly used in low buildings in the present and the past, and in recent years timber has been more used in tall buildings. Timber is a material that is easily accessible in many countries and is easily manipulated to create advantageous shapes and dimensions. For modern buildings, Engineered Wood Products (EWP) have created new possibilities in how timber is utilised today. EWP is tailor-made for its purpose, and the physical properties have been optimised [9]. The most suitable EWP for taller buildings are Glulam and CLT [9].

The new and better technology in EWP means that the timber products have less variation in quality compared to pure timber, which optimises the material expense [9]. Improved timber products greatly benefit a world in a new direction, where sustainability is more prioritised than before. Compared to concrete, which is known as an environmental problem and quoted to be the third-largest source of anthropogenic emissions of carbon dioxide [10], timber has shown to be a greener material. By substituting concrete and steel with timber, the emissions can be reduced on average by 69% in the construction phase [11]. The technical advancement and the pursuit for a more sustainable future lead to more and higher buildings being built in timber or with timber combined with other materials.

2.1   EWP

In the 1990s, the development of CLT started in Central Europe. It has since spread to Scandinavia, the US, Canada, and other European countries [12]. CLT and Glulam are timber laminates glued together. What separates CLT from Glulam is the angle between the laminates. The angle is the difference between laminate grain directions. Glulam has laminates with a parallel grain direction, whereas CLT has laminates with an angle between the grain directions. The angle is usually 90 degrees, but other preferable angles can be utilised, e.g. 45 degrees. The cross

lamination gives CLT elements strength properties suitable for different uses, e.g. floors and walls, whereas Glulam is suitable for beams and columns. CLT is normally assembled in 3 to 9-layers. The number of layers can depend on the use and thickness of the element.

2.1.1 Cross Laminated Timber

CLT is utilised in houses, multi-storey buildings, and high-rise buildings. CLT can be used for the main structural system or be utilised in cooperation with Glulam or other materials, e.g. concrete and steel [12]. CLT have great flexibility in form, plan, and structures. CLT comes in prefabricated sections and reduces the constructing time [12]. Prefabricated sections are a benefit because CLT should have a weather-protected construction process. The benefit of a protected process is an even and high quality in the executed work, increased productivity and a better work environment[13] [12]. A tent can be installed over the structure to ensure a protected process. However, it is not a requirement for quality, and it has not been used at the construction site of Moholt 50|50, where a dry process would be a great challenge because of the height.
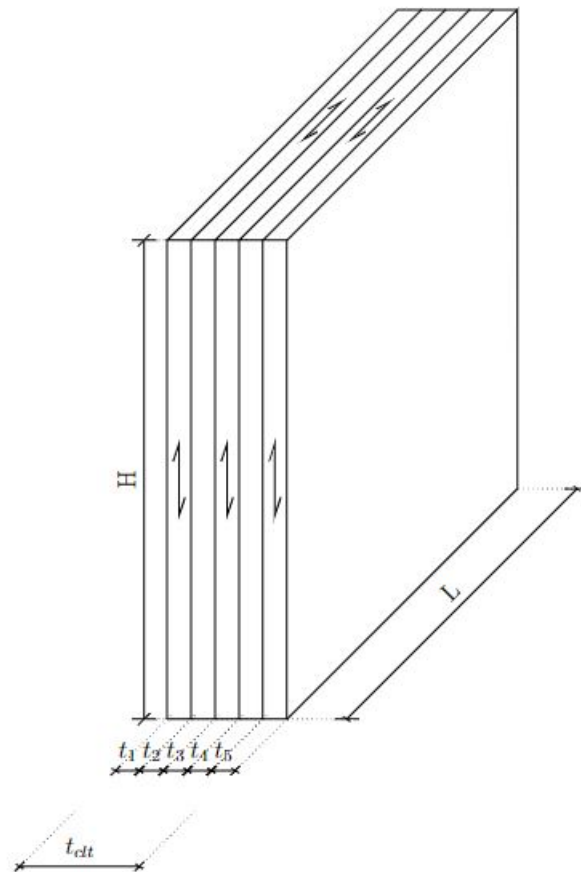
Figure 2.1: 5-layer CLT wall

2.2 CLT for the occupants

For a CLT building, certain areas need to be addressed properly to ensure a comfortable environment for its occupants. The occupants should be safe and unbothered about noise or other unpleasantness. Wood naturally conveys warmth. Thus it is a comfortable material to live with and can be used exposed. CLT is often used exposed on the walls and floors, which creates an effect of a natural environment for the occupants [14].

2.2.1 Fire resistance in CLT

When using CLT in structures, correct design for fire resistance is essential [15]. If the CLT elements can not provide sufficient protection, solutions, e.g. cladding, can help improve safety. Cladding and other safety measures can be utilised, but it is not compulsory to obtain a safe building. In 2020, Polyseam released a handbook named *Fire stopping of service penetrations in timber constructions*, where they deemed CLT unsafe as floors in buildings taller than two storeys [16]. SINTEF, an independent Norwegian research organisation, published a response to the claims of Polyseam and addressed that "*Polyseam misinforms about CLT and fire properties - new 'handbook' is pure product advertisement*" [17]. Well documented fire resistance and charring rate test from COST Action shows that CLT-structures actually can obtain a high fire resistance if designed properly [18].

One of the reasons it can be an effective material against fire is how it is damaged when exposed to fire. Timber is charring under fire which creates two properties [15]. The first is that the charring will serve as a protection against fire and slow down the charring progress further into the timber [15]. The second is that while some part of the cross-section is charring and losing strength, the rest of the material keeps the strength properties [15].

2.2.2 Acoustic performance in CLT

When using CLT, it is important to consider noise and sound insulation in the design process. Timber is a material with low density compared to concrete and steel [19]. The lower density makes timber vibrate easier than a higher density material [19]. The criteria for noise is given by NS 8175 [20] and are dependent of the building's use [20]. It would be clever to be proactive with sound when planning and designing CLT buildings. For instance, limiting exposure of noise that can be avoided, e.g. roads, playgrounds, noise from instalments in the building, and strategic placement of technical rooms.

Furthermore, to limit flanking transmission between rooms and storeys, the intersecting nodes play an essential part [19]. There are often five different acoustic areas that are involved in planning and designing the acoustic of a building: room acoustics, sound from installations, sounds from external sources (e.g. traffic), impact

sound insulation, and airborne sound insulation [15]. The last two are specifically important for timber.

(a) Example of transmission routes for airborne sound [15].

(b) Example of transmission routes for impact sound [15].

Figure 2.2: Sound transmission examples

Fixed connections can be implemented in a static system to increase the stiffness, but it will negatively impact the acoustic performance. The vibration spreads easier with stiffer connections [19]. In Central Europe, there is a tradition of increasing the weight of the floors. This is done with screed (concrete) or other materials such as gravel [21]. The increment in weight makes the element more resistant to vibrations. In principle, there are two ways of limiting flanking transmissions in CLT buildings: separate inner cladding of load-bearing elements, vibration-damping using flanking transmission barriers, or a combination of the two [15]. In the vertical direction, vibrations can be reduced by using flanking transmission barriers. Most often, it involves elastic isolation in the form of strips, called sylomer [15]. The strips go between separate building parts and separate them. It is important that the joint connection still transfer the static forces and absorb any forces of lift [15].

Figure 2.3: Vibration-damping intermediate layer. Photo: [15]

2.3 Dynamics in timber buildings

Timber has a naturally high strength-to-weight ratio. Furthermore, timber has a higher strength-to-weight (C24) ratio than both Steel (S355) and concrete (B35), as presented in table (2.1). The strength-to-weight ratio can be a positive attribute for static problems because it uses less strength to bear its self-weight than concrete and steel. Timber will need a more extensive structural system than concrete and steel to handle the applied loads, but the real problem is the dynamic properties. The dynamic problems are different for the lightweight timber structures. The lighter structures have a lower resistance against accelerations, which can be problematic for the residents' comfort level [22].

There is a criterion for comfort level in ISO 10137 [1] for accelerations. If the initial calculations of a building's peak acceleration surpass this criterion, a common solution is to increase the mass. The calculated value for the criterion in ISO 10137 is coupled with mass and natural frequency. An increment in mass will decrease the natural frequency, but the important factor is that the peak acceleration decreases. There is no independent criterion for natural frequency. The relationship between strength and mass is expressed in section (3.1) in the dynamic formulas.

Concrete decks are a solution to increase the mass of timber truss systems used in Treet in Bergen and Mjøstårnet in Brummundal. In Treet, the decks are named "power storey" and divide apartment modules and act as a base for the modules over the "power storey" [3]. In Mjøstårnet, the upper six floors are made from concrete slabs in contrast to the floors below, which utilise a "Trä8" system [6]. For CLT buildings, additional screed in floors can be a contributing factor to decrease the accelerations.

Table 2.1: Specific strength

Material	Density [kg/m^3]	Young's modulus [MPa]	Specific strength Young's modulus / Density
Concrete (B35)	2500	34 077	≈ 14
Steel (S355)	7800	210 000	27
Timber (C24)	350	11 000	31

Designing a tall building is complex. A taller building will generate larger problems both statically and dynamically. Compared to tall steel and concrete buildings, tall timber buildings have different dynamic properties. One difference is that a timber building is far lower than a steel and concrete building before the dynamic properties create challenges. Especially the low self-weight creates challenges for the acceleration comfort criteria in ISO 10137 [1]. Because of the dynamic behaviour and challenges, a timber building is often referred to as a "tall" building, in height far lower than a "tall" concrete or steel building [23].

A parametric study [24] researched the differences between CLT buildings and Glulam truss system buildings. The study showed that CLT buildings and Glulam truss system buildings have different dynamic properties. One difference is the way the

buildings are moving. A building with a truss system has a larger degree of bending tendency than CLT buildings, which rely more on shear behaviour [24]. The study used parametric conceptual buildings since there are few examples of buildings being built similar enough to compare. Comparing CLT and Glulam buildings is challenging because they are often too different in geometry and height. The conceptual buildings designed in CLT and Glulam were made in similar geometry and with several different height configurations. For the natural frequency, the study showed that CLT buildings and truss-system buildings have a similar first natural frequency when comparing two similar buildings in geometry and height [24]. The mode shapes had some slight differences between the different structure types [24].

The acceleration is coupled with the mass in the systems. The truss system has less weight than a CLT building. However, using equivalent mass, the acceleration can be lower in a truss system than in a CLT building. Therefore, Glulam truss-system buildings can be a better alternative to use in taller timber buildings [24]. There are several methods of calculating equivalent mass, which can be approximated by taking the mass in total and dividing it by the building height. It is crucial to handle this correctly to avoid unrealistic calculations of acceleration [24].

2.4 Damping in CLT

In order to reduce the risk of discomfort, it is best to achieve as high a value as possible for damping [15]. Damping in CLT floors is set by the Eurocode to be 1% [25], unless there are other values proved to be more appropriate. Since the Eurocode only suggests one value, it should be used with caution. The new draft of Eurocode 5 gives more detailed suggestions [26], but this is still a work in progress. The current Eurocode does not set values for damping in walls or other structural elements. There is limited research done for damping in a finished CLT floor. Table 2.2 presents the suggestions of the research.

Table 2.2: Suggested values for relative damping in floor structures made from wood and CLT [15].

Material and composition	Relative damping
Wooden floor structure	1.0%
Bonded boards with cast layer	2.0%
Composite structure with nailed wooden joists and cast layer	3.0%
CLT floor structure with or without additional lightweight top layer, two-sided supported	2.5%
CLT floor structure with cast layer, four-sided supported	3.5%
CLT floor structures with cast layer, four-sided supported on stud wall	4.0%

Chapter 3

Operational Modal Analysis

In several areas of engineering, dynamic properties are of great interest. It can be an automotive engineer designing a driveshaft, an aerospace engineer designing a plane, or a civil engineer designing a building. Civil engineers need to determine mode shapes, damping, accelerations, and natural frequencies. Three ways of discovering dynamic properties are [27]:

- Operational Modal Analysis (OMA) - in operational mode this is used to discover dynamic properties from vibration measurements.

- Experimental Modal Analysis (EMA) - by using the response function measurements by measured or force inputs.

- Operational Deflection Shapes (ODS) - given a operational frequency, that is not needed to be a natural frequency, it analyses the vibration shape.

OMA is the method used to investigate designs that have been executed and are now in operation. This method can not control the input, but it investigates the output. While the two other methods are performed in a laboratory with controlled input and investigate the output [27]. Ambient vibration modal identification and output-only modal analysis are other names for OMA [28]. For civil engineers, OMA is the most often applicable method. It is a method for extracting the resulting mode shaped, damping, and natural frequency. The current FE programs can calculate these values. However, there is still a need for extracting actual values [28], e.g. the need could be to discover if there are critical acceleration values or unexpected mode shapes.

OMA is a method that is derived from the procedures in EMA. Hence the procedures in the two methods share much of the common theoretical basis. The main difference is that OMA input is unknown and random compared to EMA where the input is known [28]. The input in OMA is based on ambient excitation created by the loads, e.g. wind and traffic. The vibration created by ambient excitation is small compared to the excitation created in EMA experiments. Therefore the sensors in OMA need to have high performance and a low noise level [28].

In Structural Health Monitoring (SHM), OMA can be used for health monitoring and damage detection of a building [27], [28]. SHM is used to discover if the dynamic properties change over time or before and after a large load (e.g. earthquake, extreme weather).

This chapter uses the theory and equations from Rainieri and Fabbrocino in the book *Operational Modal Analysis of Civil Engineering Structures* [28], and Van Overschee and De Moor in the book *Subspace Identification For linear System* [29], unless stated otherwise. More detailed explanations and derivations of equations can be found in their work for a better understanding.

3.1   Time Domain

For the time domain, the dynamic equation of equilibrium for a Multi Degree of Freedom (MDOF) system is described by the following:

$$\mathbf{M}\ddot{\boldsymbol{y}}(t) + \mathbf{C}\dot{\boldsymbol{y}}(t) + \mathbf{K}\boldsymbol{y}(t) = \boldsymbol{f}(t) \tag{3.1}$$

The constants $\mathbf{M}$, $\mathbf{C}$, $\mathbf{K}$ are the mass, damping, and stiffness matrix. $\boldsymbol{y}$ represents the displacement in respect to time and $\boldsymbol{f}$ is the forcing vector in respect to time (t), both at each Degree of Freedom (DOF). $\ddot{\mathbf{y}}(t)$ is the accelerations and $\dot{\mathbf{y}}(t)$ is the velocity at each DOF. Equation (3.1) represents a differential equation that is assumed to have a solution:

$$\boldsymbol{y}(t) = \boldsymbol{q}e^{\lambda t} \tag{3.2}$$

Including the amplitude, $\mathbf{q}$, at each DOF.

When substituting (3.2) into (3.1) and with the assumption of a unloaded system, the result is a characteristic equation:

$$(\lambda^2 \mathbf{M} + \lambda \mathbf{C} + \mathbf{K})\boldsymbol{q} = 0 \tag{3.3}$$

For tall timber buildings specifically, the reaction when loaded dynamically is a oscillating response. Typically this is a sign for a system that is underdamped [30]. With introducing complex conjugate pair the differential equation can be solved, for most situations [31]:

$$\lambda_j = -\omega_n \xi \pm i\omega_n \sqrt{1 - \xi^2} \tag{3.4}$$

Where ω_n is the natural frequency and ξ_n is the modal damping ratio, both of mode n.

The formulas for natural frequency, damped natural frequency, and modal damping ratio:

$$\omega_n = [\lambda] \tag{3.5}$$

$$\omega_d = Im(\lambda) \tag{3.6}$$

$$\xi_n = -\frac{Re(\lambda)}{[\lambda]} \tag{3.7}$$

With the assumption of the damping equal to zero the mode shapes can be estimated to be represented by:

$$\boldsymbol{y}(t) = \boldsymbol{q}e^{i\omega t} \tag{3.8}$$

Thus the homogeneous part in the differential equation after dividing by the harmonic part can be expressed by:

$$-\omega^2 \mathbf{M} + \mathbf{K} = 0 \tag{3.9}$$

ω_n is the natural frequency and $\boldsymbol{\omega}^2$ is a diagonal matrix with natural frequencies. The equation (3.9) is also known as the eigenvalue problem:

$$(\mathbf{K} - \omega_n^2 \mathbf{M})\phi_n = 0 \tag{3.10}$$

ϕ_n is the eigenvector in the mode shape with the natural frequency ω_n.

This eigenvalue problem is for damping neglected. When damping has not been neglected, estimating mode shapes becomes more complicated. The eigenvalue problem will then be a *second order eigenvalue problem* where not only λ is present, but λ^2 is included. A possible solution is to write equation (3.1) in something called a state-space problem.

3.2　State-Space Models

The state-space model convert the problem into two first order problems, *state equation* and *observation equation*.

3.2.1　State Equation

The first step is to transform the force vector into a vector which describes the location ($\bar{\mathbf{B}}$) of the inputs and the time variation ($\boldsymbol{u}(t)$). This can be done by factorising the force vector. Then the equation (3.1) can be expressed like this:

$$\mathbf{M}\ddot{\boldsymbol{y}}(t) + \mathbf{C}\dot{\boldsymbol{y}}(t) + \mathbf{K}\boldsymbol{y}(t) = \bar{\mathbf{B}}\boldsymbol{u}(t) \tag{3.11}$$

Or by pre-multiplying $\mathbf{M}^{-1}$:

$$\ddot{\boldsymbol{y}}(t) + \mathbf{M}^{-1}\mathbf{C}\dot{\boldsymbol{y}}(t) + \mathbf{M}^{-1}\mathbf{K}\boldsymbol{y}(t) = \mathbf{M}^{-1}\bar{\mathbf{B}}\boldsymbol{u}(t) \tag{3.12}$$

State vector is introduced and defined as:

$$\boldsymbol{s}(t) = \left\{ \begin{array}{c} \dot{\mathbf{y}}(t) \\ \mathbf{y}(t) \end{array} \right\} \tag{3.13}$$

By substituting equation (3.13) into equation (3.12) and using the *identity matrix* $\mathbf{I}$, it now yields:

$$\dot{\boldsymbol{s}}(t) = \underbrace{\left[\begin{array}{cc} -\mathbf{M}^{-1}\mathbf{C} & -\mathbf{M}^{-1}\mathbf{K} \\ \mathbf{I} & \mathbf{0} \end{array} \right]}_{\mathbf{A}_c \text{ is the state matrix}} \boldsymbol{s}(t) + \underbrace{\left[\begin{array}{c} \mathbf{M}^{-1}\bar{\mathbf{B}} \\ \mathbf{0} \end{array} \right]}_{\mathbf{B}_c \text{ is the input matrix}} \boldsymbol{u}(t) \tag{3.14}$$

The *state equation* can now be expressed as:

$$\dot{\boldsymbol{s}}(t) = \mathbf{A}_c\boldsymbol{s}(t) + \mathbf{B}_c\boldsymbol{u}(t) \tag{3.15}$$

The subscript c denotes continuous time.

3.2.2 Observation Equation

Where the *state equation* (3.15) describes the state of the system influenced by the input to the system, the *observation equation* describes the measured outputs. It can be written as:

$$\boldsymbol{y}_l(t) = \mathbf{C}_a \ddot{\boldsymbol{y}}(t) + \mathbf{C}_y \dot{\boldsymbol{y}}(t) + \mathbf{C}_d \boldsymbol{y}(t) \tag{3.16}$$

This is with the assumption that the measurements (accelerometers) are at a l locations. $\mathbf{C}_a$, $\mathbf{C}_v$, and $\mathbf{C}_d$ are output location matrices for acceleration, velocity, and displacement. By substituting the expression for $\ddot{\boldsymbol{y}}(t)$ in (3.12) into (3.16) leads to this equation:

$$\boldsymbol{y}_l(t) = [\mathbf{C}_v - \mathbf{C}_a \mathbf{M}^{-1} \mathbf{C}]\dot{\boldsymbol{y}}(t) + [\mathbf{C}_d - \mathbf{C}_a \mathbf{M}^{-1} \mathbf{K}]\boldsymbol{y}(t) + [\mathbf{C}_a \mathbf{M}^{-1} \bar{\mathbf{B}}]\boldsymbol{u}(t) \tag{3.17}$$

which again can be rewritten as:

$$\boldsymbol{y}(t) = \underbrace{\left[\ \mathbf{C}_v - \mathbf{C}_a \mathbf{M}^{-1} \mathbf{C} \quad \mathbf{C}_d - \mathbf{C}_a \mathbf{M}^{-1} \mathbf{K}\ \right]}_{\mathbf{C}_c} \boldsymbol{s}(t) + \underbrace{\left[\mathbf{C}_a \mathbf{M}^{-1} \bar{\mathbf{B}}(t)\right]}_{\mathbf{D}_c} \boldsymbol{u}(t) \tag{3.18}$$

The *observation equation* can then be written as:

$$\boldsymbol{y}(t) = \mathbf{C}_c \boldsymbol{s}(t) + \mathbf{D}_c \boldsymbol{u}(t) \tag{3.19}$$

with an *output influence matrix* $\mathbf{C}_c$ and *direct transmission matrix* $\mathbf{D}_c$. If no accelerometers are used for output measurements, then the *direct transmission matrix* disappears. This is due to the step change in $\boldsymbol{y}(\text{t})$ creating a step change in the response of the accelerometers. The *direct transmission matrix* is related to the changes and therefore disappears.

3.2.3 Eigenvalue Characteristics Across Realisations

In the *continuous-time state-space model* there exist a *realisation*. A realisation is a relationship between a given system and the infinite number of the equivalent state-space representations. For the system, it can only establish one of these representations, or realisations. By introducing a *similarity transformation matrix* the *realisations* can be multiplied.

$$\boldsymbol{s}(t) = \mathbf{T}\boldsymbol{z}(t) \tag{3.20}$$

where the $\mathbf{T}$ is an arbitrary non-singular square matrix.

When this is introduced in the *continuous-time state-space model*:

$$\dot{\boldsymbol{z}}(t) = \mathbf{T}^{-1}\mathbf{A}_c\mathbf{T}\boldsymbol{z}(t) + \mathbf{T}^{-1}\mathbf{B}_c\boldsymbol{u}(t) \tag{3.21}$$

$$\boldsymbol{y}(t) = \mathbf{C}_c\mathbf{T}\boldsymbol{z}(t) + \mathbf{D}_c\boldsymbol{u}(t) \tag{3.22}$$

The equation (3.21) can be compared to equation (3.15) and equation (3.22) can be compared to equation (3.19). The comparison shows the matrices $\mathbf{T}^{-1}\,\mathbf{A}_c\,\mathbf{T}$, $\mathbf{T}^{-1}\mathbf{B}_c$, $\mathbf{C}_c\,\mathbf{T}$, and $\mathbf{D}_c$ do describe the relationships at the matrices $\mathbf{A}_c$, $\mathbf{B}_c$, $\mathbf{C}_c$, and $\mathbf{D}_c$. Thus preserving the eigenvalues for the system across all realisations.

3.2.4 Discretisation and Added Noise

The experimental data will give measurements that are given at discrete time instants, but the equations (3.15) and (3.19) are expressed in continuous time. The solution for this is to convert the *continuous-time state-space model* in to discrete time, a *discretisation*. With a given sampling period, $\Delta t = 1/f_s$, and a time step, $t_k = k\Delta t$, the equations can be solved. For a time step an assumption has to be made about the behaviour of the time-dependent variables in between to samples. One assumption is the Zero Order Hold (ZOH) which makes the input a piecewise constant over the sampling period. When this assumption is made the *continuous-time state-space model* can be converted to the *discrete-time state-space model*:

$$\boldsymbol{s}_{k+1} = \mathbf{A}\boldsymbol{s}_k + \mathbf{B}\boldsymbol{u}_k \tag{3.23}$$

$$\boldsymbol{y}_k = \mathbf{C}\boldsymbol{S}_k + \mathbf{D}\boldsymbol{u}_k \tag{3.24}$$

where $\boldsymbol{s}_k = \boldsymbol{s}(k\Delta t)$ is the *discrete-time state vector*, thus giving the sampled displacements and velocities. $\boldsymbol{u}_k$ is the sampled input and $\boldsymbol{y}_k$ is the sampled output. $\mathbf{A}$

is the *discrete state matrix*, $\mathbf{B}$ is the *discrete input matrix*, $\mathbf{C}$ is the *discrete output matrix*, and $\mathbf{D}$ is the *direct transmission matrix*. There need to be a relationship between the continuous-time matrices and the corresponding discrete time matrices. These relationships is expressed in the following way:

$$\mathbf{A} = e^{\mathbf{A}_c \Delta t} \tag{3.25}$$

$$\mathbf{B} = (\mathbf{A} - \mathbf{I})\mathbf{A}_c^{-1}\mathbf{B}_c \tag{3.26}$$

$$\mathbf{C} = \mathbf{C}_c \tag{3.27}$$

$$\mathbf{D} = \mathbf{D}_c \tag{3.28}$$

The equations (3.23) and (3.24) represents a deterministic model, because the system is built upon only a deterministic input. The use of OMA in the case of this thesis is not built on a deterministic input, it is built on stochastic input, e.g. wind, human activity. A possible solution to solve this is to introduce *process noise* $\boldsymbol{w}_k$, and *measurement noise* $\boldsymbol{v}_k$. This translates the discrete-time stochastic state-space model to:

$$\boldsymbol{s}_{k+1} = \mathbf{A}\boldsymbol{s}_k + \boldsymbol{w}_k \tag{3.29}$$

$$\boldsymbol{y}_k = \mathbf{C}\boldsymbol{s}_k + \boldsymbol{v}_k \tag{3.30}$$

Then the system's dynamic behaviour is modelled by the state equation, and the observation equation determines the system's dynamic response, which can be seen in the model's output.

When the input $\boldsymbol{u}_k$ is unknown, the model is driven by the process noise $\boldsymbol{w}_k$, while the measurement noise $\boldsymbol{v}_k$ accounts for inaccuracies in the sensors. This is essential for OMA. Because by using Stochastic Subspace Identification (SSI) in OMA, the system uses its own generated $\boldsymbol{y}_k$ to generate realisation of the matrices $\mathbf{A}$ and $\mathbf{C}$.

3.3   Kalman Filter

The Kalman filter, or linear quadratic estimation, is an algorithm that can produce estimates of unknown variables based on a series of measurements. This is done in two repetitive steps, prediction and update. In the first step, the Kalman filter estimates the current state variables. In the second step, it updates the estimate once it observes the next measurement [32].

In this thesis, the Kalman filter is used to express the state-space model in equation (3.29) and (3.30), by use of the *forward innovation model*, with the unknown system matrices $\mathbf{A}$ and $\mathbf{C}$. Also included are noise covariance matrices $\mathbf{S}^{vw}$, $\mathbf{Q}^{vw}$, and $\mathbf{R}^{vw}$. With the assumption of the unknown matrices to be known, combined with a random process and measurement noise and the covariance between two different time steps is zero, an expression for auto- and cross-covariance of the noise is given:

$$
E\left[\left\{\begin{array}{c} \boldsymbol{w}_p \\ \boldsymbol{v}_p \end{array}\right\} \ \langle\ \boldsymbol{w}_q^T \ \ \boldsymbol{v}_q^T \ \rangle\ \right] = \begin{cases} \left[\begin{array}{cc} \mathbf{Q}^{ww} & \mathbf{S}^{wv} \\ \mathbf{S}^{wv^T} & \mathbf{R}^{vv} \end{array}\right] & p = q \\ \\ \mathbf{0} & p \neq q \end{cases} \tag{3.31}
$$

with the two arbitrary time instants, p and q. The identification process also estimates the matrices $\mathbf{Q}^{ww}$, $\mathbf{R}^{vv}$, and $\mathbf{S}^{wv}$.

To minimise the error that occurs between the predicted and measured response, an *optimal predictor* is introduced. To quantify the quality of the predicator a *state predication error* is defined:

$$
\boldsymbol{\varepsilon_k} = \boldsymbol{s_k} - \hat{\boldsymbol{s}}_{\boldsymbol{k}} \tag{3.32}
$$

The state prediction error represents the part, $\boldsymbol{s}_k$. This part cannot be predicted by the one-step ahead predictor of the state vector $\hat{\boldsymbol{s}}_k$. That is defined by the conditional mean of $\boldsymbol{s}_k$:

$$
\hat{\boldsymbol{s}}_k = E\left[\ \boldsymbol{s}_k | \mathbf{Y}^{k-1} |\ \right] \tag{3.33}
$$

$\mathbf{Y}^{k-1}$ is a matrix of the vectors from the known previous measurements:

$$
\mathbf{Y}^{k-1} = \left[\boldsymbol{y}_0, \boldsymbol{y}_1, ..., \boldsymbol{y}_{k-1}\right]^T \tag{3.34}
$$

Similarly to the state prediction error, the definition of *innovation* is:

$$
\boldsymbol{e}_k = \boldsymbol{y}_k - \hat{\boldsymbol{y}}_k \tag{3.35}
$$

The predicted differences in the measurements $\hat{\boldsymbol{y}}_k$ is:

$$\hat{\boldsymbol{y}}_k = E\left[\ \boldsymbol{y}_k | \mathbf{Y}^{k-1} | \ \right] \tag{3.36}$$

Equation (3.30) into (3.36) yields:

$$\hat{\boldsymbol{y}}_k = E\left[\ \boldsymbol{y}_k | \mathbf{Y}^{k-1} | \ \right] = E\left[(\mathbf{C}\boldsymbol{s}_k + \boldsymbol{v}_k) | \mathbf{Y}^{k-1} |\right] = \mathbf{C}\hat{\boldsymbol{s}}_k \tag{3.37}$$

When assuming no correlation in the measurement noise $\boldsymbol{v}_k$ at an instant $\boldsymbol{t}_k$ and the previous measurement $\left[|\mathbf{Y}^{k-1}|\right]$, an expression for the linear and time invariant Kalman filter system is:

$$\hat{\boldsymbol{s}}_{k+1} = \mathbf{A}\hat{\boldsymbol{s}}_k + \mathbf{K}_k \boldsymbol{e}_k \tag{3.38}$$

$$\boldsymbol{e}_k = \boldsymbol{y}_k - \mathbf{C}\hat{\boldsymbol{s}}_k \tag{3.39}$$

where $\mathbf{K}_k$ is the matrix for the *nonsteady state Kalman gain*, found with the algebraic Ribbati equation $\mathbf{P}$, with the initial state estimate $\hat{\boldsymbol{s}}_0 = \mathbf{0}$, the initial covariance of the state estimate $\mathbf{P}_0 = E\left[\hat{\boldsymbol{s}}_0 \hat{\boldsymbol{s}}_0^T\right] = \mathbf{0}$, and the output measurements $\left[\mathbf{Y}^{k-1}\right]$. Then the nonsteady-state Kalman gain estimate at time t_k can be obtained.

$$\hat{\boldsymbol{s}}_k = \mathbf{A}\hat{\boldsymbol{s}}_{k-1} + \mathbf{K}_{k-1}(\boldsymbol{y}_{k-1} - \mathbf{C}\hat{\boldsymbol{s}}_{k-1}) \tag{3.40}$$

$$\mathbf{K}_{k-1} = (\mathbf{G} - \mathbf{A}\mathbf{P}_{k-1}\mathbf{C}^T)(\mathbf{R}_0 - \mathbf{C}\mathbf{P}_{k-1}\mathbf{C}^{-1})^{-1} \tag{3.41}$$

$$\mathbf{P}_k = \mathbf{A}\mathbf{P}_{k-1}\mathbf{A}^T + (\mathbf{G} - \mathbf{A}\mathbf{P}_{k-1}\mathbf{C}^T)(\mathbf{R}_0 - \mathbf{C}\mathbf{P}_{k-1}\mathbf{C})^{-1}(\mathbf{G} - \mathbf{A}\mathbf{P}_{k-1}\mathbf{C}^T)^T \tag{3.42}$$

In short, a Kalman filter finds an optimal prediction of the state vector, $\boldsymbol{s}_k$, from the measured output till *k-1*. Then the Kalman filter estimates are obtained from the linear combinations of the raw data.

Further, the dynamic model properties can be identified when combining the Kalman filter with SSI methods.

3.4 Data-Driven Stochastic Subspace Identification

Data-Driven Stochastic Subspace Identification (DD-SSI) is a method that uses intricate geometrical manipulation of matrices to establish state-space matrices with the measured output data. These state-space matrices are where the modal parameters can be obtained. It uses the state sequence, $\hat{\boldsymbol{s}}_k$, from the Kalman filter, before the estimation of the state-space matrices $\mathbf{A}$ and $\mathbf{C}$. For the state sequence to be obtained, an orthogonal projection of the *block Hankel matrix* of output measurements is used. It uses the Singular Value Decomposition (SVD) on the projection matrices. Thus the observability matrix is obtained, and the Kalman filter state sequence is easy to calculate. Then there is an opportunity to derive the state-space matrices with different approaches.

3.4.1 The block Hankel matrix

The start of the DD-SSI is the making of the block Hankel matrix:

$$
\mathbf{H}_{0|2i-j} = \frac{1}{\sqrt{j}} \left[\begin{array}{cccc}
\mathbf{y}_0 & \mathbf{y}_1 & \cdots & \mathbf{y}_{j-1} \\
\mathbf{y}_1 & \ddots & \ddots & \mathbf{y}_j \\
\vdots & \ddots & \ddots & \vdots \\
\mathbf{y}_{i-1} & \mathbf{y}_i & \cdots & \mathbf{y}_{i+j-2} \\
\hline
\mathbf{y}_i & \mathbf{y}_{i+1} & \cdots & \mathbf{y}_{i+j-1} \\
\mathbf{y}_{i+1} & \ddots & \ddots & \mathbf{y}_{i+j} \\
\vdots & \ddots & \ddots & \vdots \\
\mathbf{y}_{2i-1} & \mathbf{y}_{2i} & \cdots & \mathbf{y}_{2i+j-2}
\end{array} \right] = \left[\frac{\mathbf{Y}_{0|i-1}}{\mathbf{Y}_{i|2i-1}} \right] = \left[\frac{\mathbf{Y}_p}{\mathbf{Y}_f} \right] \tag{3.43}
$$

The Hankel matrix is built from the measurements directly. The build up is $2i$ block rows, j columns, and l rows in each block row. The dimensions becomes $2li \times j$. The letter l is a reference to the number of output time series, this means the number measured acceleration data points in this thesis. j is a reference to the different time instants including the assumption to the statistical proof in this method:

$$
j \to \infty \tag{3.44}
$$

To make this practical the j applications, including all measured samples N, are express as:

$$
N - 1 = 2i + j - 2 \Rightarrow j = N - 2i + 1 \tag{3.45}
$$

And by choosing the number of block row i in a way that complies with this condition:

$$li > n \tag{3.46}$$

to estimate the system order n the number of peaks in the trace from the matrix containing the number of peaks in the matrix of Power Spectral Density (PSD) plots. Alternatively, the singular value plots from the SVD in the PSD matrix. With the Hankel matrix, it is possible to split it into two submatrices: $\mathbf{Y}_p$ represents the past output and $\mathbf{Y}_f$ represents the future. Another way of writing the Hankel matrix is then possible when moving the border between the past and future outputs. One block row from the future is removed and another is added to the past:

$$\mathbf{H}_{0|2i-j} = \left[\begin{array}{c} \frac{\mathbf{Y}_{0|i-1}}{\mathbf{Y}_{i|i}} \\ \hline \mathbf{Y}_{i|2i-1} \end{array} \right] = \left[\begin{array}{c} \mathbf{Y}_p^+ \\ \hline \mathbf{Y}_f^- \end{array} \right] \tag{3.47}$$

Where the $\mathbf{Y}_p^+$ is a matrix with the past output including one block row added, and $\mathbf{Y}_f^-$ is a similar matrix with the future output, but one block row is removed.

3.4.2 Projection Matrices

The orthogonal projection is a geometrical manipulation, and is of the row space of the future outputs on the row space of the past outputs, and is defined as:

$$\mathbf{P}_i = \frac{\mathbf{Y}_f}{\mathbf{Y}_p} = \mathbf{Y}_f \mathbf{Y}_p^T (\mathbf{Y}_p \mathbf{Y}_p^T)^+ \mathbf{Y}_p \tag{3.48}$$

To continue and calculate the necessary projections there needs to be a LQ decomposition of the known block Hankel matrix:

$$\mathbf{H}_{0|2i-j} = \mathbf{LQ} \tag{3.49}$$

And the matrix $\mathbf{L}$ is a lower triangular matrix expressed as:

$$\mathbf{L} = \left[\begin{array}{ccc} \mathbf{L}_{11} & \mathbf{0} & \mathbf{0} \\ \mathbf{L}_{21} & \mathbf{L}_{22} & \mathbf{0} \\ \mathbf{L}_{31} & \mathbf{L}_{32} & \mathbf{L}_{33} \end{array} \right] \tag{3.50}$$

And the $\mathbf{Q}$ is an orthonormal matrix:

$$\mathbf{Q} = \begin{bmatrix} \mathbf{Q}_1^T \\ \mathbf{Q}_2^T \\ \mathbf{Q}_3^T \end{bmatrix} \tag{3.51}$$

Now the expressions for the output sequence $\mathbf{Y}_{i|i}$ together with the projections $\mathbf{P}_i$ and $\mathbf{P}_{i-1}$:

$$\mathbf{P}_i = \frac{\mathbf{Y}_f}{\mathbf{Y}_p} = \begin{bmatrix} \mathbf{L}_{21} \\ \mathbf{L}_{31} \end{bmatrix} = \begin{bmatrix} \mathbf{Q}_1^T \end{bmatrix} \tag{3.52}$$

$$\mathbf{P}_{i-1} = \frac{\mathbf{Y}_f^+}{\mathbf{Y}_p^-} = \begin{bmatrix} \mathbf{L}_{31} & \mathbf{L}_{32} \end{bmatrix} = \begin{bmatrix} \mathbf{Q}_1^T \\ \mathbf{Q}_2^T \end{bmatrix} \tag{3.53}$$

$$\mathbf{Y}_{i|i} = \begin{bmatrix} \mathbf{L}_{21} & \mathbf{L}_{31} \end{bmatrix} = \begin{bmatrix} \mathbf{Q}_1^T \\ \mathbf{Q}_2^T \end{bmatrix} \tag{3.54}$$

3.4.3 Observability Matrix and the Kalman Filter State Sequence

If all modes are assumed excited by the process noise and can be identified, the system can be assumed controllable and observable, as long as the condition in (3.46) is satisfied. Then the main theorem in DD-SSI states that the projection matrix $\mathbf{P}_i$ can be factorised to the product of the observability matrix $\mathbf{O}_i$, and the Kalman filter state sequence $\hat{\mathbf{S}}_i$.

$$\mathbf{P}_i = \mathbf{O}_i \hat{\mathbf{S}}_i = \begin{bmatrix} \mathbf{C} \\ \mathbf{CA} \\ \vdots \\ \mathbf{CA}^{i-1} \end{bmatrix} \begin{bmatrix} \hat{\mathbf{s}}_i & \hat{\mathbf{s}}_{i+1} & \dots & \hat{\mathbf{s}}_{i+j-1} & \hat{\mathbf{s}}_i \end{bmatrix} \tag{3.55}$$

To derive the observability matrix and the Kalman filter state space sequence, a SVD is performed on the projection matrix:

$$\mathbf{P}_i = \begin{bmatrix} \mathbf{U}_1 & \mathbf{U}_2 \end{bmatrix} \begin{bmatrix} \mathbf{\Sigma}_1 & \mathbf{0} \\ \mathbf{0} & \mathbf{0} \end{bmatrix} \begin{bmatrix} \mathbf{V}_1^T \\ \mathbf{V}_2^T \end{bmatrix} = \mathbf{U}_1 \mathbf{\Sigma}_1 \mathbf{V}_1^T \tag{3.56}$$

Thus, the observability matrix and Kalman filter sequence can be calculated as:

$$\mathbf{O}_i = \mathbf{U}_i \mathbf{\Sigma}_1^{1/2} \mathbf{T}_1^T \tag{3.57}$$

$$\hat{\mathbf{S}}_i = \mathbf{O}_i^+ \mathbf{P}_i \tag{3.58}$$

$\mathbf{T}$ is a similarity transformation matrix and it can be set equal to the identity matrix. To get the one step ahead in the Kalman filter state sequence, these steps are needed:

$$\mathbf{P}_{i-1} = \mathbf{O}_1^{\uparrow} \hat{\mathbf{S}}_{i+1} \tag{3.59}$$

$$\hat{\mathbf{S}}_{i+1} = \mathbf{O}_1^{\uparrow +} \mathbf{P}_{i-1} \tag{3.60}$$

In total, there are now three different methods for computing the state-space matrices $\mathbf{A}$ and $\mathbf{C}$. The difference is that the first two do not ensure positive realness. That can lead to a synthesised spectrum matrix, that is not positive definite in all frequencies. The first sequence it uses the state sequence to estimate the state-space matrices. Where the Kalman filter state sequences $\hat{\mathbf{S}}_i$ and $\hat{\mathbf{S}}_{i+1}$, estimated in (3.58) and (3.60), to compute $\mathbf{A}$ and $\mathbf{C}$ from the overdetermined set of linear equations, by stacking the state-space models for the time instants i to $i + j - 1$:

$$\underbrace{\begin{bmatrix} \hat{\mathbf{S}}_{i+1} \\ \mathbf{Y}_{i|i} \end{bmatrix}}_{\text{known}} = \begin{bmatrix} \mathbf{A} \\ \mathbf{C} \end{bmatrix} \underbrace{\hat{\mathbf{S}}_i}_{\text{known}} + \underbrace{\begin{bmatrix} \rho_w \\ \rho_v \end{bmatrix}}_{\text{residuals}} \tag{3.61}$$

From the equation (3.61) the left side is known, with $\mathbf{Y}_{i|i}$ given by the block Hankel matrix of the known outputs. The whole Kalman filter state sequence $\hat{\mathbf{S}}_{i+1}$ and $\hat{\mathbf{S}}_i$ is computed by the known output measurements. The noise residuals, ρ_w and ρ_v, are unknown. The representation of the linear set of equations makes the noise residuals disappear in an LQ decomposition. The least-square noise residuals are uncorrelated with the states and therefore also orthogonal to the states $\hat{\mathbf{S}}_i$ and therefore do not affect the equations.

Thus the expression for the state-space matrices is represented as:

$$\begin{bmatrix} \mathbf{A} \\ \mathbf{C} \end{bmatrix} = \begin{bmatrix} \hat{\mathbf{S}}_{i+1} \\ \mathbf{Y}_{i|i} \end{bmatrix} \hat{\mathbf{S}}_i^+ \tag{3.62}$$

3.5 Stabilisation Diagram

A problem with a complicated and intricate method such as OMA is evaluating the quality of the results. A tool to visualise the output from the calculations is *stabilisation diagrams* which also can be seen as plots. The DD-SSI calculates the structural/dynamic properties for different model orders and then puts them through an evaluation criteria. The user sets the evaluation criteria to filter away mathematical poles and keep physical poles. It might be apparently physical poles originating from the system noise that needs to be filtered away.

In the figure (3.1) a stabilisation diagram with stable and unstable poles is displayed. It is essential to know that one dot is one pole.

The poles are calculated mathematically in every model order $n = [2, 4, ..., 150]$ over the expected frequency band. For many poles, the mathematical poles are just not physically possible and are therefore an *unstable pole*. At the same time, the poles where the mathematical poles are physically possible are deemed *stable poles*. The user sets the criteria for filtering out the spurious poles, which in this thesis are:

$$\frac{|\omega(n) - \omega(n - j)|}{\omega(n)} < 0.01 \tag{3.63}$$

$$\frac{\xi(n) - \xi(n - j)}{\xi(n)} < 0.05 \tag{3.64}$$

$$MPCW > 98 \tag{3.65}$$

These criteria mean the following: (3.63) demands a frequency of a pole that is less than 1% deviated from the pole in the preceding model order $n - j$. (3.64) demands the damping deviation from a pole to the preceding model order $n - j$ to be less than 5%. (3.65) demands the Weighted Modal Phase Collinearity (MPCW) to be close to 100 ensuring no complex modes. The full derivation of MPCW can be found in [33].

In these equations the $j = 1, ..., StabLevel$. *StabLevel* is the stability level, and tells the number of layers from previous model order equations (3.63 - 3.65) needs to be satisfied. For the experimental data in this thesis, the stability level is set at 3. Thus the criteria should be satisfied for all three preceding model orders $n - j$.

3.6 MAC

The Modal Assurance Criterion (MAC) value is a measurement used to compare the similarity in the mode shape vectors. It measures the experimental vector $\{\phi_n^e\}$ with the numerically obtained vector $\{\phi_n^a\}$. The formula is expressed as:

$$MAC(\{\phi_n^a\}, \{\phi_n^e\}) = \frac{|\{\phi_n^a\}^T\{\phi_n^e\}|^2}{(\{\phi_n^a\}^T\{\phi_n^a\})(\{\phi_n^e\}^T\{\phi_n^e\})} \tag{3.66}$$

From the MAC, the result varies between 0 and 1. If the value is 1, the mode shape vectors are identical. While they can vary in scale, the shape is the same. In contrast, if the value is 0, the vector is orthogonal to each other. This measurement is used by many to compare the consistency in mode shapes. It does not ensure validity, and it is more vulnerable if few measurement points are used. If the mode vectors are complex, which is not the case in this thesis, the transpose in (3.66) is changed with a Hermitian transpose (conjugate transpose).
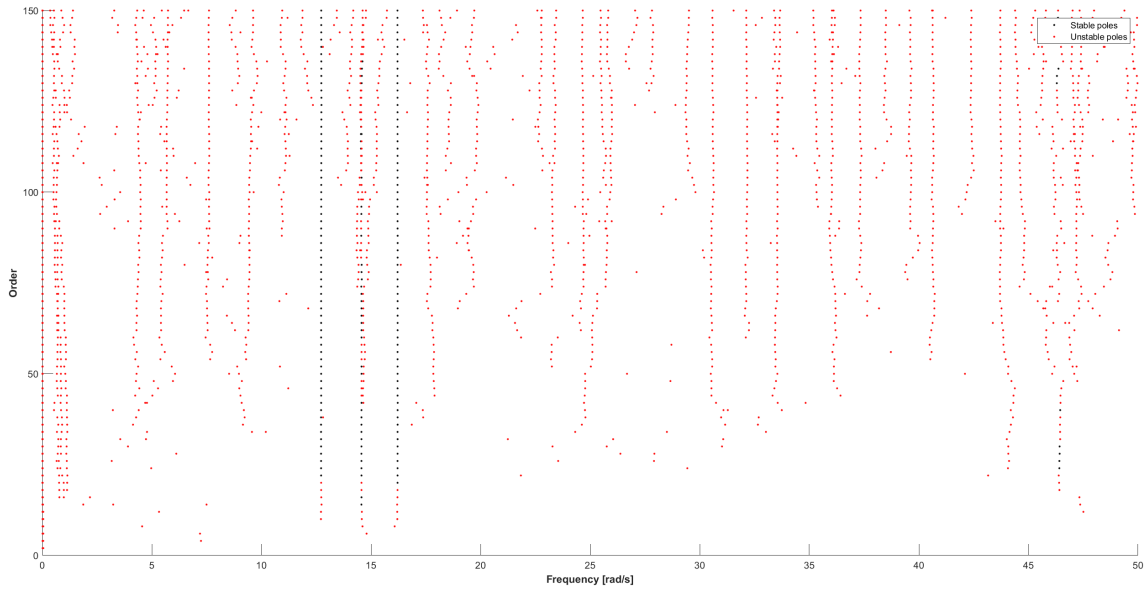
Figure 3.1: Stabilisation diagram with both stable and unstable poles. The red dots are the poles deemed unstable.
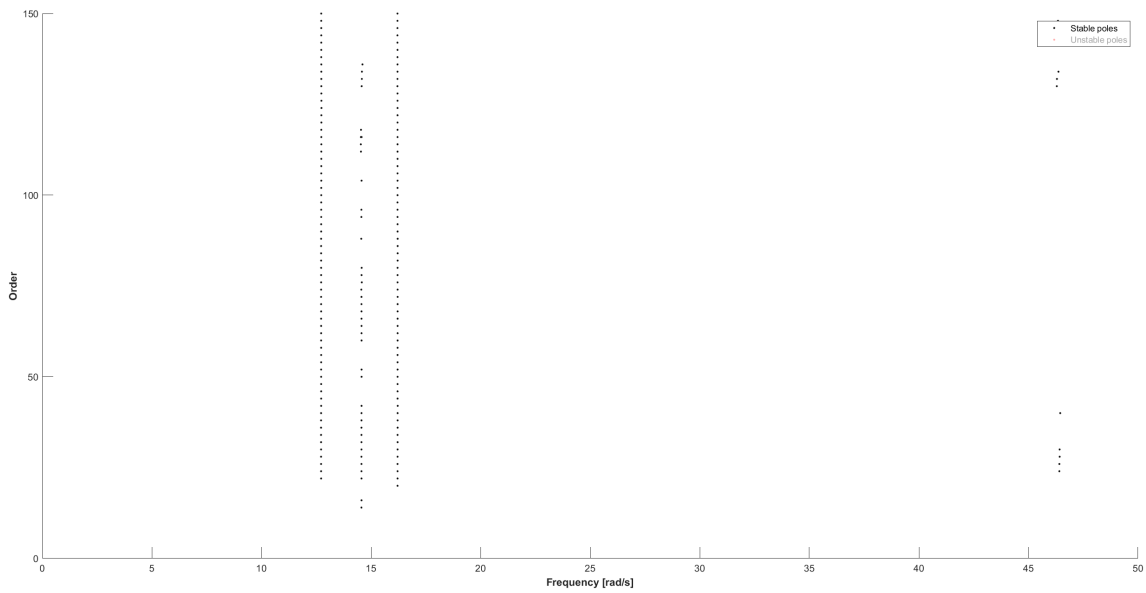

Figure 3.2: Stabilisation diagram with stable poles only
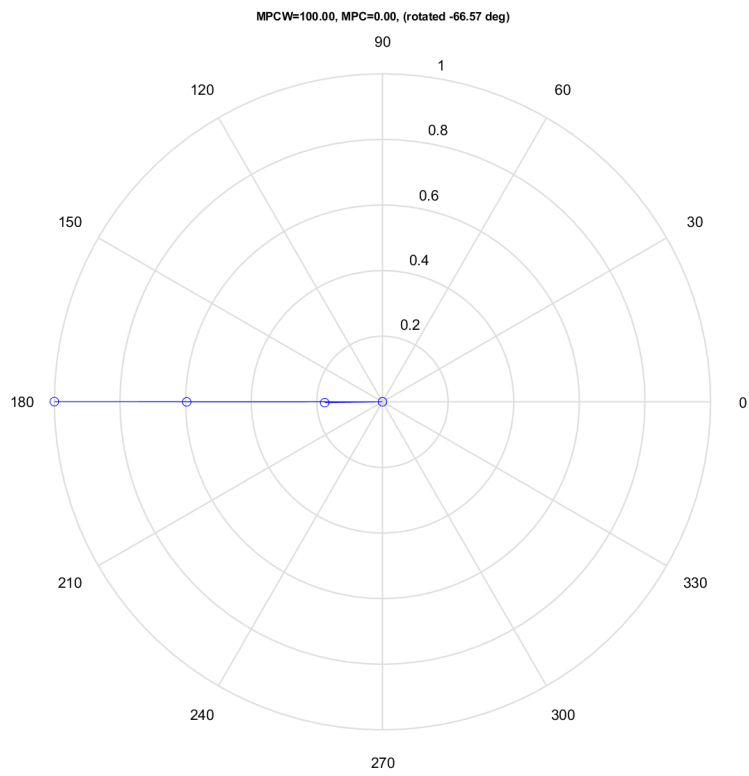
Figure 3.3: Complex plane plot of real mode
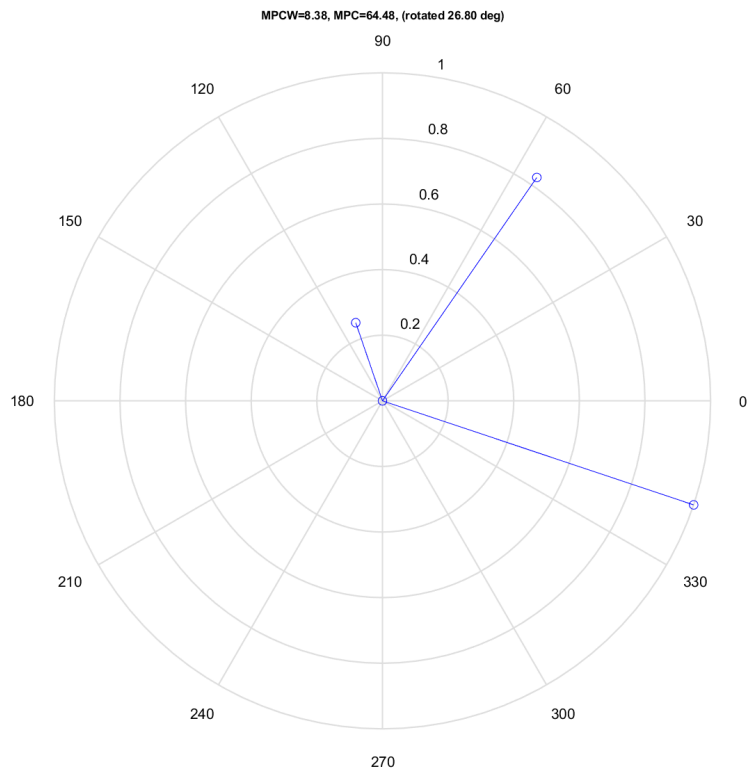
Figure 3.4: Complex plane plot of complex mode

3.7 Welch's Method

Welch's method, also known as *Welch procedure*, is used to estimate the PSD of a signal. The method divides the signal into multiple contiguous *segments* of length $T = N\Delta t$, which is subjected to direct Fast Fourier Transform (FFT) one by one. The PSD is then estimated by implementing an ensemble average over all the segments. This means the signal $x_i(t)$ is subjected to FFT, yielding $X_i(f)$ in the frequency domain. The segment number is i with the signal divided in n_d segments, which means that the segment number varies $i = 1...n_d$. The ensemble averaging over all segments, with N number of data points in each segment in the FFT calculation, is returned in the PSD as:

$$\hat{S}_{xx}(f) = \frac{2}{n_d N \Delta t} \sum_{i=1}^{n_d} |X_i(f)|^2 \tag{3.67}$$

3.7.1 Windowing

The measured signals in this thesis have a finite length, whereas the FFT assumes an infinite length signal. When subjected to a finite length signal, the FFT interprets the two endpoints as connected, thus creating an infinite loop of the finite signal. Suppose the signal is non-periodic, i.e. it does not consist of an integer number of periods to fill the time interval of the signal. In that case, it will lead to errors in the FFT caused by the discontinuities at the endpoints. The discontinuities will appear as high-frequency components in the FFT spectrum, components that are not present in the original signal. When this happens, it seems like the energy at a certain frequency in the FFT spectrum leaks into the other frequencies. This is known as spectral leakage. In order to reduce the effects of spectral leakage, windowing techniques are a helpful solution. Windowing eliminates the discontinuities at the endpoints of the signal by multiplying the signal with a window of finite length. The Hanning window, used in this thesis, has an amplitude which gradually approaches zero in a sinusoidal shape, illustrated by figure 3.5a). [34]

According to [34], the Hanning window is suitable for 95% of cases. Also, the Hanning window is the most suitable windowing technique for a narrowband random signal, or vibration data, according to [34]. This windowing technique has also been used in similar experiments in other theses at NTNU [4], [5].

To illustrate the FFT of a window, figure 3.5b) displays the spectrum of a Hanning window. The main lobe in the middle of the spectrum is centred at each frequency component of the signal. The side lobes gradually approach zero. The Hanning window yields a broad peak but has low side lobes, indicating low leakage [34]. However, the broad peak can cause errors in the PSD estimates. In order to correct this fault, the segments must be adequately long. Ideally, the length of each segment should be expanded until each segment's FFT matches the bandwidth with windowing that would occur without windowing. An undesired solution is reducing the number of

segments n_d, which reduces the quality of the PSD estimates. The preferred alternative is to overlap the segments, thus keeping the number of segments and increasing the segments' length simultaneously.

For the data in this thesis, the *cpsd()* function with a Hanning window *hann()* function for length *Nwindow* in MATLAB is used, with a 50% overlap. The equation (3.68) is utilised to calculate *Nwindow* length. In the equation the time series is downsampled by the factor $Q = 20$ and *length(signal)* is reflecting the number of data points.

$$Nwindow = \frac{length(signal)}{100} = \frac{431960}{100} \approx 4320 \tag{3.68}$$

(a) Hanning window   (b) FFT of Hanning window
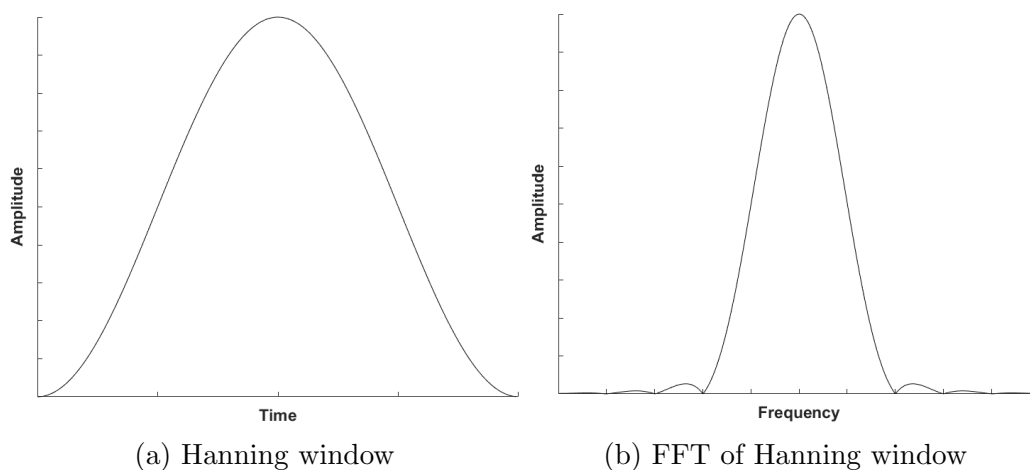
Figure 3.5: Illustration of the FFT spectrum of a Hanning window

Chapter 4

Measurements

Figure 4.1: Moholt 50|50

4.1 Description of the buildings

The buildings are nine storeys tall, where the top eight storeys accommodate students and the first storey accommodates functions mentioned in the introduction. There are three structural materials in the buildings: concrete, CLT, and Glulam. The first storey is concrete and has a more open interior layout. The top eight storeys are identical in interior layout, where there are 15 student dorms and a common area in each storey. There are three Glulam beams in the common area in the CLT storeys. The buildings have the same geometry, consisting of three wings

in a y-shape. The student dorms are divided into three groups, and each group is located in each wing of the y-shape. The common area is in the middle of the storey, towards where the facade has a kink. A student dorm is a building that naturally needs many walls because of the many rooms. For a CLT building, it is beneficial to have a lot of structural elements naturally in the building. The elements provide stiffness and weight to improve the dynamic properties.

(a) Concrete storey
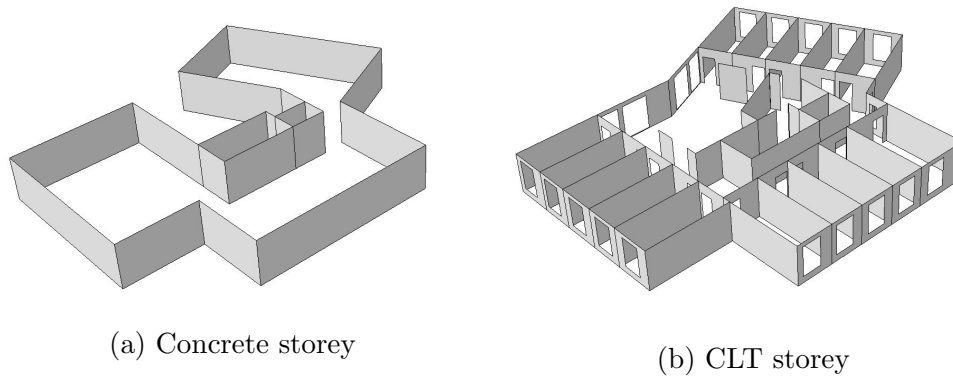
(b) CLT storey

Figure 4.2: Concrete and CLT storeys

4.2 Precautions in the measurements

After initial discussions with the building manager, SiT permitted the use of the five buildings in Moholt 50|50 for collecting experimental data. The accelerometers are connected to a central with cables when measuring the dynamic properties. Due to HSE rules, the fire cells could not be breached during the measurements, meaning there could not be cables running through doors. Thus, creating certain limitations for the locations of accelerometers. This challenge meant that the measurements were executed in two different ways: vertical and horizontal. Vertical measurements are when the accelerometers are spread over the building's height. In contrast, the horizontal measurements are when the accelerometers are spread over the building's width. A description of how these measurements were performed can be found in section 4.4 and 4.4.2. In addition to the HSE rules, the building manager explicitly wished to prevent permanent marks in the building.

When measuring buildings subjected to ambient vibration, an anemometer can be installed. When using an anemometer, the wind force to which the building is subjected is measured. Due to time limitations and the need for safety courses, this is not done for the measurements at Moholt 50|50.
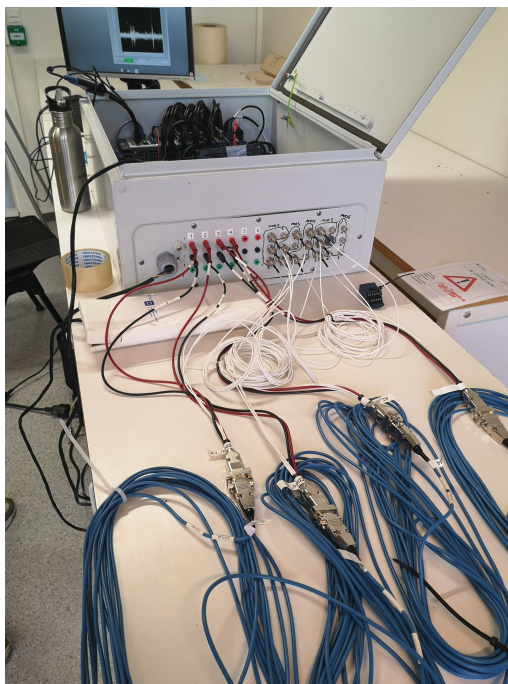
Figure 4.3: The equipment used for measuring the buildings

4.3 Description of the measurement equipment

The hardware setup was provided by the Department of Structural Engineering at NTNU. It consists of four Kistler accelerometers with accurate measurements down to 0 Hz, a GPS antenna to accurately time stamp the data and a 4G receptor for making the measurement central available off-site. The central's main component is the CompactRIO (cRIO) system from National Instruments. It consists of a cRIO controller, which houses a real-time processor and an Field-Programmable Gate Array (FPGA), and eight Input Output Module (I/O module). The FPGA is a semiconductor integrated circuit which allows the user to configure the circuit after manufacturing using the right software. The I/O modules can be fitted for individual needs. This setup consists of one NI-9467 module, five NI-9234 modules, one NI-9871 module, and one NI-9421 module. The NI-9467 module provides accurate time synchronisations, while the NI-9234 module acquisitions the measurements from the accelerometers. To store the data a two terabyte Solid State Drive (SSD) was connected to the cRIO controller.

Figure 4.4 displays how the central is set up before connecting all the necessary cables. On the left is where the central is connected with the accelerometers. In the next column, a backup battery is placed to ensure that measurements continue during eventual power outages. The next column consists of a 230V power outlet, a residual-current device, and switches to control which channels are active during measurements. The right column consists of the cRIO controller and modules. The following table summarises which hardware was used.

Table 4.1: List of hardware used in the measurements

Kistler Accelerometer	8396A2D0ATTA00, 8395A2D0DTTA00
Trimble GPS Antenna	P/N 66800-40D
NI cRIO	NI-cRIO-9036
NI modules	NI-9467, NI-9234, NI-9871, NI-9421
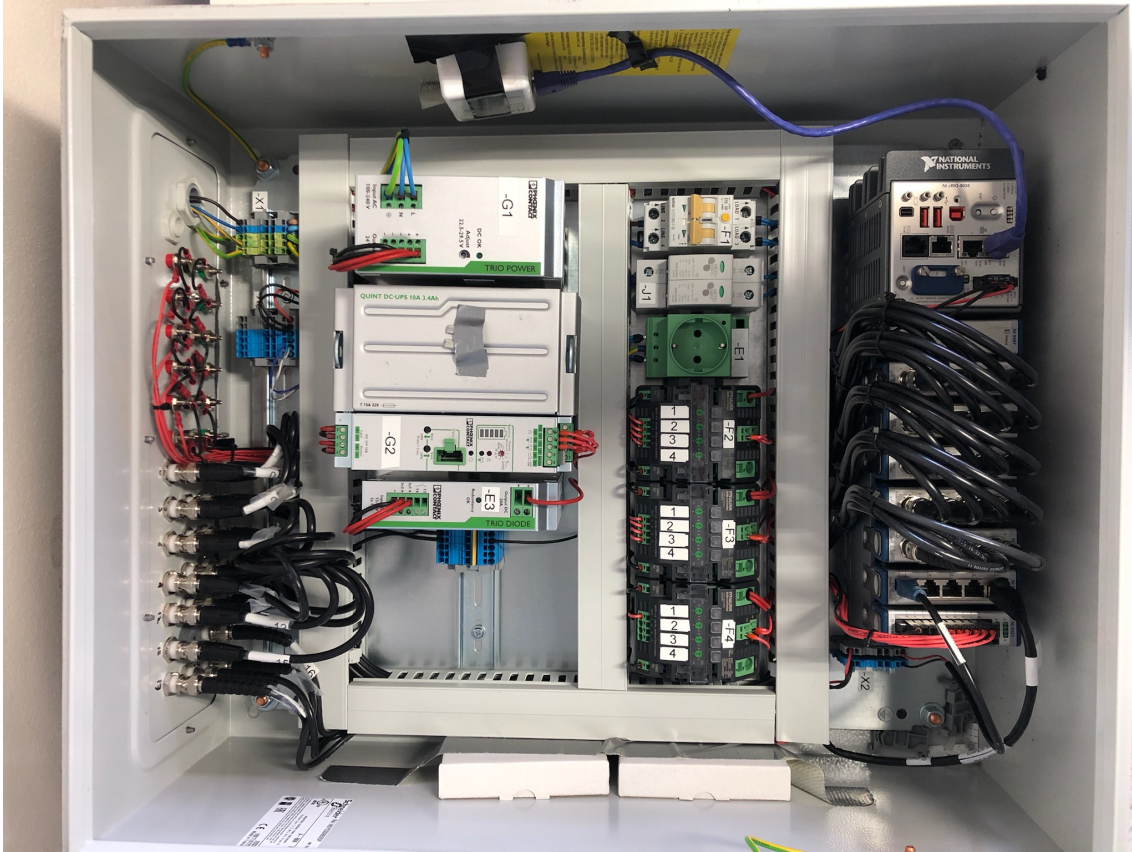
Figure 4.4: Inside the measurement central, unconnected

4.4 Layout for vertical measurement

In this case, the only suitable location available to measure the building in the vertical direction is the stairwell. That is the location that prevented most challenges, but some remained. Due to HSE rules, the central could not hinder the occupants' use of the stairwell, meaning it had to be placed outside the stairwell. The cables could go through small holes in the wall hidden above the ceiling finishes and into a separate storage room. All five buildings had an adequate storage room on the first storey. The stairwell has gaps of a few centimetres between the stair and the wall where the cables could go through storeys. Without these gaps, the cables available would not be sufficiently long.

The residents use the stairwell when the building is measured, and the installation should prevent creating unnecessary obstacles. Therefore, the cables were attached

to the walls with tape and plastic zip-ties where it was most suitable. Closer to the accelerometers, the cables were either fastened to the roofs, railings, or in existing cable bridges under the ceiling to prevent the cables from obstructing the residents.

It is crucial to prevent a load from the cables affecting the accelerometers. The accelerometers are too sensitive and need to be left unaffected. Together these solutions made sure the instalment neither affected the residents, damaged the building, nor influenced the measurements.

All vertical measurements lasted between 18 and 24 hours.

4.4.1 Accelerometers in the stairwell

The accelerometers should be placed with an interval spacing to obtain satisfactory results. The interval is necessary for the experimental data to show the vertical (cantilever) mode shapes and frequencies. Therefore the accelerometers were installed in the 3rd (A4), 6th (A3), and 9th storey (A1 and A2), illustrated by figure (4.5). In the 9th storey, two accelerometers were installed, with the maximum distance between them in an attempt to capture the torsional mode. Due to the space available limited by the HSE demands, the torsional modes measurements were limited. For vertical mode shapes, the locations of the accelerometers were deemed sufficient with the space available.
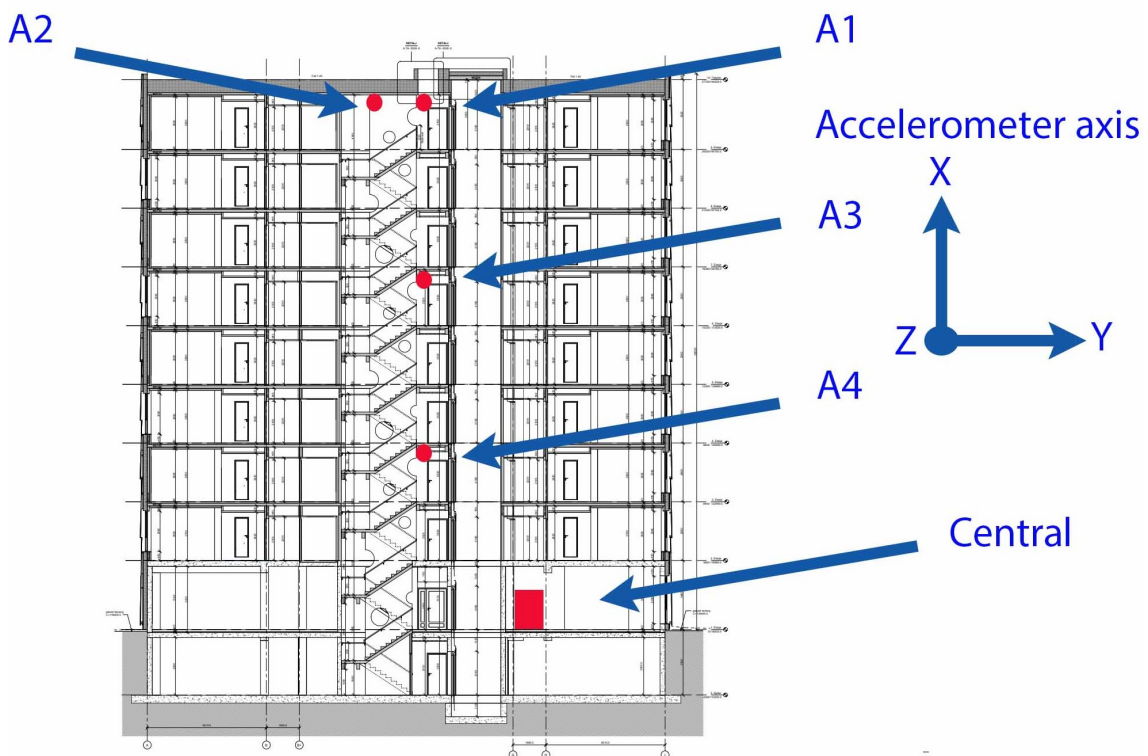
Figure 4.5: Accelerometers in the stairwell

The connections between accelerometers and walls were a steel plate screwed into the walls. These were screwed onto the CLT in existing cracks. The building manager wanted to minimise the permanent traces and proposed using this solution. These cracks provided a sufficient bonding between the plate and the wall. The CLT walls are a part of the structural system and are a good connection point to obtain physical movement from the building in the measurements. The accelerometers were mounted as high as possible on the walls because the vibration amplitude is most significant at the top. The residents use the stairwell and elevator, which can cause noise in the measured data. The use of the elevator can also result in some noise in the measurements. The building manager mentioned that, when the building was new, the residents had noted that the building vibrated when the elevator moved. However, the residents did not feel this anymore. The last noise for the accelerometers is the doors in the stairwell. They are connected to automatic mechanisms and should provide a minimal noise level in the measurements.

Figure 4.6: Accelerometer installed on a CLT wall

4.4.2 Measuring mode shapes in the common area

Since the locations of the accelerometers in the stairwell provided limited horizontal mode shapes in the experimental data, the building manager gave access to the resident's common area. However, the access was limited to one workday because the building manager wished to prevent disturbing the residents. This opportunity meant that the accelerometers could be placed with a larger interval between them in the horizontal plane than in the stairwell. The measurement is only performed in one building, due to time limitations and limited access. Because of the limited time, each in-plane measurement only lasted for three hours.

Measurements were performed in two different ways to provide more experimental data. In the first arrangement, all four accelerometers were on the 9th storey. In the second arrangement, one of the accelerometers (A1) stayed in its location, and three accelerometers were moved down two storeys. The layout is displayed in figure 4.8.

4.4.3 Accelerometers in the common area

The procedure is similar to the measurements in the stairwell (4.4.1). The same precautions were executed in the common area, including using cracks in the CLT, avoiding loads from the cables on the accelerometers, and limiting the obstacles for the residents. The accelerometers were mounted high on the walls, and the entire width of the common area was exploited. The cables went outside the building through the windows when the three accelerometers were moved down two storeys. This step was implemented with the permission of the building manager and carried out with caution.
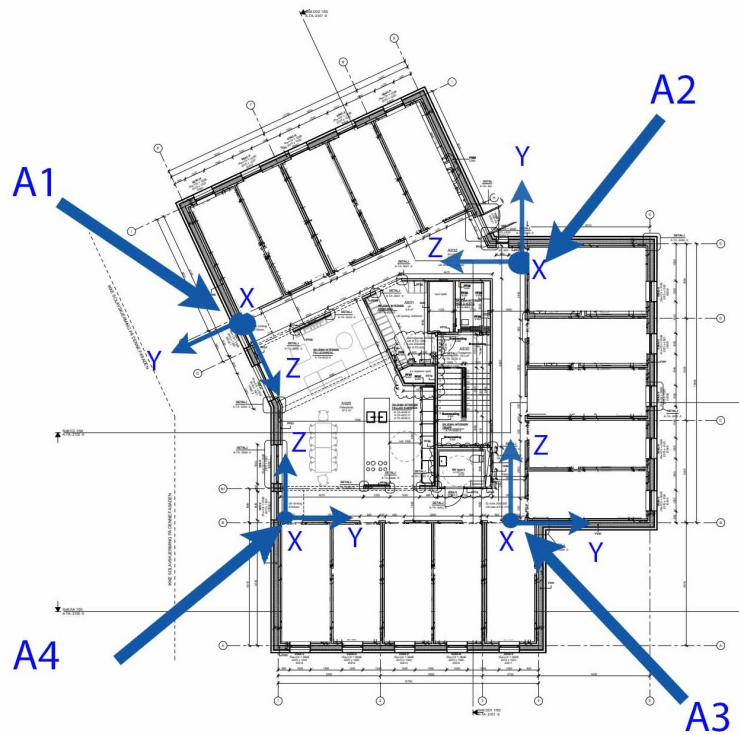
Figure 4.7: Accelerations layout 9th storey
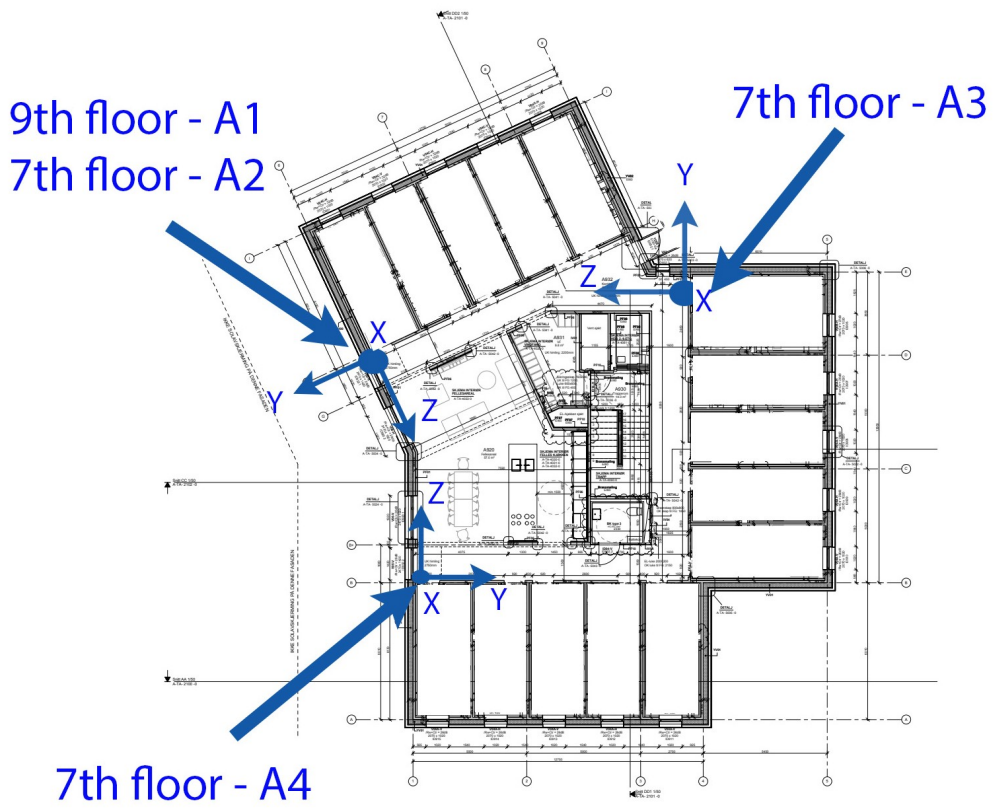
Figure 4.8: Accelerations layout 7th and 9th storey

Chapter 5

Data Acquisition and Processing

This chapter presents the software used to record the data. It also shows and explains how the data was processed before it was used to obtain the results presented in chapter 7.

Each building was measured between 18 and 24 hours. The system creates a new file to store the data every sixth hour, meaning that for each building the data set consists of at least three full six hour recordings. The files were generated on this form:

$$\underbrace{2022}_{\text{year}} - \underbrace{02}_{\text{month}} - \underbrace{28}_{\text{date}} - \underbrace{18 - 00 - 00}_{\text{UTC+0 time}} \underbrace{Z.tdms}_{\text{file extension}}$$

The first three numbers states which date the recording was done. The following three numbers states which time the recording of the file started at UTC+0 time. The last brace shows the file extension. An important notice here is the "Z" in the file extension, which is just an extension of a file's name and all files contains this. It has nothing to do with which direction is measured.

5.1 Software

The cRIO system was already set up through previous measurements performed at the Department, meaning no adjustments to the software were needed. This means the metadata was still set according to the last project where the equipment was used. This did not affect the results in any way.

5.1.1 Sampling rate of NI-9234

$$f_s = \frac{f_m}{256 \cdot n}, \; n = [1, 31] \tag{5.1}$$

Equation (5.1) shows the available data rates of the NI-9234 module [35]. The lowest data rate possible is 1652 Hz, which is an unnecessary high sampling rate for this type of measurement, explained in section 5.2. The FPGA has been modified to lower the sampling rate further so that the new sampling rate can be described as follows:

$$f_s = \frac{f_m \cdot L}{256 \cdot n \cdot M} \tag{5.2}$$

- f_s: sampling frequency

- f_m=13.1072 MHz, clock rate of the master module

- L: specifies the interpolation factor

- M: specifies the decimation factor of the rational resampler in the FPGA

- n: decimation factor for tuning to desired sampling frequency

5.2 Data processing

Over the past years, similar experimental measurements have been conducted by the Department of Structural Engineering at NTNU, both on master's thesis level and PhD level. As a result, multiple data processing tools have been developed, mainly MATLAB scripts. These have been a great benefit when processing the data from Moholt 50|50, where they were used as guidance on how to process the data using MATLAB. Most of the work done with the scripts was learning how they worked and reconfiguring them for Moholt 50|50. This section seeks to explain the processing of the data and the tools used to do so. The theory parts of this section are taken from Fabbrocino and Rainieri [28] if nothing else is stated.

5.2.1 Aliasing

When conducting a measurement of this sort, one of the most crucial settings is the sampling frequency. It is critical to set a high enough sampling frequency to get an accurate representation of the signal from the accelerometers. On the other hand, the advantage of a low enough sampling frequency which keeps the amount of data down, thus reducing the computational time and storage space. The most deciding factor to consider when determining the sampling frequency is what frequency range

is to be explored. This must be considered to avoid aliasing in the Analog-to-Digital Converter (ADC), where the analogue signal from the accelerometers is discretised into a digital signal. Aliasing in this stage of data sampling occurs when the sampling frequency is set too low relative to the analogue signal obtained from measuring.

According to *Shannon's theorem*, aliasing is avoidable by setting a sampling frequency at least twice as high as the highest frequency contained in the signal. For instance, if a signal has an expected maximum frequency of $\boldsymbol{A}$ Hz, the sampling frequency, f_s, must be set to $f_s > 2\boldsymbol{A}$. The threshold $f_s/2$ is known as the Nyquist frequency, denoted as f_N. This represents the upper limit of which the observable frequency range should lie. All frequency components in the signal above the limit are subjected to aliasing, which causes them to appear in the frequency range below the Nyquist frequency in the PSD. This phenomenon is also known as folding, and causes errors in the amplitude and frequency in the frequency range of the signal. The alias frequency, f_a, can be calculated and is given as:

$$f_a = |n \cdot f_s - f_{signal}| \tag{5.3}$$

where n is the integer which makes $(n \cdot f_s)$ the value closest to the signal frequency. Once the signal is converted in the ADC, the alias frequencies cannot be distinguished from the real measured frequencies below the Nyquist frequency. To avoid aliasing in the ADC, all frequency components above the Nyquist frequency must be removed before converting the signal from analogue to digital. A low-pass filter can do this in the ADC, also known as an anti-aliasing filter. The ideal anti-aliasing filter has a sharp cut-off. It passes all frequency components below the cut-off frequency and removes all frequency components above the cut-off frequency. This cannot be achieved since no low-pass filter has an infinitely sharp roll-off. A real anti-aliasing filter has a transition band which gradually attenuates the frequencies above the cut-off frequency. Therefore, the cut-off frequency must be set lower than the Nyquist frequency, where the quality of the filter decides how much lower it needs to be. According to the datasheet of the NI-9234 module [35] used in this setup, the cut-off frequency and the stopband frequency are set at $0.45f_s$ and $0.55f_s$, respectively. This means that the transition band lies between $[0.45f_s, 0.55f_s]$, as illustrated in figure 5.2. With a sampling frequency set at $f_s = 400Hz$, all frequencies below $0.45f_s = 180Hz$ should be free of alias frequencies, and any distortion of the frequencies close to the transition band is of no concern since the expected frequency range of the building is 1-10 Hz.
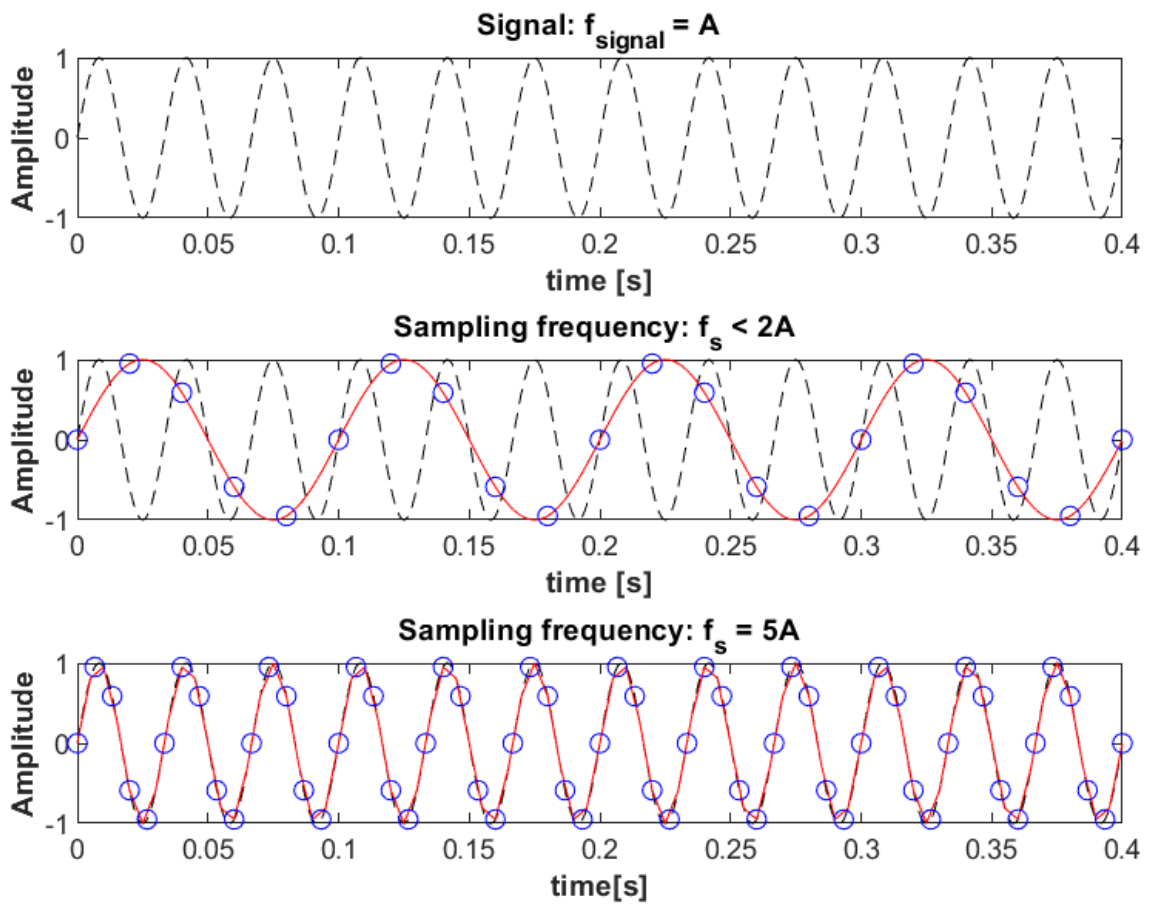
Figure 5.1: Illustration of aliasing
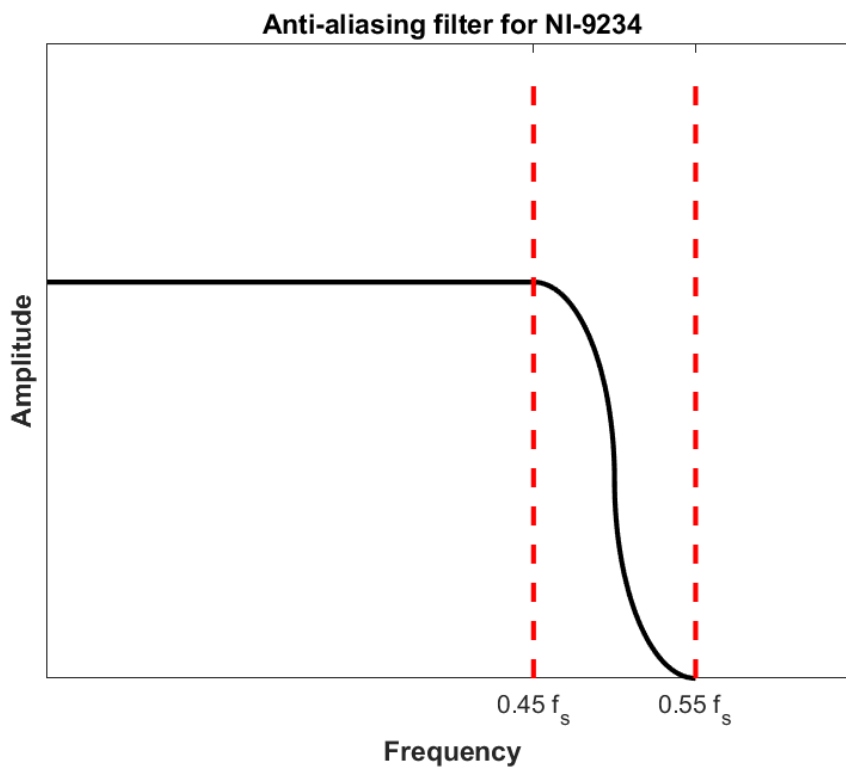
Figure 5.2: Illustration of the anti-aliasing filter in the I/O module NI-9234

5.2.2 Data processing using python

The data sets obtained from the measurements consisted of one Technical Data Management Streaming (tdms) file every six hours of recording. The .tdms-file format is developed by National Instruments and is designed to write and read measured data at high speed while maintaining a simple layout of the measured data. In this case, one such file typically had the size of about 1.6 gigabytes. Since MATLAB was the chosen software to process the data, it had to be converted to a suitable file format. To convert the .tdms-files into .mat-files, three python scripts provided by the department were used. These scripts sorted out only the necessary data to keep in the .mat-files, which reduced the file size to about 0.6 gigabytes, thus making the next steps of processing more effective. The most frequently used data in the results kept from the .tdms-files were the acceleration data in the Z-direction and Y-direction. The acceleration data from the X-direction were left out since the accelerations in this direction are assumed small and the results needed only involved the YZ-plane.

5.2.3 Data processing using MATLAB

Decimation

With the expected frequency range of the building lying between 1-10 Hz and a sampling frequency of 400 Hz, the rate of the amount of data captured against the amount needed to accurately represent the building was high. Decimation, or downsampling, was deployed to reduce the amount of data. This was done by the use of MATLAB's resample function. The decimation factor was set to Q=20, which meant that every 20th data point was kept while the rest was disregarded, thus making the new sampling frequency:

$$f_{s,dec} = \frac{1}{Q} \cdot f_s = \frac{1}{20} \cdot 400Hz = 20Hz \tag{5.4}$$

However, if this were the only measure performed to resample the data, there would be a new risk of aliasing. This can occur because there is also a new Nyquist frequency when the original input is resampled to a new sampling frequency. Since all frequencies above the Nyquist frequency are prone to aliasing, they must be removed before decimation. In this case, it is taken care of through the resample function from MATLAB, which applies a digital Finite Impulse Response (FIR) anti-aliasing low-pass filter [36]. This works in the same manner as described for the analogue anti-aliasing filter, where it removes all frequency components above the Nyquist frequency. Like the analogue version, the FIR filter has a transition band that gradually attenuates the frequencies. Usually, this band begin at 80% of the Nyquist frequency, thus making the new cut-off limit for the decimated frequency 8 Hz. For the sake of clarification, a quick sum up follows.

Original sampling frequency:	$f_s = 400Hz$
Original Nyquist frequency:	$f_N = f_s/2 = 200Hz$
Cut-off limit due to analog filter:	$f_c = 0.9f_N = 180Hz$
Decimation factor:	$Q = 20$
Decimated sampling frequency:	$f_{s,dec} = 20Hz$
Decimated Nyquist frequency:	$f_{N,dec} = 10Hz$
Aliasing can occur between:	$[f_{N,dec}, f_N]$
New cut-off limit due to FIR filter:	$f_{c,dec} = 0.8f_{N,dec} = 8Hz$

From the founds made by Olsen and Hansen [4], no relevant frequencies above 8 Hz were expected, with their highest measured frequency being about 6.6 Hz.

Detrending

Data sets like these measurements are sometimes subjected to offsets and spurious trends. One example of this is the X-direction accelerometer data, which lies in the same direction as gravity. This leads the accelerometer to oscillate around -2V in the X-direction. Spurious trends can often be explained by a change in temperature, which causes the signal to drift slightly. In this case, with measurements executed inside, the temperature was stable and no trends were detected. However, an offset was detected as can be seen in figure 5.3 a). To resolve this problem, the function detrend in MATLAB was deployed. The function detrends the data by removing the mean value of the input data. This leads to the data oscillating around 0, which is the wanted result. Figure 5.3 a) and b) illustrates how the data for accelerometer A1 in Y-direction initially was offset and then moved to 0.

Exclusion of data points

Some large peaks were visible at the start and end of the acceleration time series after decimation and detrending were performed on the data. These were caused by the FIR filter applied in MATLAB's resample function, which assumes that the input signal is zero before and after the filtered signal. Since the data had an offset, as shown in figure 5.3 a), these peaks had to be removed. This was done by excluding the first and last 750 data points, with a visual inspection of the acceleration time series confirming this was sufficient (figure 5.3 c). 1500 data points after decimation equates to 75 seconds worth of data, which in a six hour recording is a negligible amount.
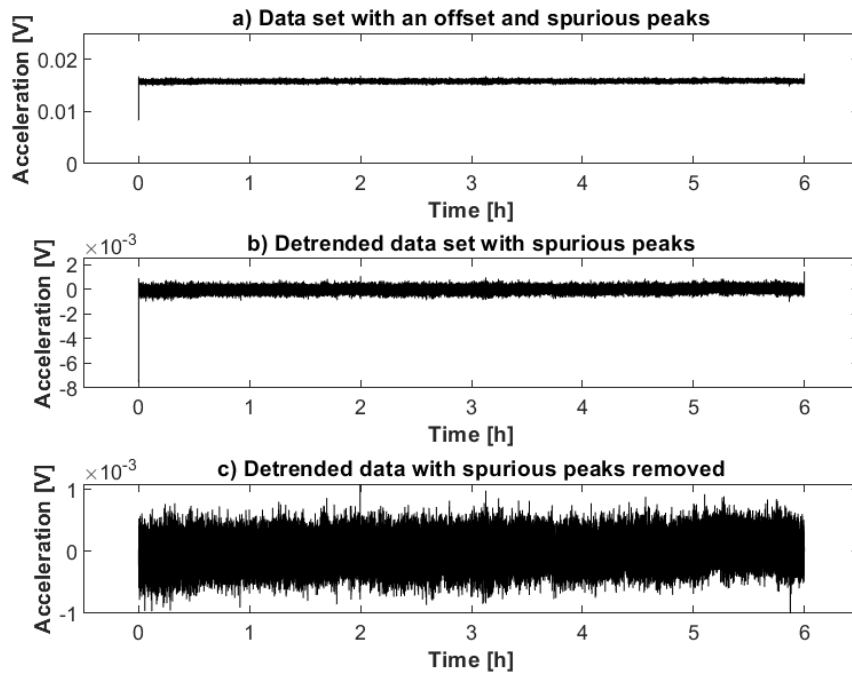
Figure 5.3: Illustration of how the data of accelerometer A1 was affected by detrending and removing of spurious peaks
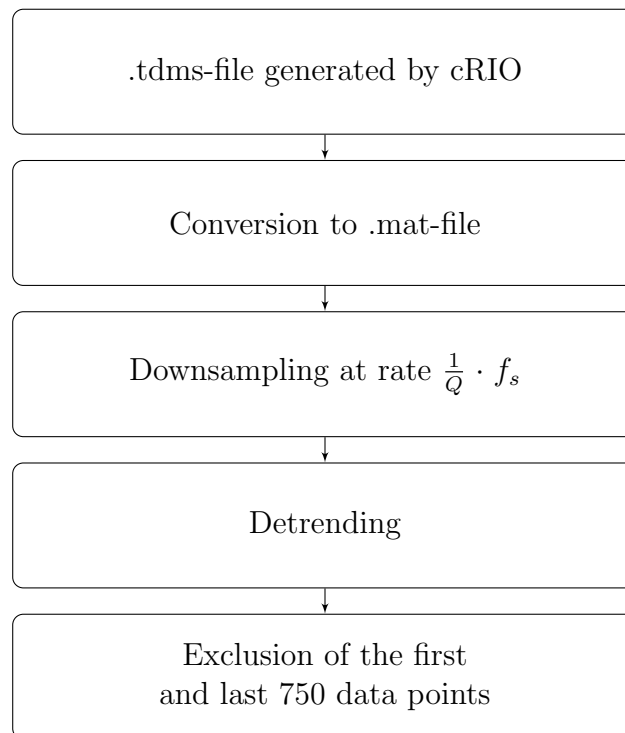
Figure 5.4: Flowchart of steps taken to process the data

Chapter 6

Numerical Model
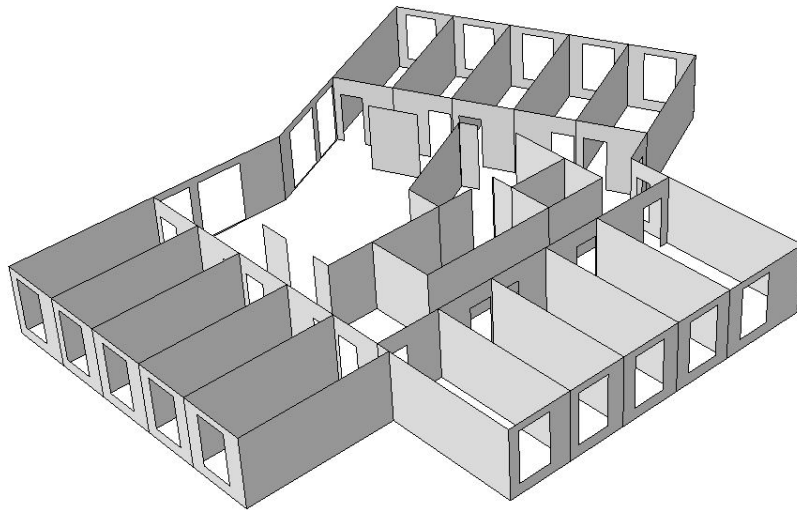
Figure 6.1: Illustration of CLT storey.

A numerical model can have several benefits when working with experimental data. Structures are different, but often have similarities in both geometry and materials. The differences give the structures their own way of moving in different mode shapes, and frequencies. When creating a numerical model that replicates the building virtually, it is possible to read estimations of the mode shapes and frequencies. Mode shapes have zero displacement locations where the building does not move. For instance it could be a rotation centre. To avoid installing the accelerometers in these sub-optimal locations, the numerical model can show the user a mode shape and therefore indicate the spots that can cause problems in the experimental data.

In a normal design process a building will be designed virtually before it is constructed. When working with experimental data, the building exist, and can be used to ensure a correct detailing. When doing a process like this, where the data can assure the preciseness, the knowledge can be used in future designs. A benefit of the nu-

merical model is that the mode shape can be compared with the mode shape vectors in the experimental data. To check if the model is well designed, the frequencies can be compared with the values in the experimental data. The model could be too stiff if the numerical frequencies are too large. In contrast, if the frequencies are too low, some stiffness can be missing in the model. The mass will also influence the natural frequencies, more mass will results in an lower frequency and vice versa. The discrepancy, between the numerical model and the experimental data, could be wrongdoing in the modelling or, e.g. imprecise material properties.

The Moholt 50|50 buildings have very similar structural systems. The difference is only on the first floor, with slight differences in the interior layout. Thus, it seemed most logical to make one model instead of five almost identical ones. The mode shapes do not change much with minor changes in the model, but the structural mass affects the frequencies. The nonstructural mass is complex to replicate because it is dependent on many variables. The mass is compared to the actual load in the building and not the Eurocode. The nonstructural mass should duplicate the buildings' actual nonstructural mass. It is also a problem, when calculating the nonstructural mass, that the mass in the building changes continuously with the residents' activity. During a holiday, the 15 residents in each storey leave and bring a load of their personal belongings. The complete opposite can be on a Saturday night when there can be a get-together and an increase in nonstructural mass and activity. With the amount of nonstructural mass in this building, the occupants mass should only slightly impact the dynamic properties.

The numerical model is made with Abaqus/CAE by Simulia. Abaqus is a Finite Element Analysis (FEA) program with a high level of detail and a detailed analysis. The basis of the modelling is the Abaqus-manual [37] and earlier experience. Abaqus is used extensively for research purposes. It is a program seldom used in engineering offices due to a slower work rate because of the required detail. It is missing opportunities to use predefined sections and Eurocode calculation checks, both of which can found in other FE programs, e.g. FEM-Design and ROBOT.

Abaqus provides practical opportunities, e.g. the extraction of displacements at nodes in elements. From Abaqus, the displacements are extracted to compare the mode shape vectors from the numerical model with the experimental data by using MAC. For an optimal comparison, the chosen nodes should be as close as possible to the actual locations of the accelerometers.

Compared to a real-life building, the model is simplified. There are several reasons for this, e.g. time and knowledge. One significant challenge is that CLT is a complex material to use in modelling and creates other challenges than a typical structural system of concrete or steel. The connections in CLT buildings is an important part of modelling with CLT. Steel connections are used in buildings at Moholt 50|50. The connections in CLT buildings are complicated to model, and it is a challenge to transform the real connections into theoretical ones in a finite element model. The connections are simplified to be able to create a working model. However, the model is assumed to be accurate and detailed enough to provide sufficient comparisons with the experimental data. In section (6.4) this is explained and researched further.

6.1   Materials
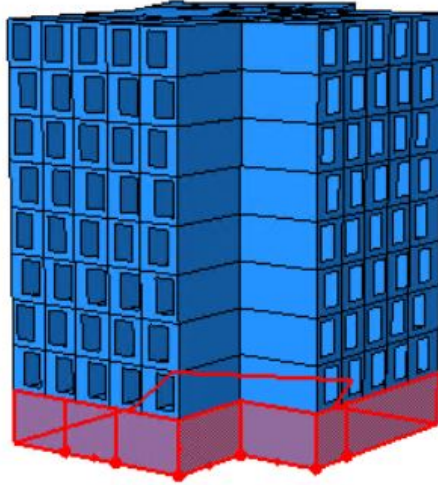
Figure 6.2: Model of a building at Moholt Student Village. The first storey (in red) is in concrete, the eight storeys above is in CLT

The model uses a structural system of two different materials. The first storey is concrete. The rest of the storeys are CLT elements, and a CLT floor separates the storeys consisting of a 70mm screed layer above a 140mm thick CLT panel. There are Glulam beams in the buildings, but these are not included in the model. The earlier work at Moholt 50|50 showed that the Glulam beams did not provide a significant sitffness, but created local bending spurious modes [4]. The CLT walls varies in thickness: 80mm, 100mm, 120mm, 140mm, and 160mm thick. To model the CLT it is used engineering constants in Abaqus. CLT is made by different manufacturers and has specific layer layouts and material properties. The most commonly used material quality for CLT, also used in this building, is C24. Stora Enso manufactures the CLT used in Moholt 50|50, and the technical brochure explains its properties [38]. The technical brochure from Stora Enso states that the material density is to be taken from EN 338 [39]. The concrete in Moholt 50|50 is of quality B30. Concrete is considered an isotropic material, and easier to model. These are the material properties used for the concrete:

Table 6.1: Concrete properties in Abaqus

	ρ [kg/m^3]	E [MPa]	ν
$B30$	2500	33000	0.2

Composite shells are created in Abaqus and assigned to CLT elements. These composite shells are made layer by layer for the specific sections. The sections that Stora Enso delivers are in their technical brochure [38]. The elements that are used

at Moholt 50|50 is: CLT 80 L3s, CLT 100 L5s, CLT 120 L5s, CLT 140 L5s, and CLT 160 L5s. The grain direction in the layers and element direction is specified in Abaqus. The values used in the engineering constants for the elastic material properties are from [40]. This is an approach used in [41], where it most accurately represents the reference model.

An alternative approach to model the stiffness in CLT that has been used in [4] is to use engineering constants for the combined strength in the section without taking the element layer layout into account.

The CLT properties used in every CLT element, for the final model, are:

Table 6.2: CLT properties in Abaqus. Elastic moduli are given in MPa

	$\rho[\mathrm{kg/m}^3]$	$E1$	$E2$	$E3$	$\nu12$	$\nu13$	$\nu23$	$G12$	$G13$	$G23$
CLT	420	10000	800	400	0.5	0.6	0.6	600	600	30

The different layout in the CLT elemtens:

Table 6.3: CLT elements layout

Thickness	Panel type	Layers	L	C	L	C	L
80	L3s	3	20	40	20		
100	L5s	5	20	20	20	20	20
120	L5s	5	30	20	20	20	30
140	L5s	5	40	20	20	20	40
160	L5s	5	40	20	40	20	40
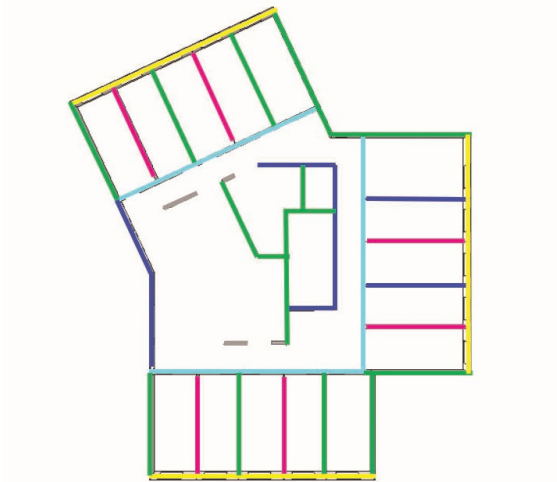
Figure 6.3: Illustration of CLT location

Table 6.4: CLT overview

	CLT storeys			
	2 - 3	4 - 5	6 - 7	8 - 9
Grey	160	140	120	120
Blue	140	120	100	100
Green	120	120	100	100
Cyan	120	120	100	100
Yellow	100	100	100	100
Pink	80	80	80	80

6.2 Elements

The CLT and concrete elements were assigned S4R shell elements in the mesh. The S4R is an appropriate element type for shell elements [42]. It is a general purpose, 3-dimensional, shear flexible, six DOFs at each node, and a 4-node element [43]. The R symbolises reduced integration and adopts the theory of reduced integration to treat the shear locking [42]. The S4-element created by Abaqus uses *thick-plate theory* (Reissner-Mindlin). The first floor columns have been made by using B32 elements in Abaqus. The B32 element is a three-dimensional *Timoshenko (quadratic)* element [44].

6.3 Nonstructural mass

It is essential to include the nonstructural mass to replicate the actual building precisely. This model is not made for static calculations, but for obtaining the natural frequencies and mode shapes. That is the reason for replicating the nonstructural mass, instead of using the conservative Eurocode. The nonstructural mass makes the frequencies more realistic when including the actual loads and not the loads in the Eurocode. The loads in the Eurocode are for static design and deflections, and they are therefore more conservative than an accurate estimate.

To estimate the nonstructural mass calculation, or live load, SiT's list of inventory [45] from their web page has been used. This list does not include details such as manufacturer, but includes the quantity of most of the inventory. The building manager have been helpful and reported some of the larger and heavier items manufacturer and model names. The building manager provided information about the stoves, refrigerators, and bathroom modules. Minor things were estimated by researching the typical weight of a similar product.

There is uncertainty about how much the residents' personal belongings weigh. The building manager could report that the resident's belongings could vary from a toothbrush, large gaming setups, or multiple instruments and amplifiers. Therefore this must be thought of as a qualified guess made with the help of the building manager and fundamental assumptions of commonly used items in a student housing. Since the chosen acceleration recordings are taken when the resident activity is assumed high, all the residents are included in the mass calculation.

The estimate of the nonstructural mass calculations results to 35t of nonstructural mass on every floor. The mass is lumped on the CLT floor and spread across the area.

The layer of screed and plaster is also a nonstructural mass, but separated into a independent mass. To calculate the contribution for screed and plaster it is used density, layer thickness, and area.

The detailed calculations of the nonstructural mass can be found in Appendix F.

This is the resulting nonstructural mass for each CLT floor:

Table 6.5: Total nonstructural mass

Group	Weight [kg]
Dorm	1772.1
Bathroom in dorm	12800
Entrance	170.2
Hallway	100.96
Common area and kitchen	1050.07
Personal belongings	2100
Windows and doors	2074.89
Outer cladding	13300
Elevator	1333.34
Total	$\approx$ 35 000

6.4 Assembly
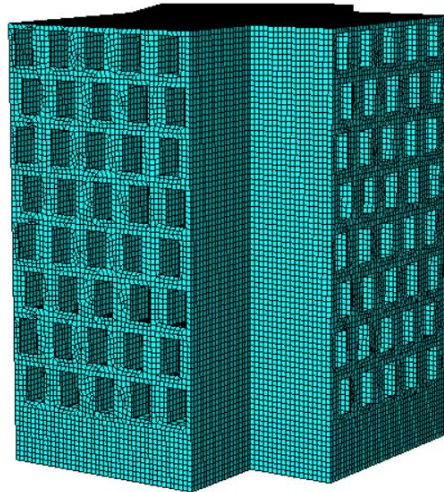
Figure 6.4: The mesh in the building

The first storey of the model is made in concrete and the top eight storeys in CLT. The first storey have a more open interior layout with columns and fewer walls, compared to the CLT storeys. The CLT storeys have an identical interior layout. Woodplan has shared their drawings, which shows a detailed layout with the different sections and materials used. The buildings are connected by steel plates and screws. There is no straight forward method to design the connection stiffness for CLT buildings in a FE-program. However, there is research, with varying methods, that obtains good results on the topic [46]–[49]. At low-amplitude movements the connections operate below their strength and the load transfer is predominately in the friction and direct contact between the panels [49]. Due to the slip in the

screws, the behaviour in the CLT connections is nonlinear [48]. These connections are simplified to be linear connections where the walls and floors meet in the building. The connections involving concrete are fixed.

The walls in the separate storeys are modelled as rigid to each other. Thus creating one part for each storey, with the walls as separate sections. The different storeys and floors have been tested with hinged and rigid connections. In the final model, hinged connections are chosen. The reason for this is three things: mainly because connections in timber buildings do not have the rigidity to be calculated as if they are 100% rigid. Secondly, because a CLT building is constructed as a house of cards, there are no large moment forces between the connections and the forces are distributed in shear. Lastly, the model with rigid connections proved that the differences did not vary much from a hinged building, except for some small increment in the frequencies. An alternative is to model connections with slip or a limited flexibility, but without further research of the used connections, this would be based on guessing and updating the model. Therefore this approach is not used.

It is uncertain how the screed is bonded to the CLT floor in the buildings at Moholt 50|50. It could be no interaction, incomplete interaction, or complete interaction. With no interaction, it is added as a nonstructural mass. When completely interacted it is added as layer to the shells and represent a joint section together with the CLT. However, if it is incomplete interaction, is neither two separate sections or a completely bonded to each other. The shear force are transferred between the CLT and concrete causes a sliding in the joint that is not negligible [15]. To design this it is usually avoided to use incomplete interaction when designing a composite floor. If the number of shear is sufficiently large and/or use shear connections with extremely high shear stiffness, then the composite floor can be designed as complete interaction. If not, the floor can be designed as no interaction [15]. Since it is unknown how the bonding is at Moholt 50|50, both types of floor is tried.
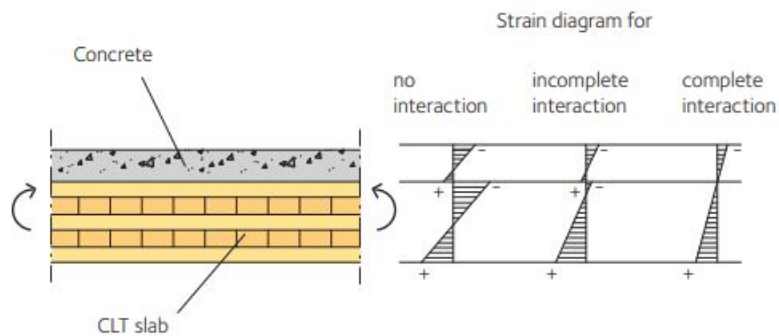
Figure 6.5: Illustration of different floor interactions

Source: [15]

6.5 Extracting data from Abaqus

A separate step is needed in Abaqus to extract the dynamic properties of the building. When doing a job in *Lancos Eigenvalue solver* it calculates the building's natural frequencies and mode shapes. This step makes both the relevant data and animations available in Abaqus.

The focus of this model is to extract the three first mode shapes and frequencies. The model, and the experimental data, have shown a big step in frequency from the first three modes to the fourth. The experimental data shows limited oscillation in the higher modes. With a more extended time series and larger loads, the higher modes could also be compared.

6.5.1 Mode shape vectors

A mode shape is a collection of node displacement vectors. In the experimental data at Moholt, four accelerometers are utilised in the measurements. Thus, the mode shapes extracted in the experimental data, for in-plane measurement, are based on the four displacement vectors or mode shape vectors. MAC (see section 3.6) is a criterion used to compare two mode shapes. The displacements in the Abaqus model are extracted with the *Query* tools. To represent the numerical mode shape vectors, nodes that replicate the accelerometers' location best are chosen. The rejection level value varies between 0 and 1, as seen in section 3.6, where 1 is a perfect match and 0 is orthogonal vectors. A typical MAC rejection level is 0.8 [28].

During the process of making the numerical model, there have been used different approaches to model the building with different build-ups. These possible build-ups of elements have been tried: homogeneous shells, composite shells, different engineering constants, screed as a structural material, screed as a nonstructural mass, stiff floors, and without stiff floors. Different approaches with different solutions, which have been tried and tested in the model. Using homogeneous shells is a method used in [4], [50], which requires different engineering constants than composite shells. The frequencies vary between the different build-ups, but they do not deviate from the experimental data frequencies. The solution that proved to replicate the experimental data the best is the solution with: composite shells in the walls and floors, CLT properties in the floors, with screed added as a nonstructural mass, and using the engineering constants from Dahl's work [40]. A comparison of the MAC values from different build-ups is found in table 9.3, section 9.5.2

Chapter 7

Experimental Results

This chapter presents and explains the results of the measurements made of the building named MAL2. A detailed presentation of the results from the other buildings can be found in appendix B-E. For each building (except MAL8), three full six hour recordings was obtained. For the results in this chapter, only one of these recordings is used, unless stated otherwise. The captions for the figures and tables states which file is used for the result.

Having five buildings to measure, meant limited time to record. The buildings was therefore measured on arbitrary days between 22nd February and 3rd March 2022, meaning that the wind load have not been taken into consideration when picking the six hour recording to present the results. However, the amount of traffic in the buildings was considered. The chosen recordings are therefore the ones recorded at a time with the most expected traffic, i.e. when most residents are expected to be home and using the building.

7.1 Moholt Allmenning 2

This section presents the results obtained from the vertical measurements at MAL2. The recordings of this building was made on the 22nd and 23rd of February. The following files are used for the results:
- 2022-02-22-18-00-00Z
- 2022-02-23-00-00-00Z
- 2022-02-23-06-00-00Z

7.1.1 Stabilisation Diagram

Figure 7.1 displays the stabilisation plots from the six hour recording on 22nd February 2022 18.00-00.00 UTC+0 from accelerometers A1, A3, and A4. The data from accelerometer A2 was omitted because its placement deviates from the other three accelerometers in the global Y-direction. The plot in global Y-direction shows three clear dotted lines which represents the first three modes, from left to right: first mode, second mode, and third mode. It also shows tendencies of a higher order mode at approximately 46 rad/s. This mode is left out of the results. The plot in global Z-direction shows two clear dotted lines which represents the first and third mode, respectively. An incomplete line appears at approximately 38 rad/s which could indicate a higher order mode in Z-direction. Both plots shows some spurious stable poles, i.e. poles that met the stability criteria but is unrelated to the modes. These were filtered out by the process described in appendix H. At the top of each plot, the stability criteria for the poles is stated but is reproduced here for simplicity.

- $\omega_n < 0.01$

- $\xi_n < 0.05$

- MPCW > 98

- Stability level = 3
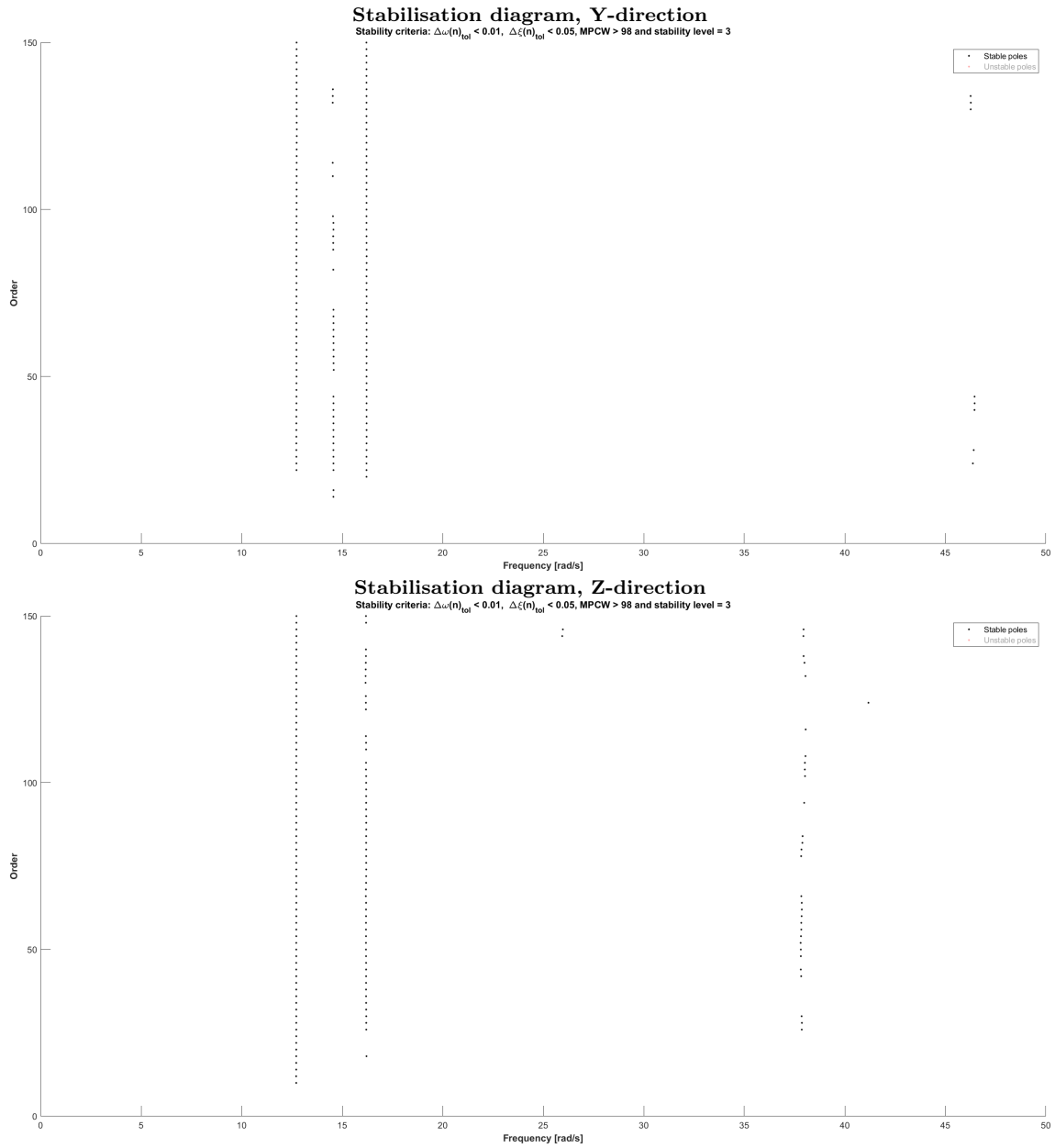
Figure 7.1: Stabilisation diagrams from 6hr recording, 2022-02-22-18-00-00Z

7.1.2 Power Spectral Densities

Figure 7.2 displays the one-sided Power Spectral Density obtained from MAL2, in the Y-direction and Z-direction, respectively. The PSD's were obtained by Welch's method with a Hanning window with 50% overlap. The PSD's were created with the acceleration data from accelerometer A1, since this was placed on the top storey. The PSD plots from the remaining buildings are presented in appendices B-E.
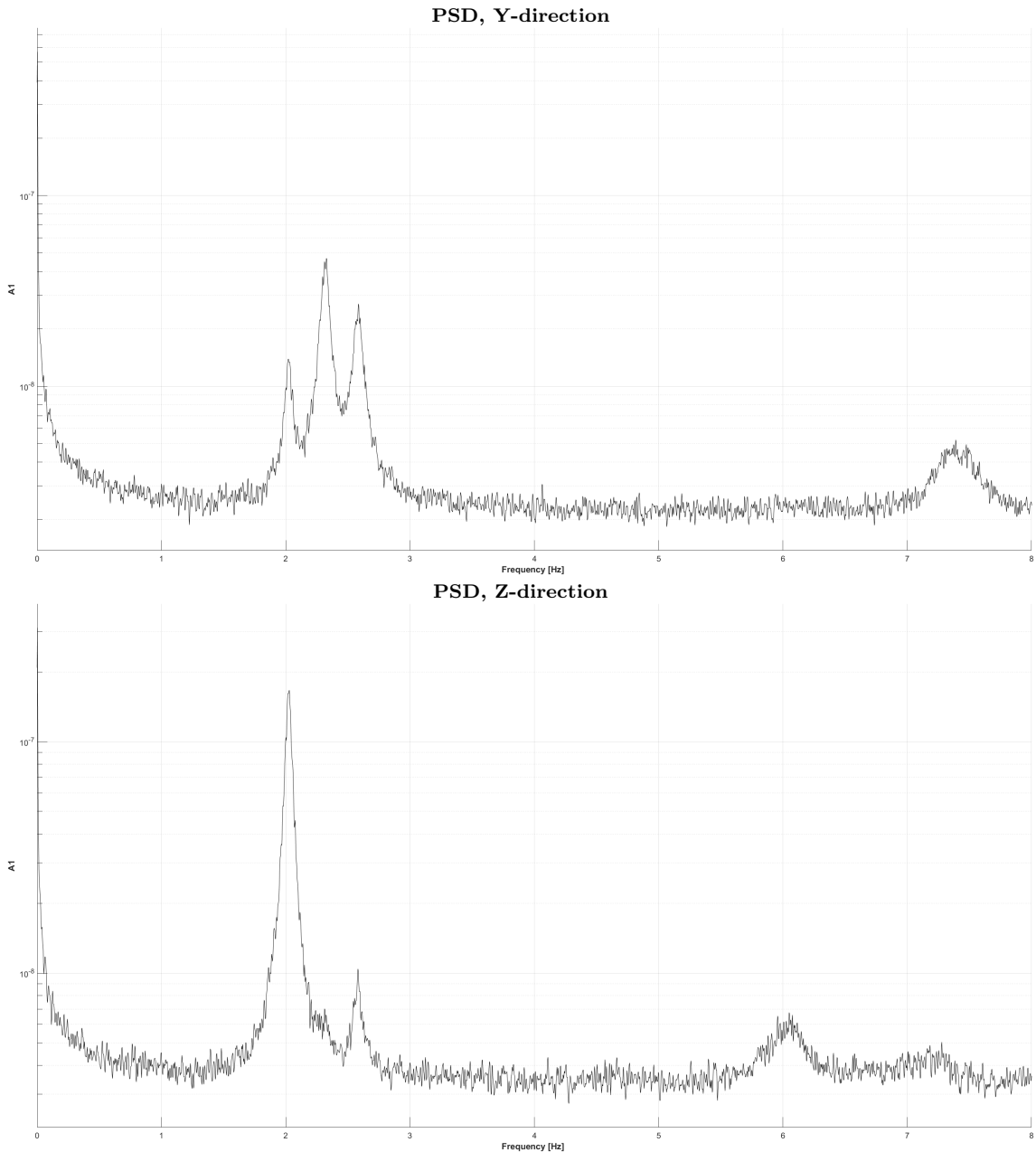
Figure 7.2: Plots of PSD from accelerometer A1, 6hr recording, 2022-02-22-18-00-00Z

7.1.3 Natural Frequencies

Table 7.1 displays the mean natural frequencies obtained from DD-SSI of the measurements at MAL2. All three full 6hr recordings were used in the calculation. The second and third column displays the Standard Deviation (SD) of the obtained frequencies and the number of stable poles found related to the modes, respectively. A description of how the data was processed to find the mean natural frequencies can be found in appendix H.

Table 7.1: Natural frequencies at MAL2, including standard deviation and number of stable poles

Mode	$f_n[Hz]$	$\sigma_{f_n}[Hz]$	SP	$f_{n,PSD}[Hz]$
1	2.022	0.0006	338	2.029
2	2.315	0.0010	169	2.329
3	2.572	0.0014	323	2.583

7.1.4 Damping

Table 7.2 displays the mean damping value obtained from DD-SSI of the measurements at MAL2. All three full 6hr recording were used in the calculation. The second and third column displays the SD and number of stable poles, respectively.

Table 7.2: Damping values for MAL2, including standard deviation and number of stable poles

Mode	$\xi_n[\%]$	$\sigma_{\xi_n}[\%]$	SP
1	1.357	0.017	338
2	1.577	0.048	169
3	1.711	0.063	323

7.1.5 Mode Shapes

Table 7.3 displays the mode shape vectors obtained from the full 6hr recording *2022-02-22-18-00-00Z* at MAL2, derived by DD-SSI. Each individual mode shape vector is obtained from a single stable pole (one dot in the stabilisation diagram), i.e. a pole that satisfied the criteria set in section 3.5. The direction row in the table refers to which direction of accelerometer data that were used in the DD-SSI, and the order row refers to which model order the pole were collected from, i.e. the ordinate axis of the stabilisation diagram (figure 7.1). For the third mode, mode shape vectors for both directions are included since this is a torsional mode. All mode shape vectors are normalized.

Table 7.4 shows an average of all normalized mode shapes, where every stable pole related to a natural frequency is taken into account. This provides a picture of how similar the mode shape vectors are, regardless of the chosen model order.

Figure 7.3 shows the plots of the vertical mode shapes obtained from the DD-SSI of MAL2. Each pole in the stabilisation diagram can be used to generate a plot. The three first plots stem from model order 60 and the last plot stem a pole of model order 64.

Table 7.3: Normalised mode shape vectors from MAL2, recording *2022-02-22-18-00-00Z*

Accelerometer	Mode 1	Mode 2	Mode 3	Mode 3
A1	1.0000	-1.0000	1.0000	1.0000
A3	0.6296	-0.5948	0.6957	0.6699
A4	0.1955	-0.1694	0.2318	0.2981
Direction	Z	Y	Y	Z
Order	60	60	60	60

Table 7.4: Average of all normalised mode shape vectors from MAL2, recording *2022-02-22-18-00-00Z*

Mode 1	σ_1	Mode 2	σ_2	Mode 3	$\sigma_{3,Y}$	Mode 3	$\sigma_{3,Z}$
1.0000	0.0000	1.0000	0.0000	1.0000	0.0000	1.0000	0.0000
0.6383	0.0079	0.5959	0.0067	0.7003	0.0109	0.6475	0.0268
0.1961	0.0065	0.1743	0.0081	0.2237	0.0063	0.2979	0.0236
Z		Y		Y		Z	

(a) Mode 1

(b) Mode 2

(c) Mode 3, Z-direction

(d) Mode 3, Y-direction
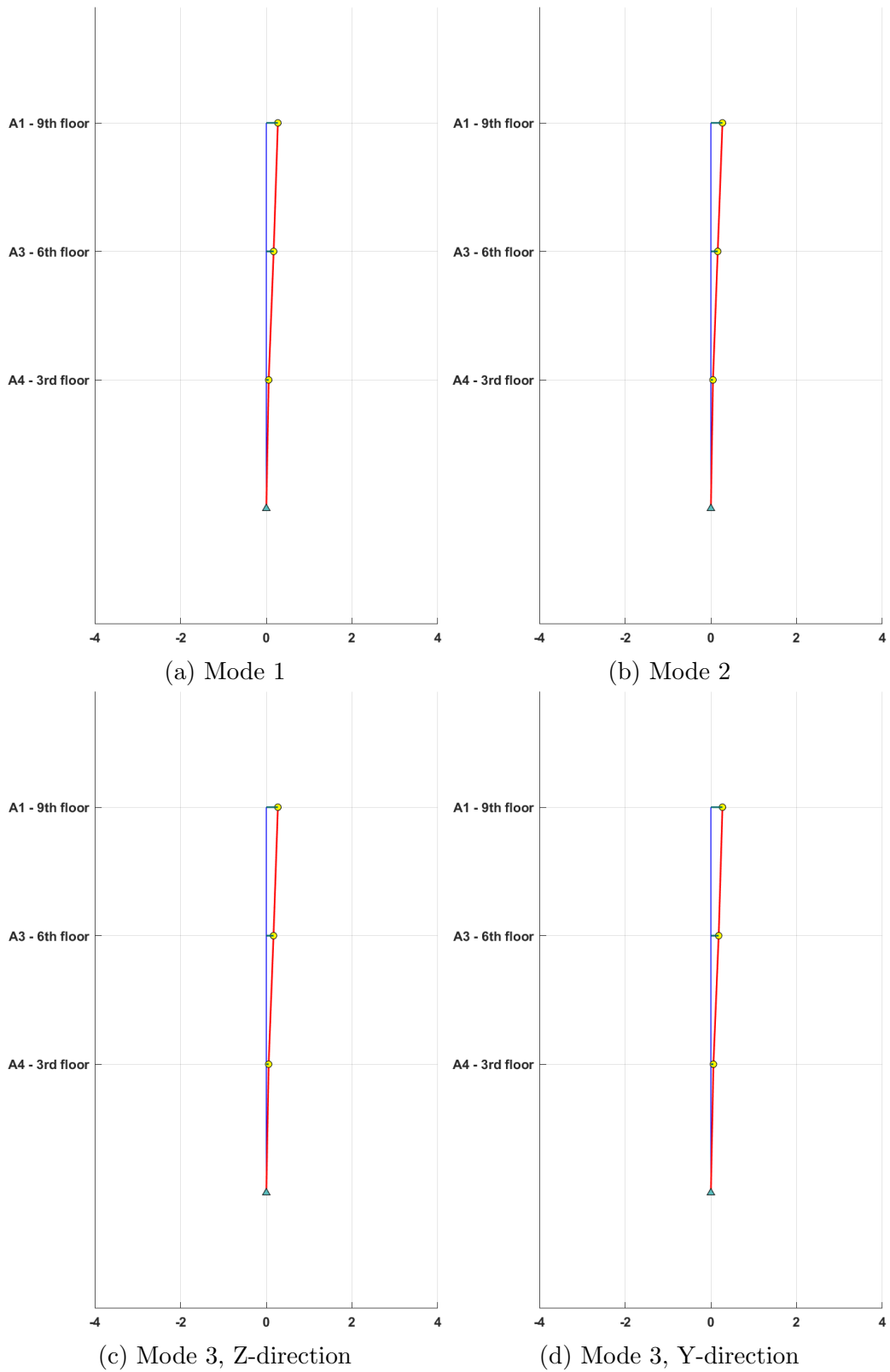
Figure 7.3: Illustration of vertical mode shapes at MAL2

(a) Mode 1

(b) Mode 2

(c) Mode 3, Z-direction

(d) Mode 3, Y-direction
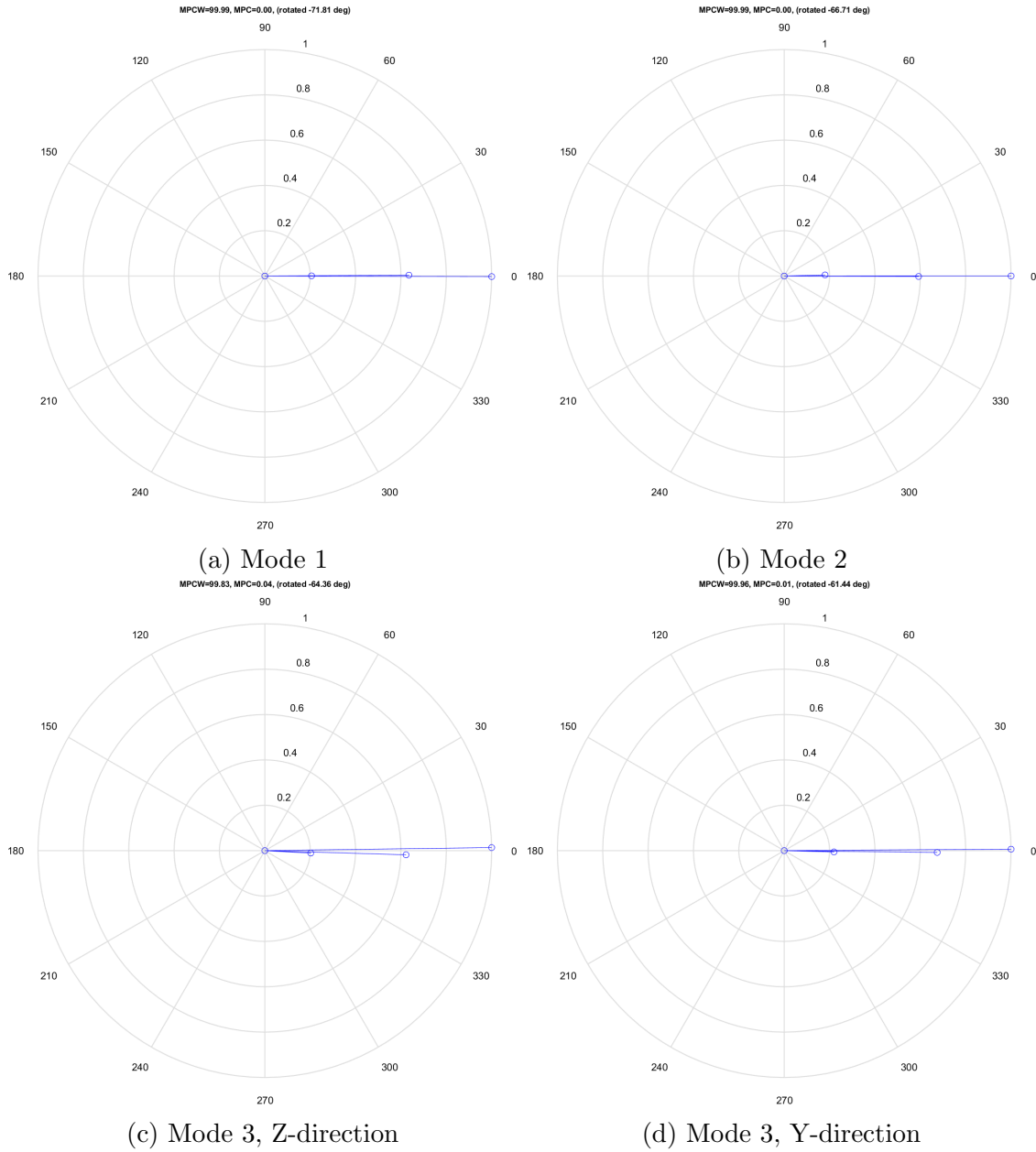
Figure 7.4: Plots of the mode shapes in the complex plane

7.1.6 Peak Acceleration

Table 7.5 displays the peak accelerations obtained from the four accelerometers from the full 6hr recording *2022-02-22-18-00-00Z*. The accelerometers measures the acceleration in volts. In order to convert the signal to $[m/s^2]$, the signal was multiplied by a factor of 4.905 [35]. The signal was filtered through a 10th order *Butterworth filter* with MATLAB's butter function, to discard irrelevant frequency components, and a high pass filter with MATLAB's highpass function to discard frequencies close to Direct Current (DC). This procedure was applied to all three full 6hr recordings of MAL2 in order to find the highest value from the available measurements.

Table 7.5: Peak accelerations at MAL2

Accelerometer	Y-direction$[m/s^2]$	Z-direction$[m/s^2]$
A1	0.0048	0.0063
A2	0.0047	0.0056
A3	0.0035	0.0045
A4	0.0037	0.0041

7.2 In-plane measurements

In addition to the vertical measurements in the staircase, two more measurement schemes were performed for building MAL2, described in section 4.4.2. These measurements were performed to observe how the building behaved in the YZ-plane for the three modes. It should be noted that the in-plane measurements were processed with Covariance Driven Stochastic Subspace Identification (Cov-SSI), and not DD-SSI like the rest of the results. The Cov-SSI was used for convenience since the Department had provided a script where this was used. The Cov-SSI and DD-SSI should yield the same result. The in-plane measurements were performed during working hours on the 5th April 2022.

7.2.1 Measurements on the 9th storey

Figure 7.5 displays the three mode shapes obtained from the measurements on the 9th storey. The modes are oriented in the same manner as figure 4.7. The four points represents the placement of the accelerometers. The dashed lines is the initial placement of the storey and the solid lines shows the scaled maximum displacement of the storey. The initial placements of the accelerometers, needed for the scripts, were estimated by using a architectural model of the building made by Woodplan.

The way the accelerometers were set up, meant there were three different orientations. In order to convert all accelerometers to the global axes, the following equations were used. The denotations $()_G$ and $()_L$ refers to the global axes and local axes, respectively.

Accelerometer A1:
$$Y_G = -Z_L \cdot \cos(25°) - Y_L \cdot \sin(25°) \qquad (7.1)$$

$$Z_G = -Z_L \cdot \sin(25°) - Y_L \cdot \cos(25°) \qquad (7.2)$$

Accelerometers A3 and A4:
$$Y_G = Z_L \qquad (7.3)$$

$$Z_G = -Y_L \qquad (7.4)$$

7.2.2   Measurements on the 7th and 9th storey

To find the in-plane mode shapes for the 7th storey a different setup of the accelerometers was deployed. The accelerometer A1 remained in the same place on the 9th storey as for the measurements described in 7.2.1. Accelerometer A2, A3, and A4 was moved to the 7th storey, were A2 was installed directly underneath A1, and A3 and A4 was placed in the corners opposite to each other, as shown in figure 4.8. To convert the accelerometer data to the global axes, accelerometer A1 and A2 was adjusted according to equations (7.1) and (7.2), and A4 was adjusted according to equations (7.3) and (7.4).

In order to get the mode shapes from 7th and 9th storey simultaneously, scaling of the measurements on the 9th storey were used. To find the scaling ratio, the maximum normalized displacements from accelerometer A2 was divided by the maximum normalized displacements of accelerometer A1:

$$c_z = \frac{\Phi_{A2,z}}{\Phi_{A1,z}} \qquad c_y = \frac{\Phi_{A2,y}}{\Phi_{A1,y}} \qquad (7.5)$$

These scaling factors were then multiplied to the maximum normalized displacements obtained from the measurements on the 9th storey to find the equivalent normalized displacements on the 7th storey. Figure 7.6 displays the three mode shapes on the 7th and 9th storey, where the mode shape on the 7th storey is obtained thru the scaling method.
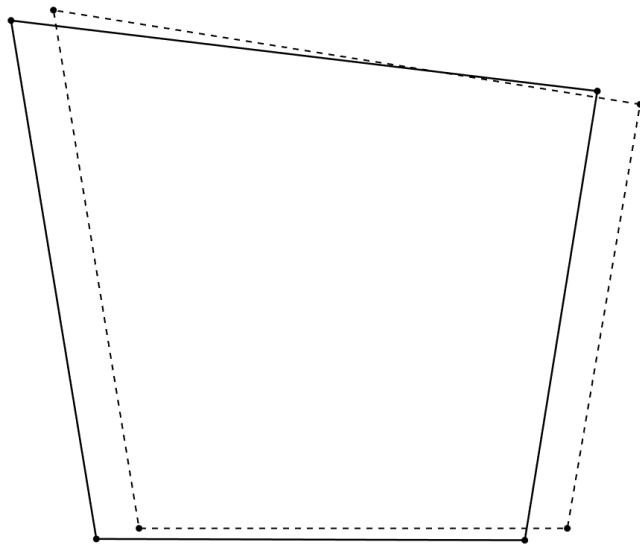
(a) Mode 1
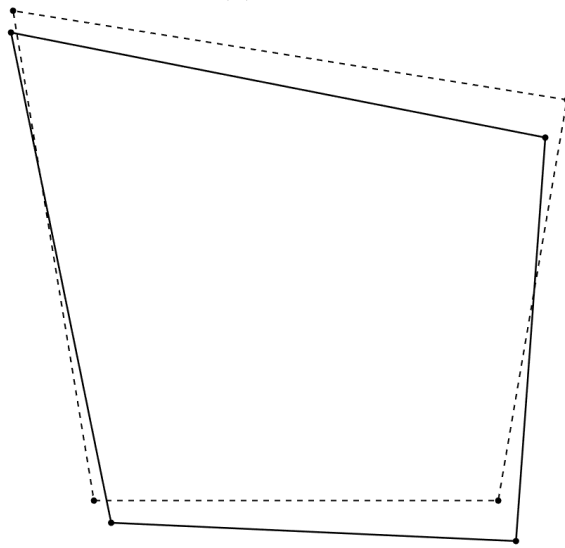
(b) Mode 2
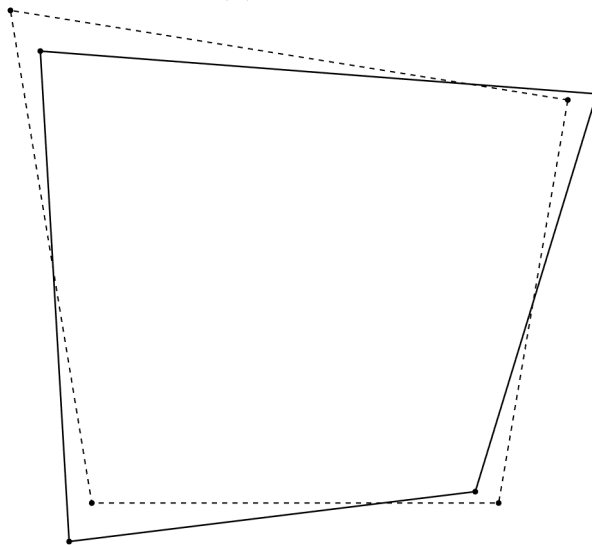
(c) Mode 3

Figure 7.5: Mode shape plots from in-plane measurements on the 9th storey of MAL2
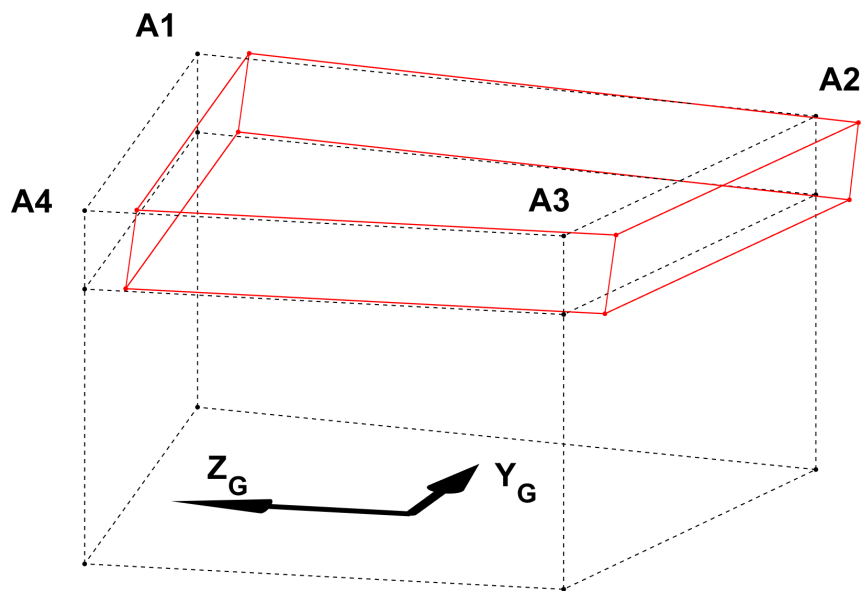
(a) Mode 1
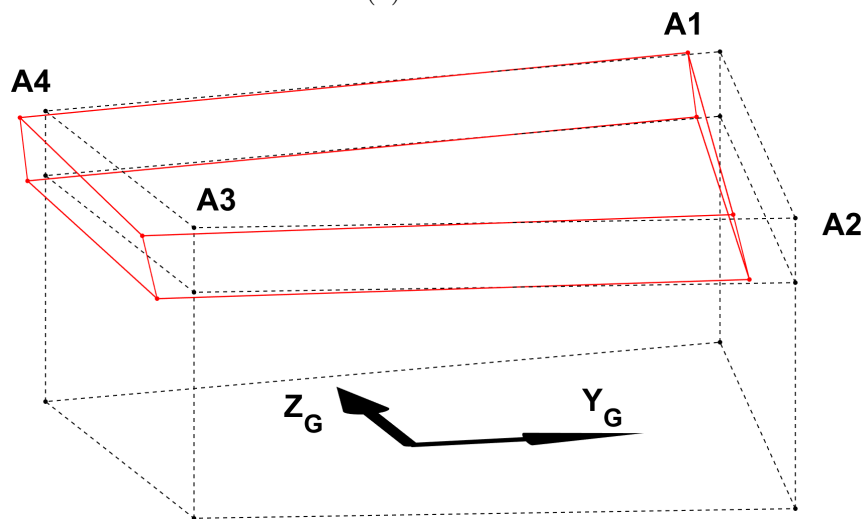
(b) Mode 2
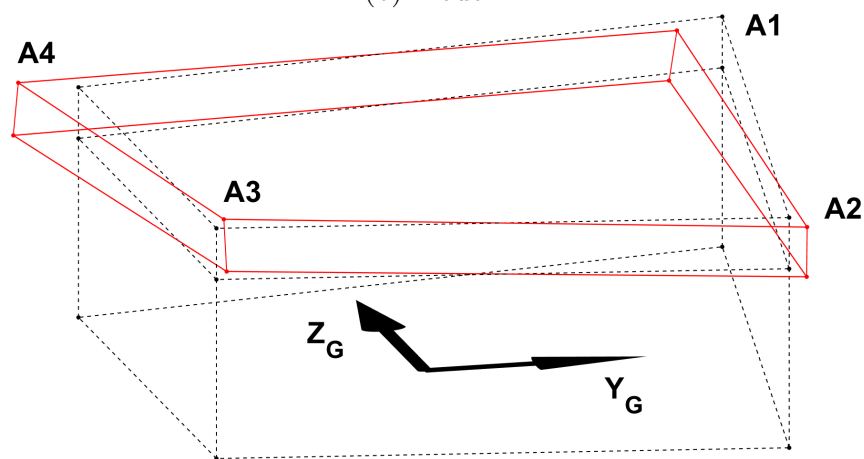
(c) Mode 3

Figure 7.6: Scaled mode shape plots from in-plane measurements on the 9th and 7th storey of MAL2

Chapter 8

Numerical Results

8.1 Numerical model

The results from the numerical model are presented in this section. The results presented are from a model with hinged connections, nonstructural mass of 35t lumped at the CLT floors and distributed over the area, with engineering constants from Dahl's work [40]. Different solutions with composite or homogeneous shells have been tried with different engineering constants. The frequencies have not changed much between the different solutions, but the MAC values presented in 8.1.3 have.

8.1.1 Natural frequencies

The natural frequencies in the model have shown to be coupled with the nonstructural mass more than the structural elements. The resulting natural frequencies in the model is slightly off for the second and third mode, but is precise for the first mode.

Table 8.1: Natural frequencies in numerical model and measured frequencies of MAL2

Mode	Natural frequency [Hz]	Natural frequency in experimental data [Hz]
1	2.0005	2.022
2	2.1464	2.315
3	2.4614	2.572

8.1.2 Mode shapes

The three first mode shapes is presented here. It is not focused on the higher order modes in this thesis.

First mode

The first mode shape is chiefly a translation mode shape. The irregular translation shape is believed to be caused by the irregular shape of the building. The building has a slight torsional movement in the first mode.
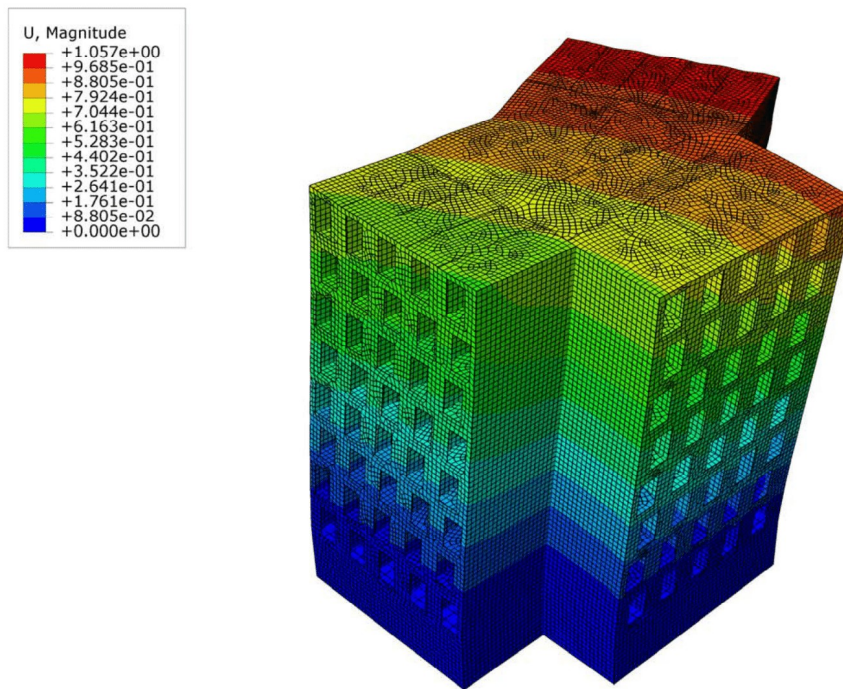
Figure 8.1: Illustration of the first mode shape

Second mode

The second mode shape is chiefly torsional. As displayed by the figure, the torsion origin is in one of the wings of the buildings. This creates a torsional movement close to the origin, but further away from the origin the movement is more similar to a translation movement. Thus, the accelerometers furthest away from the origin may not show the torsional movement.
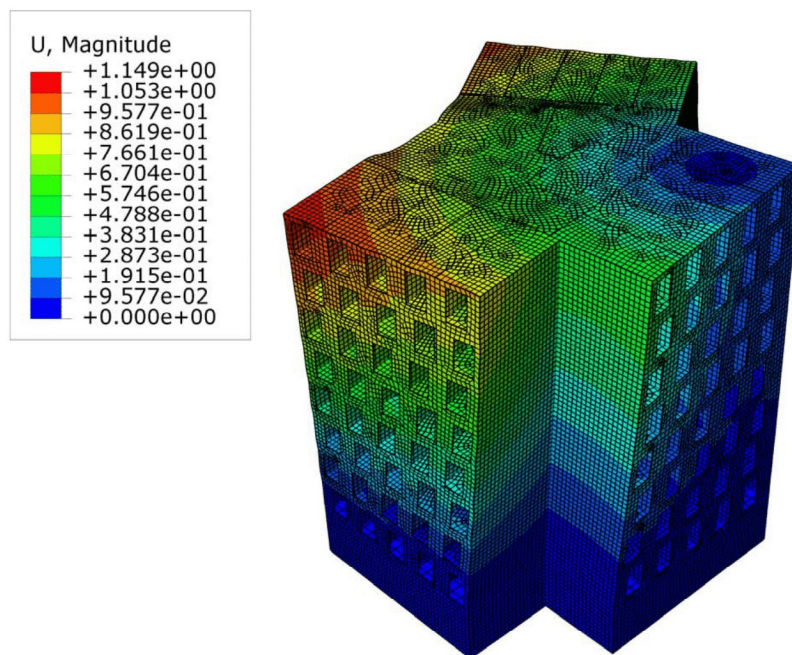
Figure 8.2: Illustration of the second mode shape

Third mode

The third mode shape is a combination of torsional and translation mode. It is chiefly a torsional mode, but the origin of the torsion is outside of the building. This creates an effect where the rotation of the building is approaching a translation movement. The effect is similar in mode 2, but is more significant in mode 3.
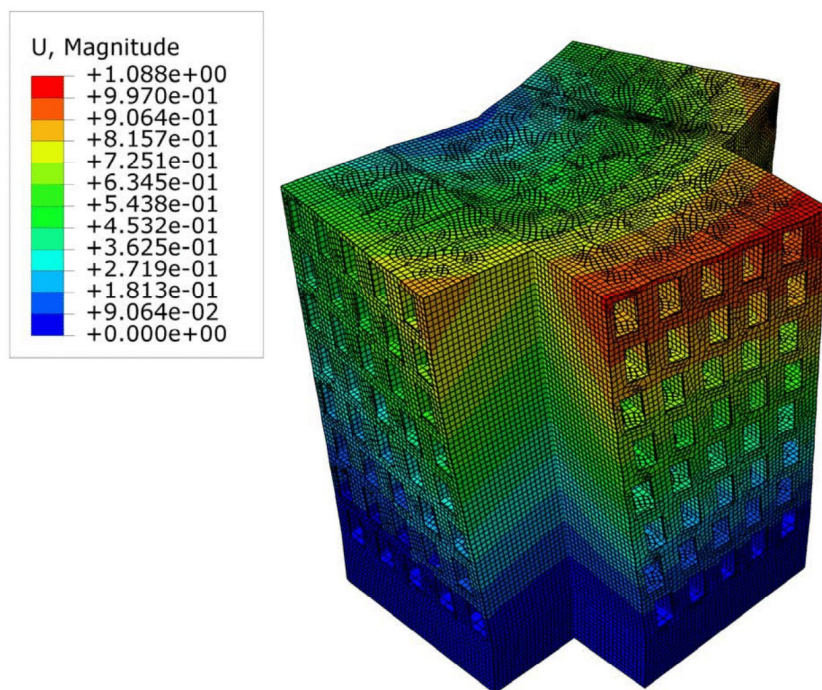
Figure 8.3: Illustration of the third mode shape

8.1.3   MAC - experimental and numerical in the 9th storey

The MAC assessment for the numerical mode shape and the measured mode shape of MAL2 are presented in table 8.2. The value that matters is the diagonal between the modes. The values read 0.8100, 0.7861, and 0.8385. A typical MAC rejection level is 0.8 [28]. Thus the MAC values for mode 2 are under the rejection level.

As explained in section 6.5.1, it has been tried and tested with different build-ups, and this is the build-up that provides the best MAC values for the comparison with the experimental data.

Table 8.2: MAC assessment of the numerical and measured mode shape on the 9th storey

	Mode	Numerical model		
	Mode	1	2	3
	3	0.0107	0.0878	0.8385
Measured	2	0.1555	0.7861	0.0351
data	1	0.8100	0.1127	0.0037
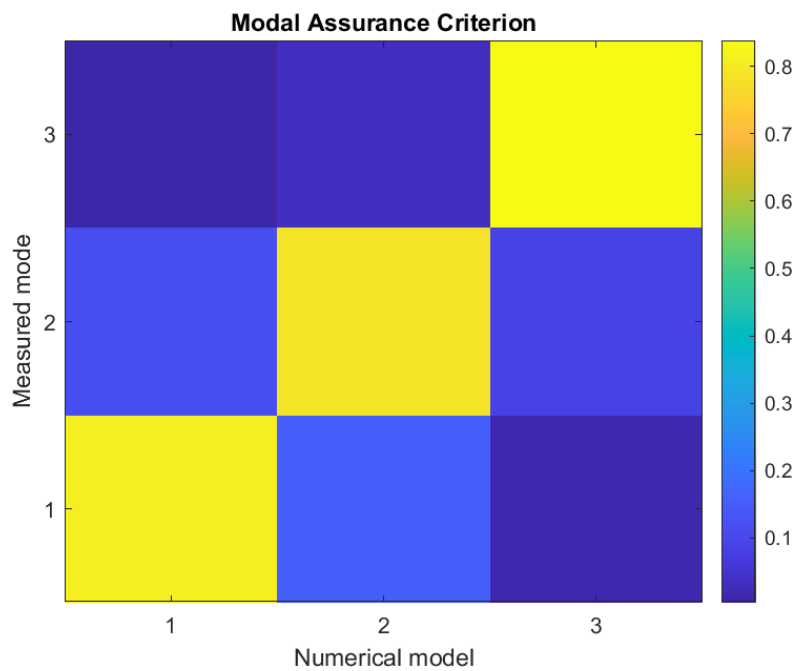
Figure 8.4: Contour plot of MAC matrix

8.1.4 MAC - experimental and numerical in the 7th and 9th storey

The MAC assessment for this comparison shows that the first and second mode is well below the rejection level, but the third mode is adequate. This is discussed in section 9.5.3.

Table 8.3: MAC assessment of the numerical and measured mode shape on the 7th and 9th storey

| | Mode | Numerical model | | |
		1	2	3
	3	0.2661	0.0395	0.8181
Measured	2	0.3719	0.7469	0.0009
data	1	0.6555	0.1022	0.0626
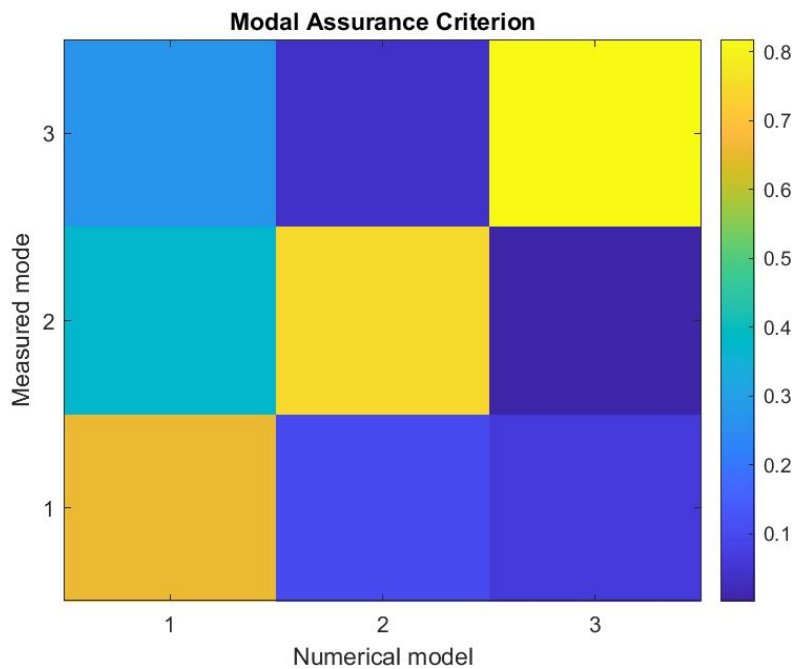
Figure 8.5: Contour plot of MAC matrix

8.2 Calculations using Eurocode

In addition to calculations from the measurements, the peak accelerations for all buildings were calculated following the procedure described in Annex B and Annex C in NS-EN 1991-1-4 [2]. This section explains the calculations and the choices made in them. The detailed calculations can be found in appendix G.

8.2.1 Theoretical mode shapes

In order to calculate the peak accelerations from the procedure in Annex C, determining whether the mode shape of the building was linear or parabolic was necessary. A comparison of the recorded mode shape and the two theoretical mode shapes was performed to decide this, which is covered in the next section. The linear and parabolic mode shape is based on the two equations:

$$g(x) = ax + b \qquad (8.1)$$

$$f(x) = ax^2 + bx + c \qquad (8.2)$$

To find the constants a, b and c, a set of Boundary conditions (BC) is needed. The first BC is the displacement at the top storey. This is set equal to 1 to represent the normalized displacement, same as the mode shapes in section 7.1.5. For the second BC, an assumption of the normalized displacement on the second storey was made. This is where the CLT is connected to the concrete base. The assumption is based on the fact that concrete is stiffer than the CLT, thus yielding a smaller displacement on the second storey compared to a full CLT building. The displacement is assumed to be small, so for practicality the second BC is set to:

$$g(1) = 0 \qquad f(1) = 0 \qquad (8.3)$$

For the parabolic mode shape, a final BC was needed. A small tilt of the concrete storey is assumed. The assumption is made from the expectation of some bending actions in the concrete. The tilt is assumed so small, that for practicality the BC is set to:

$$\frac{df(1)}{dx} = 0 \qquad (8.4)$$

Figure 8.6 and 8.7 displays the theoretical mode shapes found from equations 8.1 and 8.2. Figure 8.7 displays the mode shapes where the stiffness of the first storey is considered to be greater than the top eight storeys, with BCs in (8.3) and (8.4).

To further clarify equations (8.1) and (8.2), x=0 is the ground storey, x=1 is the second storey, and x=9 is top of the building, i.e. the roof.

(a) Linear (b) Parabolic
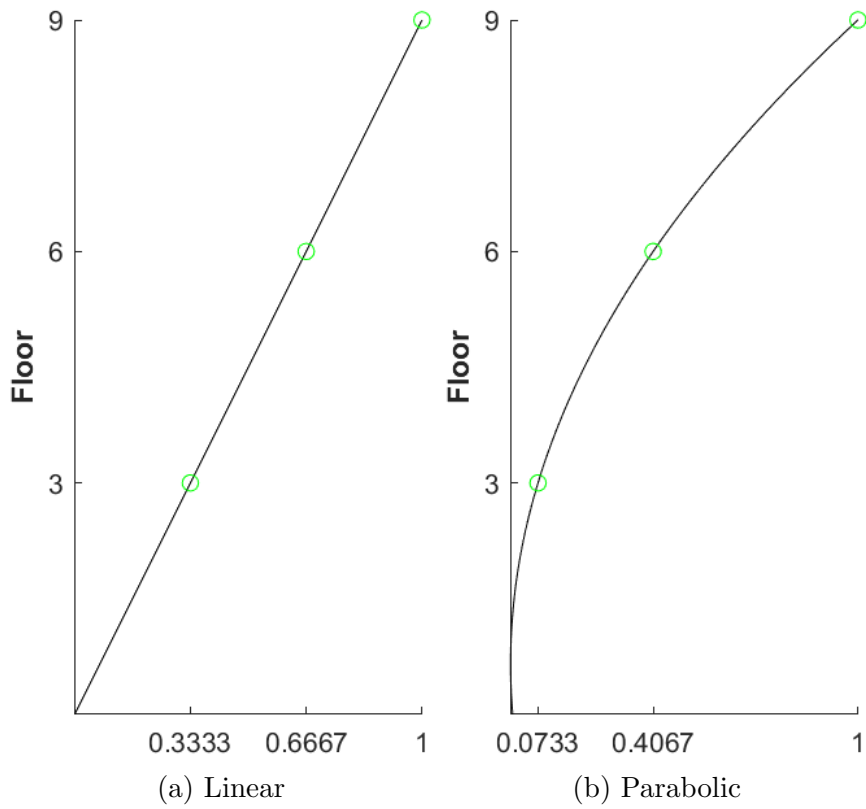
Figure 8.6: Plots of the theoretical mode shapes

(a) Linear (b) Parabolic
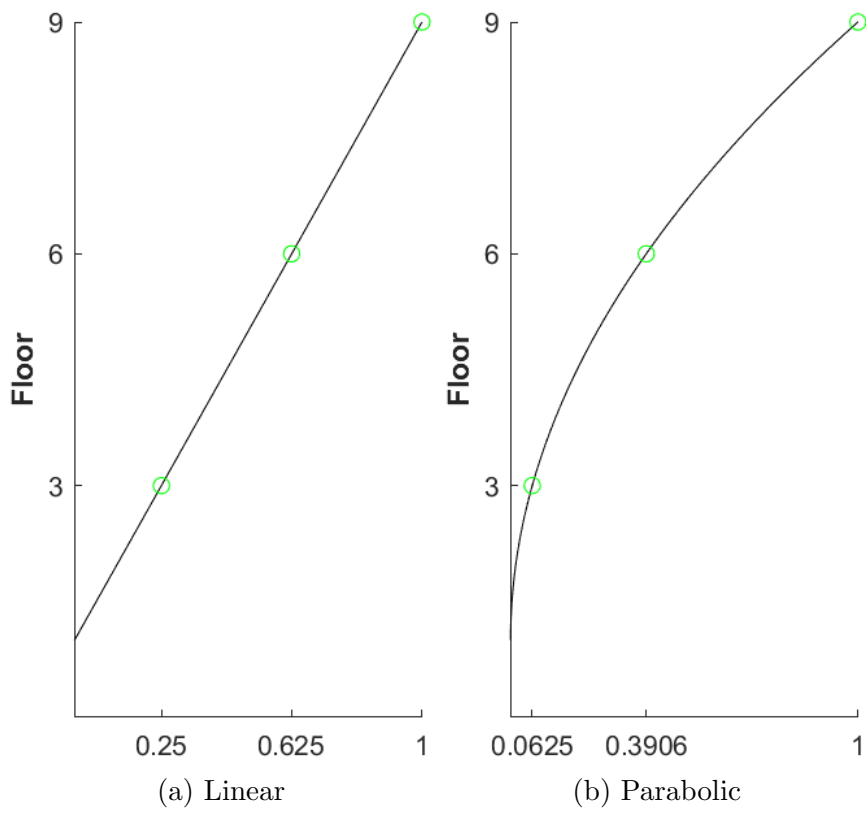
Figure 8.7: Plots of the theoretical mode shapes with BC

8.2.2 Peak accelerations

The natural frequencies used in the calculations stem from the average frequencies for the first mode found with DD-SSI. They can be found in the experimental results in chapter 7 and appendices B-E, but are reproduced here for simplicity.

$$f_n = \begin{bmatrix} 2.022 & 1.978 & 1.985 & 1.939 & 1.959 \\ MAL2 & MAL5 & MAL7 & MAL8 & MAL11 \end{bmatrix} Hz$$

The structural damping values are also calculated with DD-SSI. The damping values used in the calculation are the averages of the damping values for each pole in the stabilisation diagram related to the first mode for every available six hour recording. The procedure in NS-EN 1991-1-4 uses logarithmic decrement of structural damping, δ_s, instead of the equivalent viscous damping, ξ, which is found in the DD-SSI. The values needed to be converted with the use of the relation $\delta_s = \xi \cdot 2\pi$, which yielded the following values for structural damping:

$$\delta_{s,n} = \xi_n \cdot 2\pi = \begin{bmatrix} 0.085 & 0.099 & 0.091 & 0.097 & 0.090 \\ MAL2 & MAL5 & MAL7 & MAL8 & MAL11 \end{bmatrix}$$

When deciding the force coefficient, c_f, the shape and size of the building are deciding parameters. NS-EN 1991-1-4 does not offer a specific solution for sections shaped like Moholt 50|50, only for rectangular shaped buildings, cylindrical-shaped buildings, or regular polygonal-shaped buildings, e.g. hexagonal shaped. As an approximation, it was decided to use the procedure for rectangular sections with the width of the largest facade, i.e. the facade with a 25-degree kink. Because the calculations are meant for wind perpendicular to a surface, the width was set equal to the length from corner to corner of the kinked facade, as shown in figure 8.8.
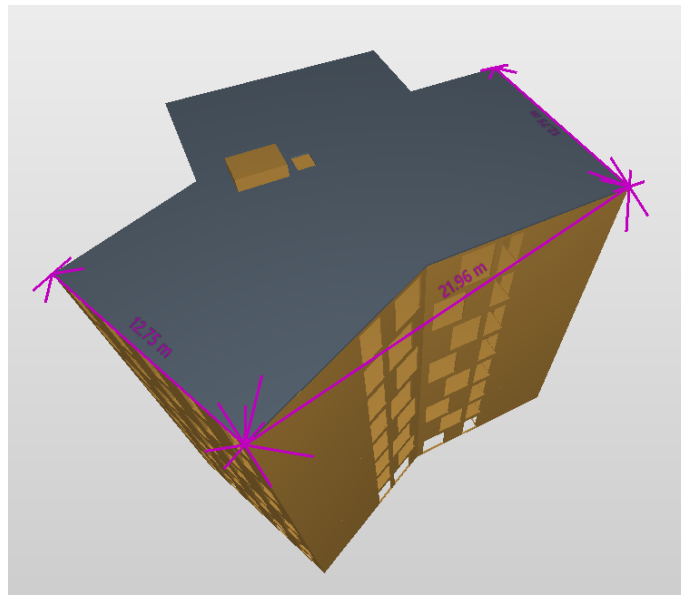
Figure 8.8: Illustration of the simplification of chosen wind surface for the procedure in Annex C

In the procedure of Annex C, determining the vertical mode shape was necessary, either linear or parabolic. To decide this, a comparison of the theoretical mode shapes and the measured mode shape was needed. Table 8.4 contains values from a MAC evaluation of the two translation modes between the theoretical mode shapes and the measured mode shapes. The linear theoretical mode shape with the boundary conditions given in section 8.2.1, yields the best results for all buildings. Therefore, it seems more likely that the buildings experience linear mode shapes. Since the MAC values for a parabolic mode shape is high too, and for the sake of completeness, the calculations in Annex C with constants for a parabolic mode shape is also performed.

Table 8.4: MAC evaluation of theoretical mode shapes and measured mode shapes

Building	Mode	Linear	Parabolic	Linear[1]	Parabolic[1]
MAL2		0.9880	0.9609	**0.9980**	0.9541
MAL5		0.9892	0.9593	**0.9984**	0.9524
MAL7	1	0.9906	0.9544	**0.9986**	0.9471
MAL8		0.9878	0.9647	**0.9981**	0.9582
MAL11		0.9879	0.9611	**0.9979**	0.9543
MAL2		0.9817	0.9720	**0.9954**	0.9663
MAL5		0.9809	0.9763	**0.9949**	0.9709
MAL7	2	0.9812	0.9691	**0.9950**	0.9631
MAL8		0.9764	0.9808	**0.9924**	0.9759
MAL11		0.9879	0.9611	**0.9972**	0.9622

[1] Theoretical mode shapes with boundary conditions described in section 8.2.1

Table 8.5 displays the peak accelerations calculated with the procedure in Annex B, Annex C with linear vertical mode shape, and Annex C with parabolic vertical mode shape. All calculations were performed with the mean wind velocity calculated from NS-EN 1991-1-4 and one year's return period. The return period used was considered to represent best the probability of faster gusts of wind on the day the building was measured.

Table 8.5: Peak accelerations according to NS-EN 1991-1-4, Annex B and Annex C

			Peak acceleration $[m/s^2]$		
Building	f_1 $[Hz]$	δ_s	Annex B	Annex C[1]	Annex C[2]
MAL 2	2.022	0.085	0.019	0.022	0.028
MAL 5	1.978	0.099	0.018	0.021	0.027
MAL 7	1.985	0.091	0.018	0.022	0.028
MAL 8	1.939	0.097	0.018	0.022	0.028
MAL 11	1.959	0.090	0.019	0.022	0.029

[1] Linear mode shape
[2] Parabolic mode shape

Chapter 9

Discussion

Within this chapter, the findings from all buildings are discussed and compared. The experimental results are compared to the numerical results, both to the numerical model and the calculations from NS-EN 1991-1-4. The results from the numerical model is assessed, and alternative solutions is discussed. The method of measurement is assessed.

9.1 Natural frequencies

Every stabilisation plot displays the natural frequencies of the respective buildings. The stabilisation plots in Y-direction give indications of the natural frequencies for the first three modes, including the first mode, which mainly is a translational mode in the Z-direction. The stabilisation plots in Z-direction displays frequencies for first and third mode only, which results in fewer stable poles for the frequency in the second mode, a recurring theme for all measurements. However, there is consistency in the frequencies obtained from the DD-SSI, with the highest SD found being 0.0015 Hz for mode three in MAL11 (table E.1).

Some stabilisation plots give indications of higher-order modes, e.g. figure 7.1, where a partially dotted line appears at $\approx$ 38 rad/s (= 6.05 Hz). Other stabilisation plots give more ambiguous indications of the higher-order modes. For instance, figure E.1 shows some stable poles scattered over a frequency range of 35-39 rad/s. Since there is little consistency for these higher-order modes from building to building, they are not accounted for in this thesis. In order to better register these higher-order modes, measurements over a more extended period would be required.

The frequencies found from DD-SSI coincide nicely with those found from the PSD, with a difference under 1%, confirming the frequencies. Like the stabilisation plots, the PSD plots display some higher-order modes. These modes exhibit less spectral strength than the first three modes for most of the recorded time series and often with a more rounded peak, making it difficult to interpret the frequency and mode.

Figure 9.1 displays a plot of the average natural frequencies for every building and natural frequencies from the numerical model. The figure shows a small spread of the measured frequencies, with the difference in the extrema being 0.084, 0.083, and 0.145 for the first, second, and third mode, respectively. A difference in either mass, stiffness, or both causes the spread of the natural frequencies. However, it is not easy to pinpoint precisely where the differences lie. Both stiffness and mass are unknown values. Nevertheless, some reasonable assumptions can be made. The structural mass and most nonstructural mass are considered equal from building to building. It is assumed that the only part of the nonstructural mass that fluctuates is the occupants' weight and possessions. This portion is $\approx 1\%$ of the estimated total mass, which has little effect on the frequencies. Thus, it seems more likely that the stiffness is the altering factor for the frequencies.

When comparing the buildings' natural frequencies, they all seem to follow the same pattern of incrementation from one mode to the next. This consistency gives an extra assurance of the accuracy of the measurements, where the buildings' frequencies confirm each other.

The numerical model is made to compare numerical values with the experimental data. Out of the data extracted, the natural frequencies are essential to ensure that the model replicates the actual buildings. A general numerical model is made for all buildings, because the buildings have negligible differences. Several different build-ups, material properties, and nonstructural mass have been tried to replicate the real-life buildings correctly. Different solutions resulted in different results, but the frequencies proved to be consistently similar. They regularly matched the experimental data with different build-ups, materials, and connections. Out of the changes performed on the numerical model, the nonstructural mass affected the natural frequencies the most. The values for the natural frequencies changed almost proportional to the changes in the nonstructural mass. The nonstructural mass is one of the uncertainties in the numerical model. Thus, time and consideration have been invested in ensuring a detailed calculation of the nonstructural mass. Calculations for the estimate of nonstructural mass can be found in appendix F.
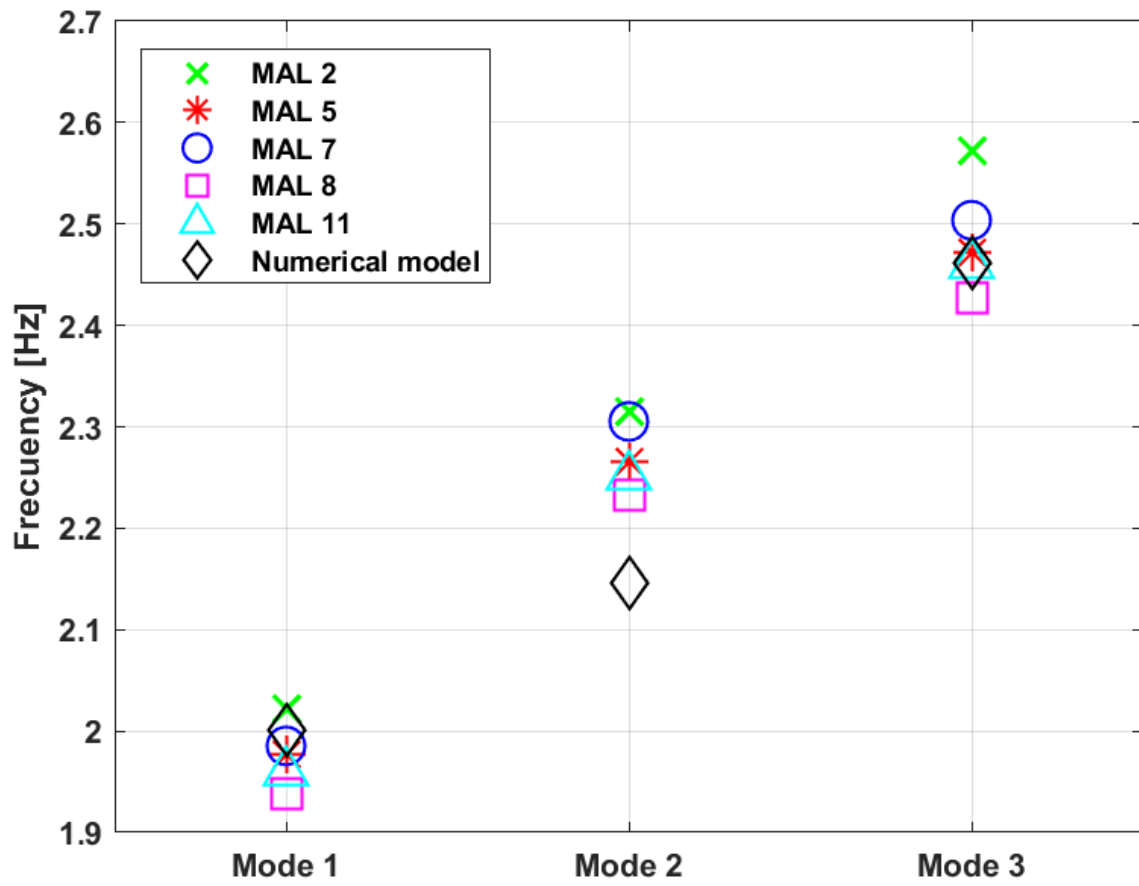
Figure 9.1: Comparison of the average frequencies for every building and the numerical model

9.2 Damping values

Similarly to the frequencies, a damping value is related to every pole in the stabilisation plot. From the looks of the SD, this value seems to be more fluctuating than the natural frequencies.

Figure 9.2 displays the average damping values for every mode of every building obtained from DD-SSI. Compared to the plot of the natural frequencies, the damping values are more scattered. There is no pattern between the damping values in either the modes or between the buildings. However, the averaged values all lie within a relatively small range, indicating consistency in the measured data. The highest averaged damping value found is 1.779 % in mode two for building MAL8, and the lowest value found is 1.357 % in mode one for building MAL2. In NS-EN 1995-1-1 [25], the damping ratio of a timber floor is assumed to be $\xi = 1.0\%$, which is in the proximity of the measured values.

In NS-EN 1991-1-4 [2], table F.2, approximate values of logarithmic decrement of structural damping for different types of constructions are presented. There is no approximated value for timber buildings. However, there is one for timber bridges. The approximated range is $\delta_s = [0.06, 0.12]$, which equates to $\xi_n = [0.95, 1.91]$ % in viscous damping. All averaged values in this thesis lie within this range, suggesting that the approximated range for timber bridges is apt also for timber buildings.

The damping ratios obtained in this thesis seem to coincide nicely with values from similar experiments on similar buildings. Measurements performed by Aloisio et al. [47] on an 8+1 (top eight storeys of CLT, first storey of concrete) storey CLT building with a CLT core yielded damping ratios ranging from 1.216 % for the first translational mode to 1.921 % for the first torsional mode. Lervik and Kristiansen [5] measured two CLT buildings with CLT cores, one with ten storeys and one with 13 storeys. The damping ratios ranged between 1.3710 % and 1.5663 % for the ten storey building and 1.1797 % and 1.445 % for the 13 storey building. Granted the small sample size, it is not possible to give a conclusion about the damping ratios. However, it is interesting to see that values obtained from all these buildings lie within a range of $\approx 0.8\%$.

Estimating the damping ratios is a complicated affair due to many affecting factors. A note in table B.2 in ISO10137 [1] states: "*Damping ratios depend on the type of construction, material, presence of nonstructural elements, age, quality of construction, and amplitude and frequency of vibration... For any form of construction, the type of joint and the type of bearing employed play an important role in damping. For floors, the presence of some floor and ceiling finishes and partitions can increase the damping considerably*". In this thesis, the damping ratios are only presented as a result of the measurements. In order to explain why the damping ratios are the way they are, more extensive research of the underlying factors is needed.
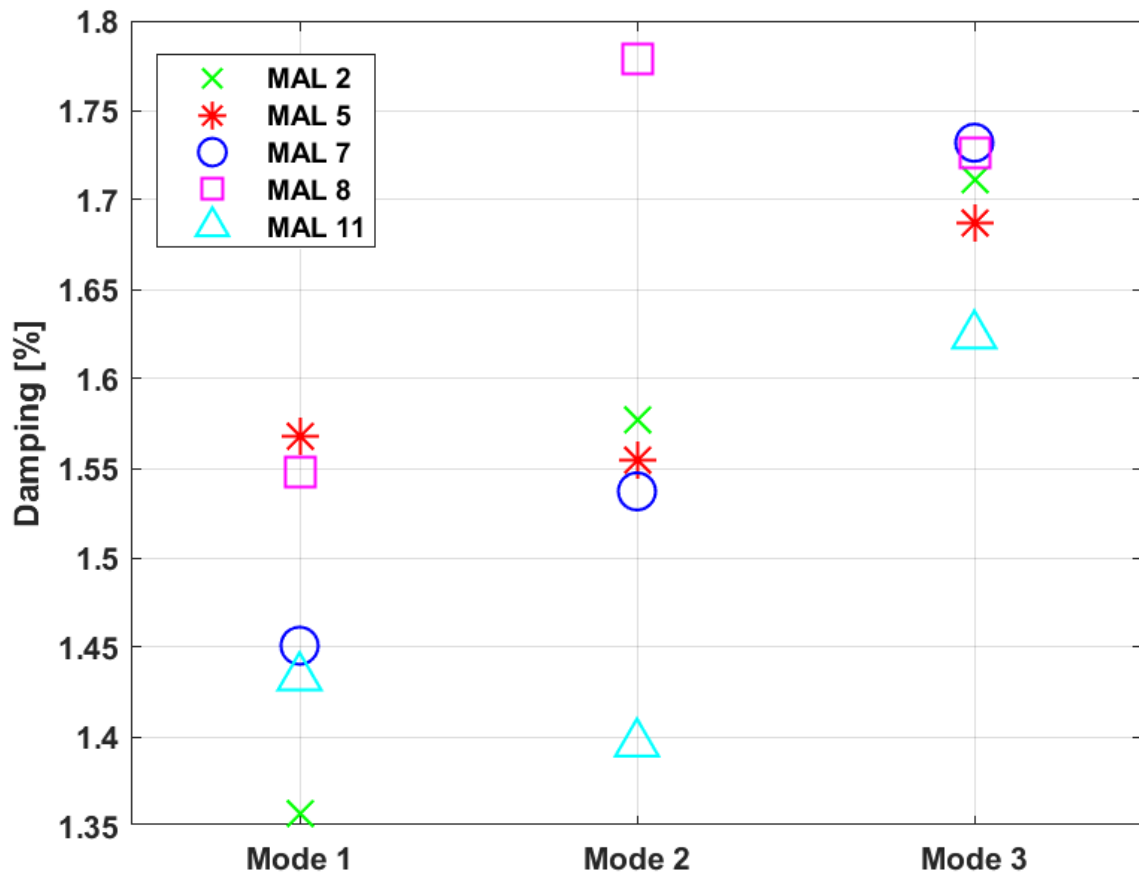
Figure 9.2: Comparison of the average damping values for every building

9.3 Mode shapes

There is consistency in the stabilisation plots for the first three modes of all buildings from the measurements performed in the vertical direction. The first mode is translational in the weak direction (Z), the second mode is translational in the strong direction (Y), and the third mode is torsional. The mode shapes obtained from the in-plane measurements also support this. The MAC assessment between the theoretical and measured mode shapes in table 8.4 suggests that both the first and second modes have linear behaviour, which indicates them being shear dominated. However, the MAC assessment with the theoretical parabolic mode shape also yields high values, causing uncertainty regarding which shape the building takes.

In an attempt to further investigate this, the parabolic equation (8.2) was solved using the normalized displacement of the first mode in MAL2 (table 7.3) as boundary conditions, which yielded the following constants a, b, and c:

$$a = -0.001769 \qquad b = 0.1553 \qquad c = -0.2545$$

The constant a decides the parabolic contribution to the equation, while constant b decides the linear contribution to the equation. Comparing the two constants for the range $x = [0, 9]$ with equation (9.1), the maximum contribution from the parabolic part is only 10% of the contribution from the linear part for $x = 9$, which points to the mode shapes being shear dominated with a slight bending portion.

$$\frac{a \cdot x^2}{b \cdot x} = \frac{a \cdot x}{b} = \frac{-0.001769 \cdot 9}{0.1553} = 0.1025 \tag{9.1}$$

Another observation made from the MAC assessment between theoretical and measured mode shapes is that the boundary conditions in equation (8.3) seem to fit the measured mode shapes well for the linear equation. The MAC values increase compared to the original linear mode shape depicted in figure 8.6a). For the parabolic mode shape, it is the other way around. It is not easy to decide which method is most fitting. Finding the exact mode shape the buildings take and how the concrete floor affects this should be looked at in further works.

An interesting note about the stabilisation plots is that all three modes are displayed in the plots for Y-direction for all buildings. In the Z-direction, only the first and third modes are displayed. The same pattern is also evident in the PSD plots, where three peaks arise in the Y-direction, implying that the first mode has significant oscillations in the Y-direction. The in-plane mode shapes in figure 7.5a) also support this, where a slight displacement in Y-direction is evident.

Table 9.1 presents the MAC values when comparing the mode shapes between MAL2 and the four other buildings. The high values indicate that the buildings experience similar mode shapes, which was the expected result, and that there has been consistency in the measurements and the processing of data.

Table 9.1: MAC values from the comparison of MAL2 with the other buildings

Mode	MAL2			
	MAL5	MAL7	MAL8	MAL11
1	1.0000	0.9997	0.9998	1.0000
2	0.9996	0.9998	0.9991	0.9998
3_y	0.9998	0.9986	0.9985	0.9986
3_z	0.9998	0.9997	0.9989	0.9893

9.4 Peak accelerations

The ISO-standard ISO10137 [1] contains recommendations for the serviceability of buildings against vibrations. In this standard, a recommendation for peak accelerations caused by wind-induced vibrations for a one-year return period can be found in Annex D. Figure 9.3 displays the maximum measured acceleration and the three maximum accelerations calculated from procedures in NS-EN 1991-1-4 plotted against the recommendations in ISO10137. The maximum measured acceleration stem from the recording *2022-02-28-18-00-00Z* at MAL5 (table B.5), which was measured to be 0.0103 m/s^2. The maximum calculated accelerations came out at 0.019, 0.022, and 0.029 m/s^2 for procedure in Annex B, Annex C - linear, and Annex C - parabolic, respectively.

As figure 9.3 displays, all accelerations are well within the recommended limit of 0.04 m/s^2 for a building with a first natural frequency of 2 Hz. The procedure in Annex B yields the closest calculated acceleration to the measured maximum acceleration. However, it is still 75% higher than the measured acceleration. The main reason for this is likely the wind speed used in the calculations, which was calculated to be 19.49 m/s. The measurements were performed without an anemometer, meaning no accurate wind data at the site was recorded. However, the Norwegian Meteorological Institute has a weather station about 1.1 km east of Moholt Student Village, at Voll. On the day of measuring MAL5, 28th February 2022, the fastest gust of wind was measured at 14.1 m/s between 8 and 9 PM [51]. The acceleration time series of accelerometer A1 and A2 in figure 9.4, shows the largest peak between hour one and two of the recording, which coincides with fastest gust of wind recorded at Voll. Based on this, the wind around Moholt student village was likely around the same speed measured at the weather station, which would explain the overshoot of the calculations from NS-EN 1991-1-4.

With the measured wind at the weather station as the basic wind, $v_b = 14.1 m/s$, the results are closer to the measured acceleration; 0.0065, 0.0077 and 0.0099 m/s^2 for calculations in Annex B, Annex C - linear, and Annex C - parabolic, respectively. These results suggest that using the parabolic mode shape in the acceleration calculations in Annex C yields the most realistic result in this case.
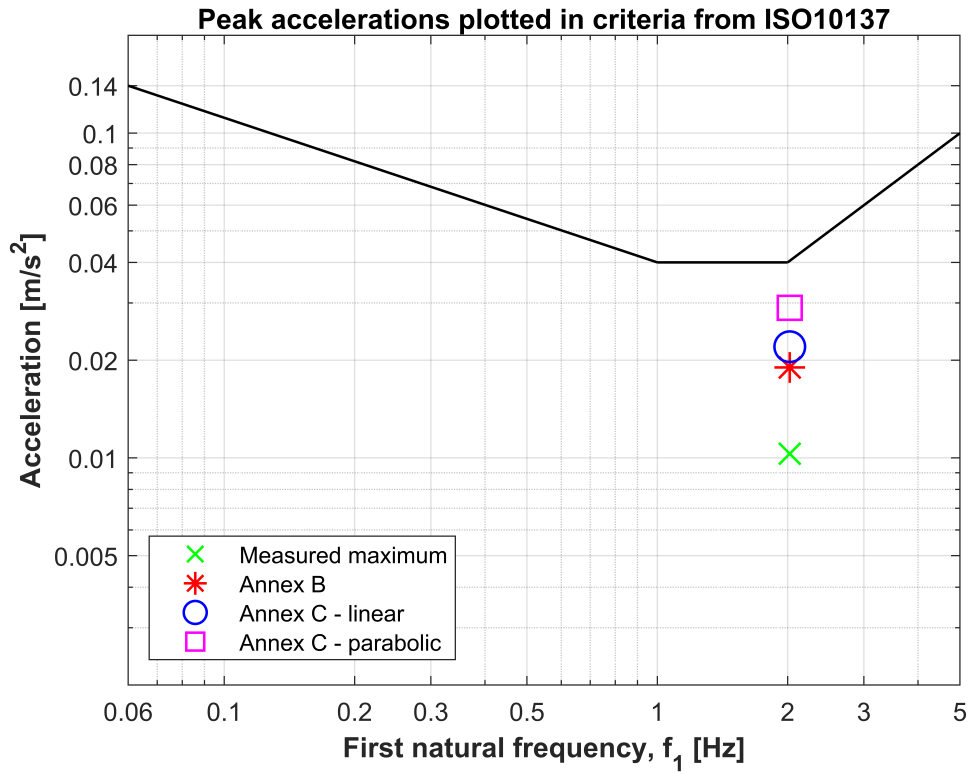
Figure 9.3: Comparison of the measured and theoretical peak accelerations with comfort criteria limit from ISO10137
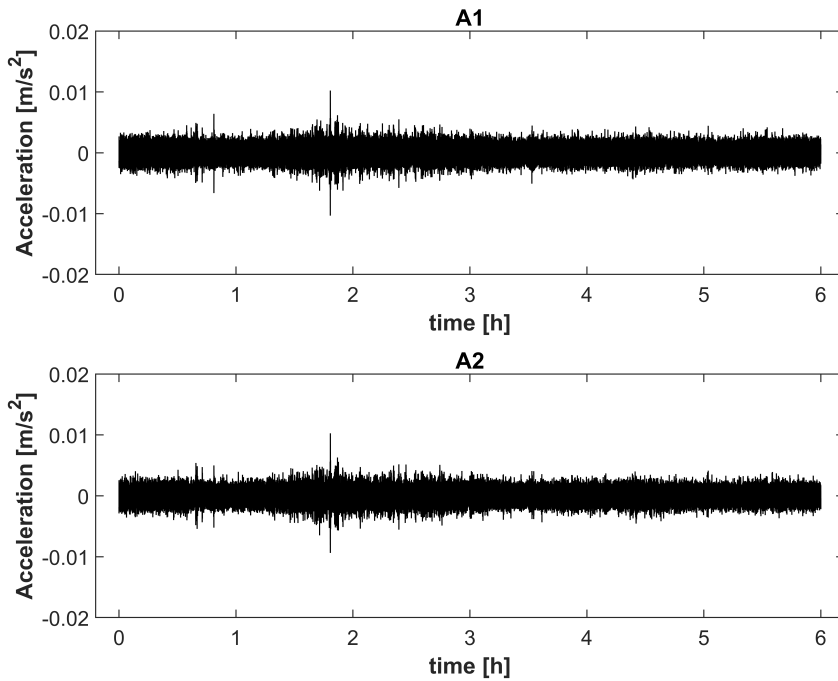
Figure 9.4: Acceleration time series for accelerometers A1 and A2 at MAL5, recording *2022-02-28-18-00-00Z*

9.5 Numerical model assessment

There are many elements of CLT modelling that are complicated and create challenges. Especially when comparing with in situ research the connections, nonstructural mass, and material properties is difficult to replicate exactly. A limitation of the numerical model is the assumptions made to present a result. The assumptions are reasoned, but they still present uncertainty.

The method to create the model has been to create the geometry per plan view and model the structural elements based on earlier research. Then look at the results, and see how they compare to the experimental data. Then try a different method in one of the variables, e.g. change the connections from hinged to fixed, change nonstructural mass, or use other material properties, while always trying to understand what the changes represent and how the results are affected. Because the goal is to design the model correctly according to what it is and not manipulate the results to get the wanted answer. After numerous model updates, research in earlier work, and actively advising the supervisors, the resulting model is the one that replicates the actual building the best of the tested solutions. However, there is still room for improvements, as the model do not compare perfectly with the experimental data.

While iterating the model, the results showed that it was the MAC values that was sensitive to changes. The natural frequencies did not deviate much from the experimental data with the different solutions. A speculative reason for these results could be the unusual y-shape in the building. The authors wonder if a traditional square-shaped building would differ less in MAC values with the same changes. It would be interesting to see a comparison of two buildings with the same structural system and similar size, but with a different shape, and do the same iterations in the model done in this thesis.

The second mode shape did not compare well with the experimental data. The numerical model showed a mode shape that had more torsional effect than in the experimental data. It was also for this mode shape that the MAC assessment did not reach a value above the rejection level. This is a weakness for the numerical model.

Different build-ups in the sections did not change the frequencies much, but they changed the interval between them. There are different engineering constants used for homogeneous sections compared to composite sections. This will make a difference between the solutions, but it is unclear how to replicate the same material properties with the different section types. This thesis does not research why and how to know which solution is better for different buildings and elements, but both methods are tested to see the different results.

Earlier research for numerical models of CLT buildings has used different techniques to model the CLT floor. It can be modelled stiff as a typical CLT element, combining the material properties in one mixed-material, or by adding a concrete layer to the composite sections. The interaction between the CLT and concrete in the actual

buildings is, for now, unclear. Therefore the methods were modelled, and the results were compared with the experimental data.

9.5.1 Study in different mass and connections

As the nonstructural mass and the connections are uncertainties, an overview of the possible solutions is created. The calculated nonstructural mass is 35t, and table 9.2 shows how a change affect the natural frequency. It is clearly the nonstructural mass that have the largest affect on the natural frequency. The connections do affect them, but not by more than $\approx 1\%$. The connections can still affect the mode shapes, and can not be neglected just by looking at the indifferent natural frequencies.

Table 9.2: Natural frequencies from Abaqus in Hz

Mass	Hinged			Fixed		
	f_1	f_2	f_3	f_1	f_2	f_3
0t	2.2853	2.4501	2.8022	2.3127	2.4721	2.8224
20t	2.1089	2.26121	2.5915	2.1340	2.2822	2.6098
35t	2.0005	2.1464	2.4614	2.0242	2.1654	2.4785
50t	1.9072	2.0468	2.3491	1.9297	2.0648	2.3652

9.5.2 MAC values compared

When comparing the displacement vectors from the numerical model and the experimental data, several solutions for the model have been used to see how the changes affects the mode shapes. As illustrated by table 9.3, the best match is a build-up consisting of: composite shell, regular CLT floors, 35t nonstructural mass, and material properties from Dahl's work [40]. The technique used for the comparisons is MAC (section 3.6). For the first mode it was homogeneous sections with the engineering constants from [52] with a stiff floor that provided the best MAC value. The material properties in Dahl's work [40] is for a general CLT plate, not specifically for Stora Enso. In Kurent et.al. [49] it is used values specifically for Stora Enso CLT elements. This provided worse results in MAC values than the general properties in the CLT.

Table 9.3: MAC-values compared

Section build-up	Connections	Material	Floor build-up	Mode 1	2	3
Composite	Hinged	Dahl	CLT	**0.8104**	**0.7868**	**0.8407**
			CLT w/concrete	0.7943	0.7302	0.6942
			Stiff	0.6804	0.6497	0.6838
		Kurent	CLT	0.8113	0.7515	0.7177
	Fixed	Dahl	CLT	0.8007	0.7789	0.8363
			CLT w/concrete	0.7930	0.7294	0.6952
			Stiff	0.6809	0.6499	0.6746
		Kurent	CLT	0.7930	0.7294	0.6952
Homogenous	Hinged	Gsell	CLT	**0.9280**	0.7813	0.5569
	Fixed	Gsell	CLT	0.9271	0.7847	0.5698

9.5.3 MAC values for 7th and 9th storey

The MAC values obtained for the first and second mode in the 7th and 9th storey are well under the rejection level. The value for the third mode is above the rejection level. This is probably due to a model that does not replicate the building well enough, but it is hard to pin-point why.

9.6 Measurement assessment

The equipment used for measuring the five buildings in Moholt 50|50 has been used by NTNU in different situations before and therefore did not need any preparations to get quality measurements. It was also helpful to have this project close to NTNU, which permitted frequent visits and the possibility to resume other forms of progress if it was a hindrance at the site. Hence, no obstacles have limited the data collected, and the quality is assumed valid.

The experimental data is chiefly collected in the stairwell, where the torsional movement is limited. If possible, a preferred solution is to simultaneously collect data for the horizontal and vertical mode shapes. That procedure would nullify the need for two types of installations, save time, and have more data on the horizontal mode shapes than what has been executed. It would require a permission to circumvent the HSE rules at Moholt 50|50.

9.7 Assessment of Operational Modal Analysis

Time has been invested in understanding the earlier MATLAB scripts to create the new scripts for the buildings at Moholt 50|50. It could still be that there are mistakes or errors in the scripts or how they are used. During the analysis, the results have been discussed with the supervisor, and most errors should be fixed. However, there is still the possibility of a small error, which could be a source of error.

Chapter 10

Conclusion

This thesis' main objective is assessing the dynamic properties of five identical CLT multi-storey buildings in operational conditions through in situ measurements and appropriate processing of the data. The dynamic properties obtained from every building is assessed and compared to each other. Natural frequencies and mode shapes have been compared with a numerical model, and peak accelerations has been compared to numerical calculations in the Eurocode [2] and the criteria in ISO 10137 [1].

The first three mode shapes of all five buildings are identified by DD-SSI. The corresponding frequencies are also confirmed by the PSD, showing similar results. The processed data displays the same three mode shapes for all the buildings: mode one as the first order translational mode in Z-direction, mode two as the first order translational mode in Y-direction, and mode three as the first order torsional mode. There are indications of detecting higher order modes in the data. Unfortunately, there is little consistency for these modes and they are therefore deemed inconclusive.

The dynamic properties of the buildings coincide nicely with each other. Both natural frequencies and mode shapes are in close proximity of each other. The damping ratios shows a little more inconsistency, where the values follow no detectable pattern. However, the range of which all the damping ratios lie, are coincident with damping ratios found in other similar buildings.

Through trial and error, a numerical model that adequately represents the building is presented. In the numerical model, a series of different approaches explained how the different parameters affect the modal properties. Different adaptations made different changes: build-ups in the sections, different techniques to model the floor, connections, and nonstructural mass. The nonstructural mass is estimated to replicate the realistic nonstructural mass. The result that, in this case, best represented the buildings is using composite shells in the sections, composite shells in the floor with screed and plasterboard added as nonstructural mass, material properties from Dahl's work [40], and hinged connections.

Peak accelerations measured in the buildings are well below the recommended criteria in ISO 10137[1], presumably because there was not a large enough ambient loading to extract a proper peak acceleration in the buildings. The calculations in Annex C with a parabolic mode shape gives the closest result to the measured peak acceleration when adjusting the wind to that measured at the weather station.

10.1 Further work

It will continue to be important to research tall timber buildings, and hopefully it will be normal to see new and higher buildings in timber in the future. With the work done in this thesis it is possible to continue this project and obtain an higher level of knowledge, and there is already data available. Hopefully, this thesis will better the understanding of CLT buildings, and improve the understanding of taller timber buildings in general.

10.1.1 Numerical model updating

The numerical model is designed as detailed and extensively with time and knowledge present, but it is still not a finished product. There are actions to improve the model by updating it. Following the work e.g. Kurent et.al. [49] there are possibilities to update the model, e.g. changing material properties, shear wall stiffness reduction due to the wall-floor joint, or implement sensitivity analysis. This can be especially useful because it is difficult to model the actual connection stiffness in CLT buildings, and the building can be represented better by an updated model. These actions can be implemented on the numerical model for the Moholt buildings to find a result that represents the experimental data better than the current numerical model do. It would also be naturally to get into more detail about nonstructural mass to get a even better numerical model.

10.1.2 Damping

The draft for the new NS-EN 1995-1-1 [26] do cover damping more extensively than the current [25], so it should be easier in the future to design CLT buildings. A important factor to consider when estimating the damping of a building is sylomers. The sylomers inside the building is affecting the damping and reduces the stiffness in the building [53]. In this thesis it has not been researched. It could be very relevant for the future to improve the understanding of damping in CLT buildings, and sylomers are an important factor.

As a starting point, if someone are going to try and continute this project it is made an illustration of the different sylomers in the building [54].

Figure 10.1: Illustration of sylomer location
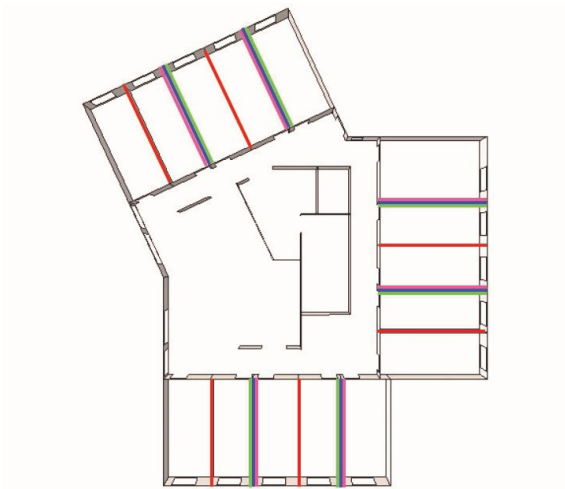
Table 10.1: Overview sylomer types

	Storeys	Types
Red	All	Getzner SR220
Violet	2 - 4	Getzner SR1200
Blue	5 - 8	Getzner SR850
Green	9	Getzner SR66

Bibliography

[1] *Bases for design of structures — Serviceability of buildings and walkways against vibrations. ISO 10137:2007*, Nov. 2007.

[2] *Eurokode 1: Laster på konstruksjoner Del 1-4: Allmenne laster Vindlaster. NS-EN 1991-1-4:2005+NA:2009*, Apr. 2005.

[3] K. A. Malo, 'Some structural design issues of the 14-storey timber framed building "Treet" in Norway', en, p. 18, 2016.

[4] M. F. Olsen and O. Hansen, 'Measuring Vibrations and assessing Dynamic Properties of tall Timber Buildings', Engelsk, M.S. thesis, NTNU, Trondheim, Jun. 2016.

[5] R. H. Lervik and S. Kristiansen, 'Assessing Wind Induced Dynamic Properties of Two Tall CLT Buildings in Tromsø', English, M.S. thesis, NTNU, Trondheim, Jun. 2021.

[6] S. Tulebekova *et al.*, 'Modeling stiffness of connections and non-structural elements for dynamic response of taller glulam timber frame buildings', *Engineering Structures*, vol. 261, p. 114 209, Jun. 2022. DOI: 10.1016/j.engstruct.2022.114209.

[7] *Moholt studentby*, nb. [Online]. Available: https://www.sit.no/hybel/moholt-studentby (visited on 8th Jun. 2022).

[8] SiT, *Moholt studentby*, nb. [Online]. Available: https://www.sit.no/hybel/moholt-studentby (visited on 1st Jun. 2022).

[9] K. H. Solli and G. Glasø, *FOKUS på tre: Trebaserte konstruksjonselementer*, Norsk, Jan. 2011. [Online]. Available: https://www.treteknisk.no/resources/filer/publikasjoner/fokus-pa-tre/Fokus-nr-27.pdf (visited on 27th Apr. 2022).

[10] R. Andrew, *Global CO2 emissions from cement production*, en, Version Number: 210723 Type: dataset, Jul. 2021. DOI: 10.5281/ZENODO.831454. (visited on 27th Apr. 2022).

[11] A. Himes and G. Busby, 'Wood buildings as a climate solution', en, *Developments in the Built Environment*, vol. 4, p. 100 030, Nov. 2020, ISSN: 26661659. DOI: 10.1016/j.dibe.2020.100030.

[12] J. Aarstad *et al.*, *FOKUS på tre: Masivtre*, Norsk, Jan. 2008. [Online]. Available: https://www.treteknisk.no/resources/filer/publikasjoner/fokus-pa-tre/Fokus-nr-20.pdf (visited on 28th Apr. 2022).

[13] *Massive treelementer. Typer og bruksområder. 520.205*, 2001. [Online]. Available: https://www.byggforsk.no/dokument/3009/massive_treelementer_typer_og_bruksomraader (visited on 28th Apr. 2022).

[14] D. R. Fell, 'Wood in the human environment : Restorative properties of wood in the built indoor environment', eng, Ph.D. dissertation, University of British Columbia, 2010. DOI: 10.14288/1.0071305.

[15] A. Gustafsson *et al.*, *The CLT Handbook*, English, 2019. [Online]. Available: https://www.swedishwood.com/siteassets/5-publikationer/pdfer/clt-handbook-2019-eng-m-svensk-standard-2019.pdf.

[16] J. Hindklev, *Advarer mot å bygge høyt med massivtre som hovedbærekonstruksjon*, no, Section: Bygg, Jan. 2020. [Online]. Available: https://www.bygg.no/article/1420345!/ (visited on 29th Apr. 2022).

[17] K. L. Friquin and D. Denstad, *Trygt å bruke massivtre i bærekonstruksjoner*, no. [Online]. Available: https://www.sintef.no/siste-nytt/2020/trygt-a-bruke-massivtre-i-barekonstruksjoner/ (visited on 29th Apr. 2022).

[18] J. Schmid and M. Fragiacomo, 'Editorial of the SI: Wood buildings and fire', en, *Fire Safety Journal*, vol. 107, p. 235, Jul. 2019, ISSN: 0379-7112. DOI: 10.1016/j.firesaf.2019.102884.

[19] G. Glasø, *FOKUS på tre: Tre og lyd*, 2011. [Online]. Available: https://www.treteknisk.no/publikasjoner/fokus-pa-tre/fokus-36--tre-og-lyd (visited on 10th May 2022).

[20] *Lydforhold i bygninger lydklasser for ulike bygningstyper. NS 8175:2019*, Norsk, Jul. 2021.

[21] S. Hveem and A. Homb, 'Lydoverføring i byggesystemer med massivtreelementer', SINTEF, Tech. Rep. 80, 2011. [Online]. Available: https://www.sintefbok.no/book/index/912/lydoverfoering_i_byggesystemer_med_massivtreelementer (visited on 11th May 2022).

[22] F. A. Johann *et al.*, 'Wind-induced motion on tall buildings: A comfort criteria overview', en, *Journal of Wind Engineering and Industrial Aerodynamics*, vol. 142, pp. 26–42, Jul. 2015, ISSN: 0167-6105. DOI: 10.1016/j.jweia.2015.03.001.

[23] E. Lazzarini *et al.*, 'Comfort assessment of high-rise timber buildings exposed to wind-induced vibrations', en, *The Structural Design of Tall and Special Buildings*, vol. 30, no. 12, e1882, 2021, ISSN: 1541-7808. DOI: 10.1002/tal.1882.

[24] I. Edskär and H. Lidelöw, 'Dynamic properties of cross-laminated timber and timber truss building systems', en, *Engineering Structures*, vol. 186, pp. 525–535, May 2019, ISSN: 0141-0296. DOI: 10.1016/j.engstruct.2019.01.136.

[25] *Eurokode 5: Prosjektering av trekonstruksjoner Del 1-1: Allmenne regler og regler for bygninger. NS-EN 1995-1-1:2004+A1:2008+NA:2010*, Oct. 2010.

[26] *Consolidated draft pr EN 1995-1-1*, Oct. 2021.

[27] S. MacDonald, *OMG! What is OMA? Operational Modal Analysis*, Jul. 2022. [Online]. Available: https://community.sw.siemens.com/s/article/OMG-What-is-OMA-Operating-Modal-Analysis (visited on 11th May 2022).

[28] C. Rainieri and G. Fabbrocino, *Operational Modal Analysis of Civil Engineering Structures: An Introduction and Guide for Applications*, eng, 2014th ed. New York, NY: Springer New York, ISBN: 978-1-4939-0766-3. DOI: 10.1007/978-1-4939-0767-0.

[29] P. V. Overschee and B. d. Moor, *Subspace Identification for Linear Systems — SpringerLink*. 1996. [Online]. Available: https://link.springer.com/book/10.1007/978-1-4613-0465-4 (visited on 11th May 2022).

[30] F. Ivarsson and J. Sjöholm, 'Dynamic Response in Tall Timber Structures', eng, 2018, Accepted: 2019-07-03T14:51:49Z. [Online]. Available: https://odr.chalmers.se/handle/20.500.12380/255792 (visited on 8th Jun. 2022).

[31] G. Lallement and D. Inman, 'A Tutorial on Complex Eigenvalues', Jan. 1995. [Online]. Available: https://www.researchgate.net/publication/253118549_A_Tutorial_on_Complex_Eigenvalues.

[32] Felix Govaers, *Introduction and Implementations of the Kalman Filter*, eng. IntechOpen, 2019, ISBN: 978-1-83880-536-4. DOI: 10.5772/intechopen.75731.

[33] S. Greś *et al.*, 'Uncertainty quantification for the Modal Phase Collinearity of complex mode shapes', en, *Mechanical Systems and Signal Processing*, vol. 152, p. 107 436, May 2021, ISSN: 0888-3270. DOI: 10.1016/j.ymssp.2020.107436.

[34] *Understanding FFTs and Windowing*, en. [Online]. Available: https://www.ni.com/en-no/innovations/white-papers/06/understanding-ffts-and-windowing.html (visited on 9th Jun. 2022).

[35] *NI-9234 Specifications - NI*. [Online]. Available: https://www.ni.com/docs/en-US/bundle/ni-9234-specs/page/specs.html# (visited on 10th Jun. 2022).

[36] *Resample uniform or nonuniform data to new fixed rate - MATLAB resample - MathWorks Nordic*. [Online]. Available: https://se.mathworks.com/help/signal/ref/resample.html (visited on 10th Jun. 2022).

[37] Simulia, *Abaqus Analysis User's Guide*, 2014. [Online]. Available: http://130.149.89.49:2080/v6.14/books/usb/default.htm (visited on 3rd May 2022).

[38] *CLT by Stora Enso - Technical brochure*, Oct. 2017.

[39] *Konstruksjonstrevirke Fasthetsklasser. EN 338: 2009*, 2009.

[40] B. Dahl, *Mechanical properties of clear wood from Norway spruce*, eng. Norges teknisk-naturvitenskapelige universitet, Fakultet for ingeniørvitenskap og teknologi, Institutt for konstruksjonsteknikk, 2009, Accepted: 2014-12-19T11:58:06Z, ISBN: 978-82-471-1912-9. [Online]. Available: https://ntnuopen.ntnu.no/ntnu-xmlui/handle/11250/236422 (visited on 23rd May 2022).

[41] J. Wetterholt, 'Modelling cross-laminated timber floors in dynamic analysis - Eigenfrequency prediction', en, *undefined*, 2019. [Online]. Available: https://www.semanticscholar.org/paper/Modelling-cross-laminated-timber-floors-in-dynamic-Wetterholt/4e87ff595ee9fa655a38f11c52afb4b18c87c797 (visited on 1st Jun. 2022).

[42] Mengyinan, 'Capability Analysis of Abaqus Shell Element Based on Finite Element Method', *Journal of Physics: Conference Series*, vol. 1345, p. 022 034, Nov. 2019. DOI: 10.1088/1742-6596/1345/2/022034.

[43] *ABAQUS Analysis User's Manual (v6.6)*. [Online]. Available: https://classes. engineering.wustl.edu/2009/spring/mase5513/abaqus/docs/v6.6/books/usb/ default.htm?startat=pt06ch23s06alm15.html (visited on 10th Jun. 2022).

[44] Simulia, *Selecting beam elements*, en, concept. [Online]. Available: https :// abaqus-docs.mit.edu/2017/English/SIMACAEGSARefMap/simagsa-c-bmssltbeamelm. htm (visited on 1st Jun. 2022).

[45] *Inventarlister for Moholt studentby*, nb. [Online]. Available: https://www.sit. no/hybel/inventarlister-moholt-studentby (visited on 7th May 2022).

[46] I. Gavric *et al.*, 'Cyclic Behavior of CLT Wall Systems: Experimental Tests and Analytical Prediction Models', EN, *Journal of Structural Engineering*, vol. 141, no. 11, p. 04 015 034, Nov. 2015, Publisher: American Society of Civil Engineers, ISSN: 1943-541X. DOI: 10.1061/(ASCE)ST.1943-541X.0001246.

[47] A. Aloisio *et al.*, 'Dynamic identification and model updating of an eight-storey CLT building', en, *Engineering Structures*, vol. 213, p. 110 593, Jun. 2020, ISSN: 0141-0296. DOI: 10.1016/j.engstruct.2020.110593.

[48] T. Reynolds *et al.*, 'Ambient vibration tests of a cross-laminated timber building', *Proceedings of the ICE - Construction Materials*, vol. 168, pp. 1–11, Jun. 2015. DOI: 10.1680/coma.14.00047.

[49] B. Kurent *et al.*, 'Model updating of seven-storey cross-laminated timber building designed on frequency-response-functions-based modal testing', *Structure and Infrastructure Engineering*, vol. 0, no. 0, pp. 1–19, Jun. 2021, Publisher: Taylor & Francis _eprint: https://doi.org/10.1080/15732479.2021.1931893, ISSN: 1573-2479. DOI: 10.1080/15732479.2021.1931893.

[50] M. Follesa *et al.*, 'Seismic design of multi-storey cross laminated timber buildings according to Eurocode 8', *Ingegneria Sismica*, vol. 30, pp. 27–53, Dec. 2013.

[51] *Historiske værdata for Trondheim Voll som graf - 28. februar 2022*, nb-no. [Online]. Available: https://www.yr.no/nb/historikk/graf/5-68860/Norge/Tr% C3%B8ndelag/Trondheim/Trondheim%20%E2%88%92%20Voll?q=2022-02-28 (visited on 10th Jun. 2022).

[52] D. Gsell *et al.*, 'Cross-Laminated Timber Plates: Evaluation and Verification of Homogenized Elastic Properties', EN, *Journal of Structural Engineering*, vol. 133, no. 1, pp. 132–138, Jan. 2007, Publisher: American Society of Civil Engineers, ISSN: 0733-9445. DOI: 10.1061/(ASCE)0733-9445(2007)133:1(132).

[53] Å. Bolmsvik, 'Damping assessment of light wooden assembly with and without damping material', *Engineering structures*, vol. 49, pp. 434–447, Apr. 2013, ISSN: 0141-0296.

[54] *Getzner sylomer*. [Online]. Available: https://www.getzner.com/en/products/ sylomer.

Appendices

Appendix A

Layout of accelerometers

Vertical layout

Table A.1 lists different information about the accelerometer for the measurementsin vertical direction. The Mod and Channel is where the accelerometers are connected to the cRIO controller. It is also possible to see the relation between local and global direction.

Table A.1: Vertical accelerometer data

Accelerometer	Floor	Mod	Channel	Local direction	Global direction (X,Y,Z)
A1	9	2	00	x'	(1,0,0)
A1	9	2	01	y'	(0,1,0)
A1	9	2	02	z'	(0,0,1)
A2	9	3	00	x'	(1,0,0)
A2	9	3	01	y'	(0,1,0)
A2	9	3	02	z'	(0,0,1)
A3	6	4	00	x'	(1,0,0)
A3	6	4	01	y'	(0,1,0)
A3	6	4	02	z'	(0,0,1)
A4	3	5	00	x'	(1,0,0)
A4	3	5	01	y'	(0,1,0)
A4	3	5	02	z'	(0,0,1)

In-plane layout 9th floor

Similarly for the in-plane layout in the 9th storey.

Table A.2: In-plane accelerometer data in the 9th storey

Accelerometer	Floor	Mod	Channel	Local direction	Global direction (X,Y,Z)
A1	9	2	00	x'	$(1,0,0)$
A1	9	2	01	y'	$(0,-1 \cdot \sin(25°),-1 \cdot \cos(25°))$
A1	9	2	02	z'	$(0,-1 \cdot \cos(25°),-1 \cdot \sin(25°))$
A2	9	3	00	x'	$(1,0,0)$
A2	9	3	01	y'	$(0,1,0)$
A2	9	3	02	z'	$(0,0,1)$
A3	9	4	00	x'	$(1,0,0)$
A3	9	4	01	y'	$(0,0,1)$
A3	9	4	02	z'	$(0,-1,0)$
A4	9	5	00	x'	$(1,0,0)$
A4	9	5	01	y'	$(0,0,1)$
A4	9	5	02	z'	$(0,-1,0)$

In-plane layout 7th and 9th floor

Similarly for the in-plane layout in the 7th and 9th storey.

Table A.3: In-plane accelerometer data in the 7th and 9th storey

Accelerometer	Floor	Mod	Channel	Local direction	Global direction (X,Y,Z)
A1	9	2	00	x'	$(1,0,0)$
A1	9	2	01	y'	$(0,-1 \cdot \sin(25°),-1 \cdot \cos(25°))$
A1	9	2	02	z'	$(0,-1 \cdot \sin(25°),-1 \cdot \cos(25°))$
A2	7	3	00	x'	$(1,0,0)$
A2	7	3	01	y'	$(0,-1 \cdot \sin(25°),-1 \cdot \cos(25°))$
A2	7	3	02	z'	$(0,-1 \cdot \sin(25°),-1 \cdot \cos(25°))$
A3	7	4	00	x'	$(1,0,0)$
A3	7	4	01	y'	$(0,1,0)$
A3	7	4	02	z'	$(0,0,1)$
A4	7	5	00	x'	$(1,0,0)$
A4	7	5	01	y'	$(0,0,1)$
A4	7	5	02	z'	$(0,-1,0)$

Appendix B

Moholt Allmenning 5

The following four appendices contains the results obtained from the measurements at building MAL5, MAL7, MAL8, and MAL11, in that order. A short description of these appendices' build up will follow. Firstly, the files used for the results are stated. One of these are in bold letters. This file is used for the figures "Stabilisation diagrams" and "Power spectral densities", and to find the mode shape vectors. All files stated are used to find natural frequencies and damping values. For peak accelerations the file with the single highest acceleration is used. Secondly, if necessary, a special note about the appendix is presented. Lastly, the results from the building is presented. They appear in the following order:

1. Stabilisation diagrams

2. Power spectral densities

3. Natural frequencies

4. Damping values

5. Mode shape vectors and MAC assessment compared to the other buildings

6. Peak accelerations

This appendix presents the results at MAL5. The files used for these results are:
- 2022-02-28-12-00-00Z
- **2022-02-28-18-00-00Z**
- 2022-03-01-00-00-00Z

Stabilisation diagrams
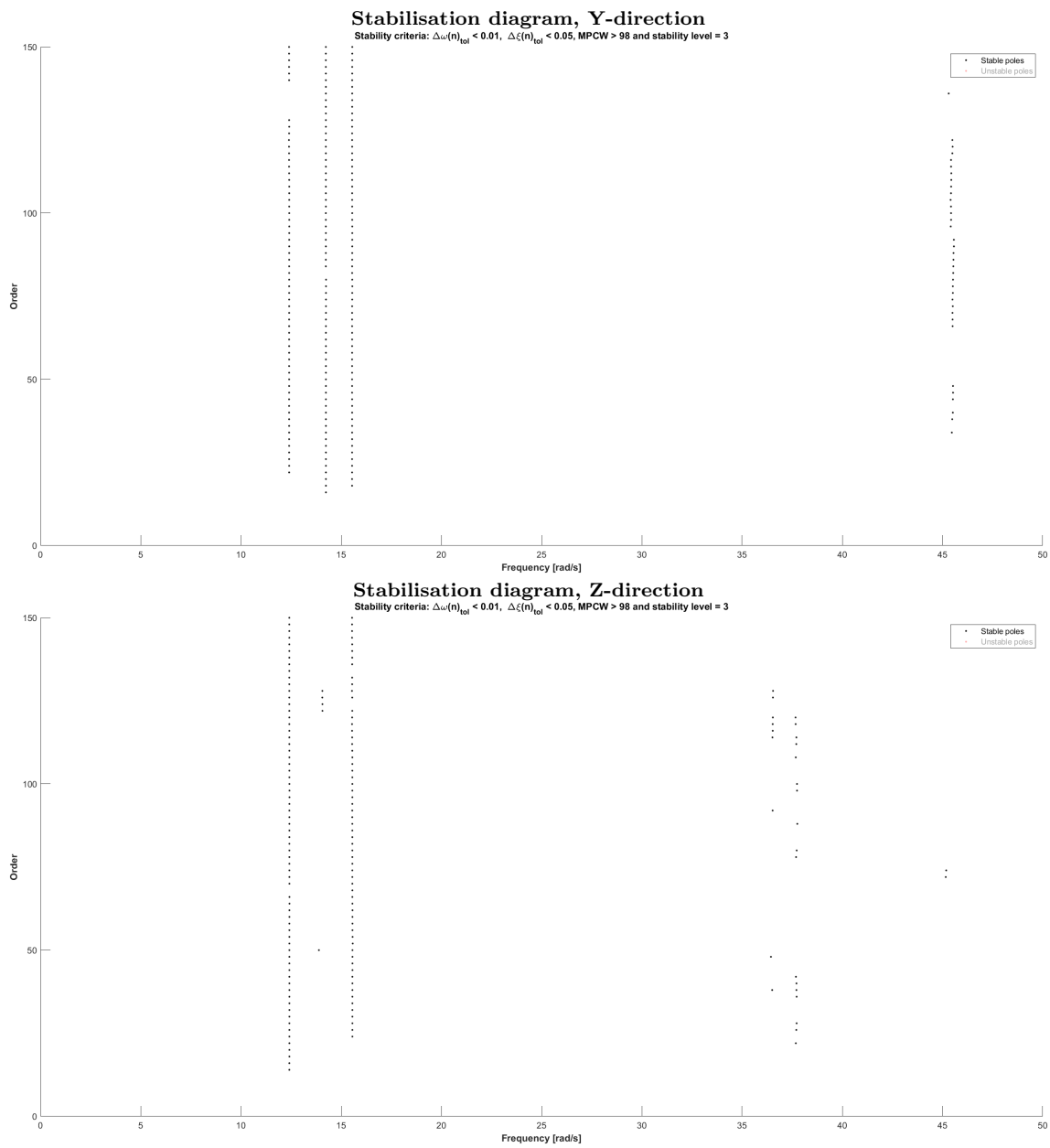
Figure B.1: Stabilisation diagrams from 6hr recording, 2022-02-28-18-00-00Z

Power spectral densities

Figure B.2: Plots of PSD from accelerometer A1, 6hr recording, 2022-02-28-18-00-00Z

Natural frequencies

Table B.1: Natural frequencies at MAL5, including standard deviation and number of stable poles

Mode	$f_n[Hz]$	$\sigma_{f_n}[Hz]$	SP	$f_{n,PSD}[Hz]$
1	1.978	0.0010	372	1.973
2	2.265	0.0005	189	2.268
3	2.472	0.0010	354	2.459

Damping

Table B.2: Damping values for MAL5, including standard deviation and number of stable poles

Mode	$\xi_n[\%]$	$\sigma_{\xi_n}[\%]$	SP
1	1.568	0.0260	372
2	1.554	0.0227	189
3	1.687	0.0460	354

Mode shapes

Table B.3: Normalised mode shape vectors from MAL5

Accelerometer	Mode 1	Mode 2	Mode 3	Mode 3
A1	-1.0000	-1.0000	-1.0000	-1.0000
A3	-0.6318	-0.5700	-0.6774	-0.6917
A4	-0.2022	-0.1737	-0.2238	-0.3086
Direction	Z	Y	Y	Z
Order	60	60	60	60

Table B.4: MAC values from the comparison of MAL5 with the other buildings

Mode	MAL5			
	MAL2	MAL7	MAL8	MAL11
1	1.0000	0.9999	0.9998	1.0000
2	0.9996	0.9989	0.9997	0.9994
3_y	0.9998	0.9994	0.9994	0.9992
3_z	0.9998	0.9991	0.9995	0.9859

(a) Mode 1   (b) Mode 2

(c) Mode 3, Z-direction   (d) Mode 3, Y-direction
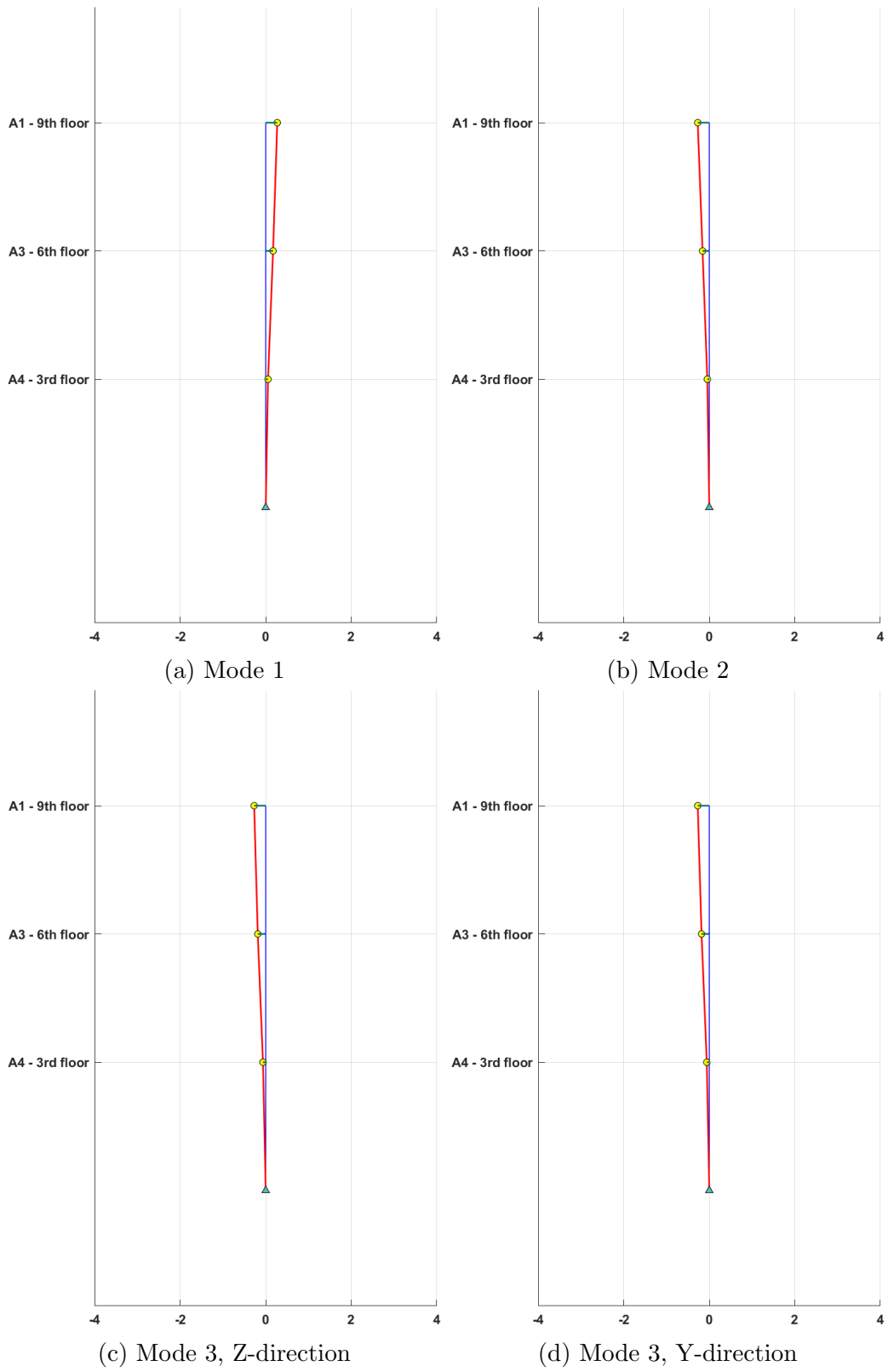
Figure B.3: Illustration of vertical mode shapes at MAL5

(a) Mode 1

(b) Mode 2

(c) Mode 3, Z-direction

(d) Mode 3, Y-direction

Figure B.4: Plots of the mode shapes in the complex plane

Peak acceleration

Table B.5: Peak accelerations at MAL5 from 6hr recording 2022-02-28-18-00-00Z

Accelerometer	Y-direction$[m/s^2]$	Z-direction$[m/s^2]$
A1	0.0103	0.0098
A2	0.0103	0.0093
A3	0.0063	0.0068
A4	0.0037	0.0038

Appendix C

Moholt Allmenning 7

This appendix presents the results at MAL7. The files used for these results are: - 2022-03-02-12-00-00Z
- **2022-03-02-18-00-00Z**
- 2022-03-03-00-00-00Z

Stabilisation diagrams
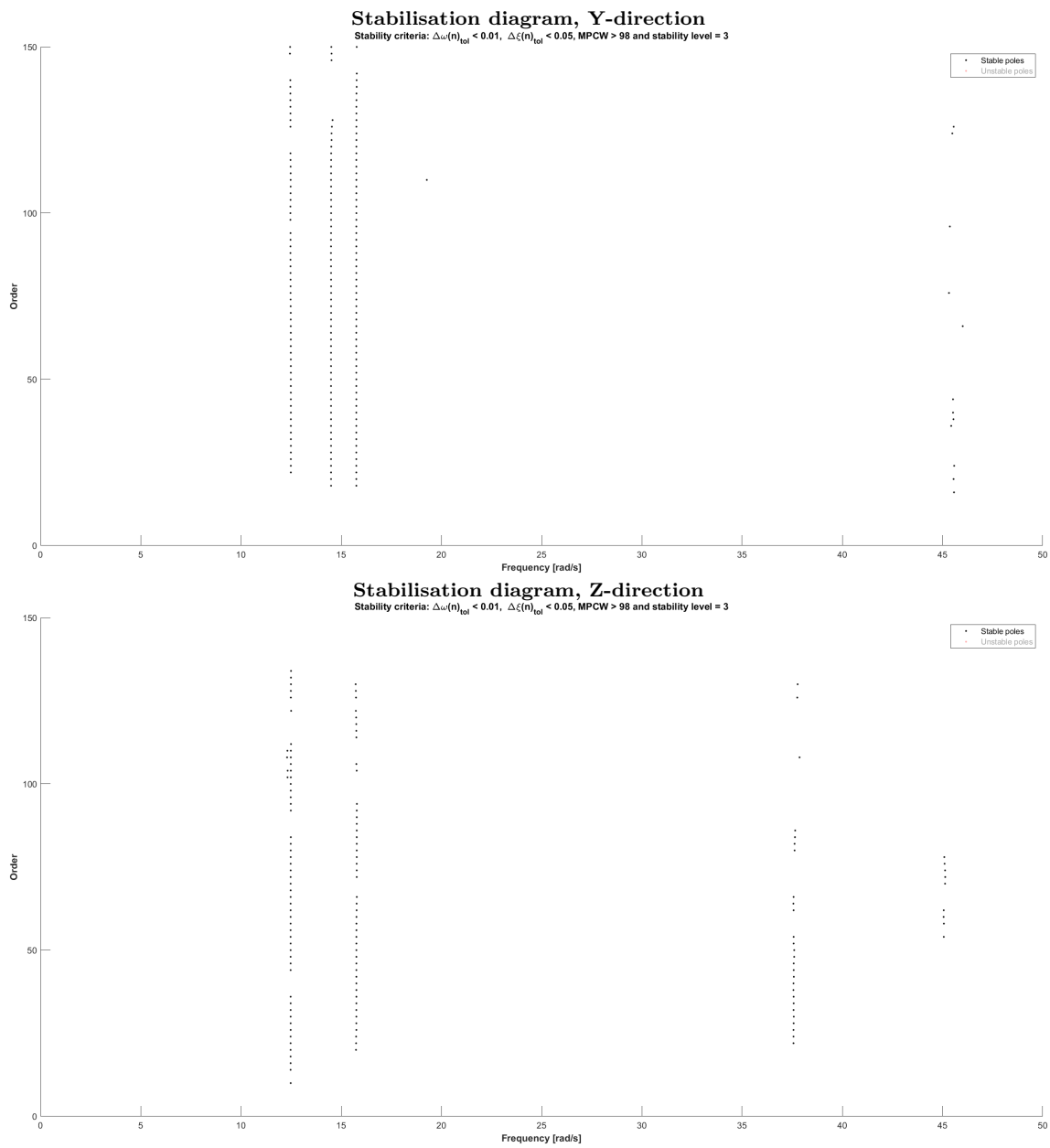
Figure C.1: Stabilisation diagrams from 6hr recording, 2022-03-02-18-00-00Z
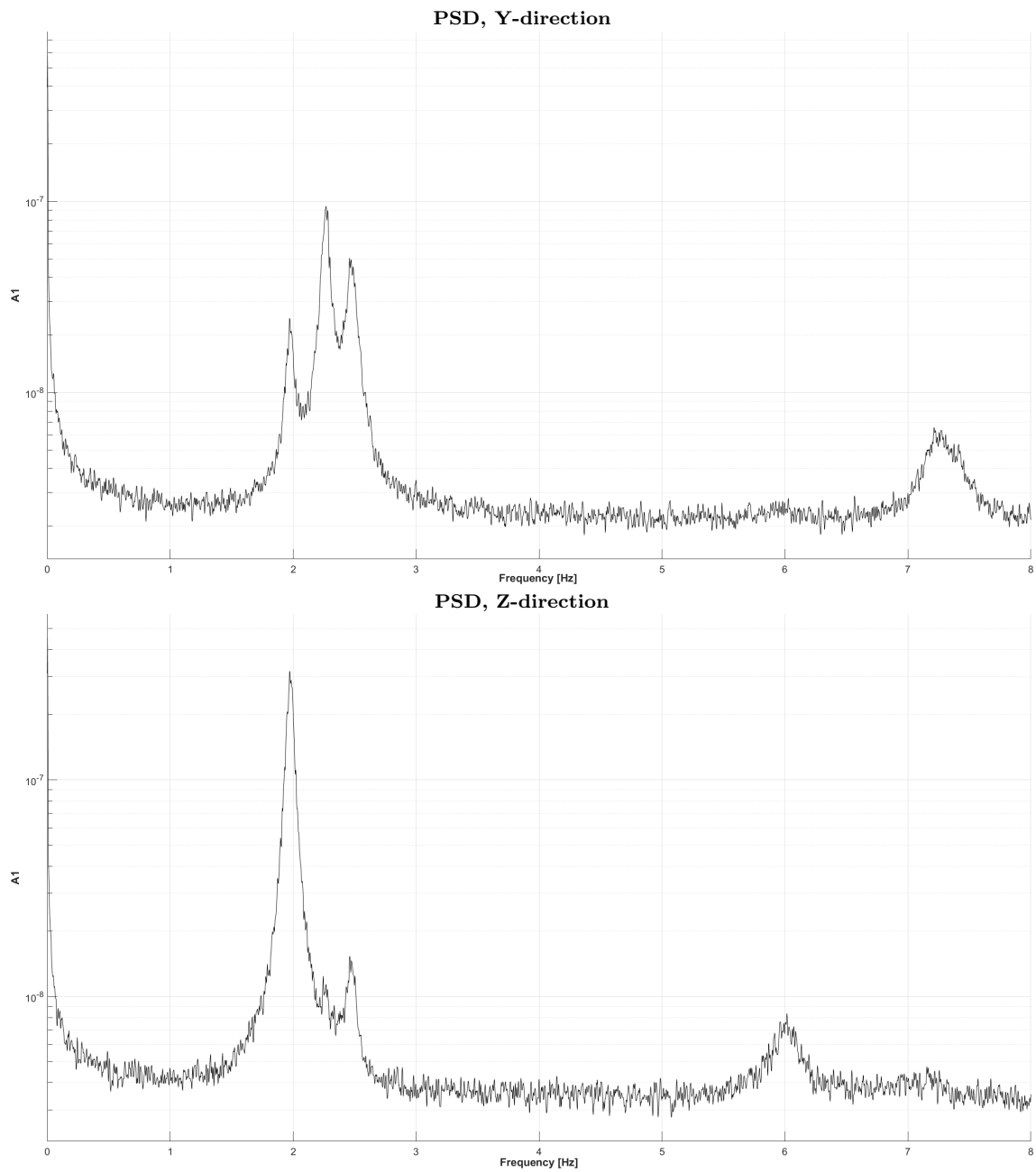
Power spectral densities

Figure C.2: Plots of PSD from accelerometer A1, 6hr recording, 2022-03-02-18-00-00Z

Natural frequencies

Table C.1: Natural frequencies at MAL7, including standard deviation and number of stable poles

Mode	$f_n[Hz]$	$\sigma_{f_n}[Hz]$	SP	$f_{n,PSD}[Hz]$
1	1.985	0.0011	303	1.982
2	2.305	0.0013	176	2.307
3	2.504	0.0015	326	2.500

Damping

Table C.2: Damping values for MAL7, including standard deviation and number of stable poles

Mode	$\xi_n[\%]$	$\sigma_{\xi_n}[\%]$	SP
1	1.451	0.0459	303
2	1.537	0.0237	176
3	1.732	0.0513	326

Mode shapes

Table C.3: Normalised mode shape vectors from MAL7

Accelerometer	Mode 1	Mode 2	Mode 3	Mode 3
A1	-1.0000	1.0000	-1.0000	1.0000
A3	-0.6435	0.6117	-0.6435	0.6613
A4	-0.2126	0.1633	-0.2126	0.2769
Direction	Z	Y	Y	Z
Order	60	60	60	60

Table C.4: MAC values from the comparison of MAL7 with the other buildings

Mode	MAL7 MAL2	MAL5	MAL8	MAL11
1	0.9997	0.9999	0.9993	0.9997
2	0.9998	0.9989	0.9983	0.9995
3_y	0.9986	0.9994	1.0000	0.9991
3_z	0.9997	0.9991	0.9986	0.9908

(a) Mode 1   (b) Mode 2

(c) Mode 3, Z-direction   (d) Mode 3, Y-direction
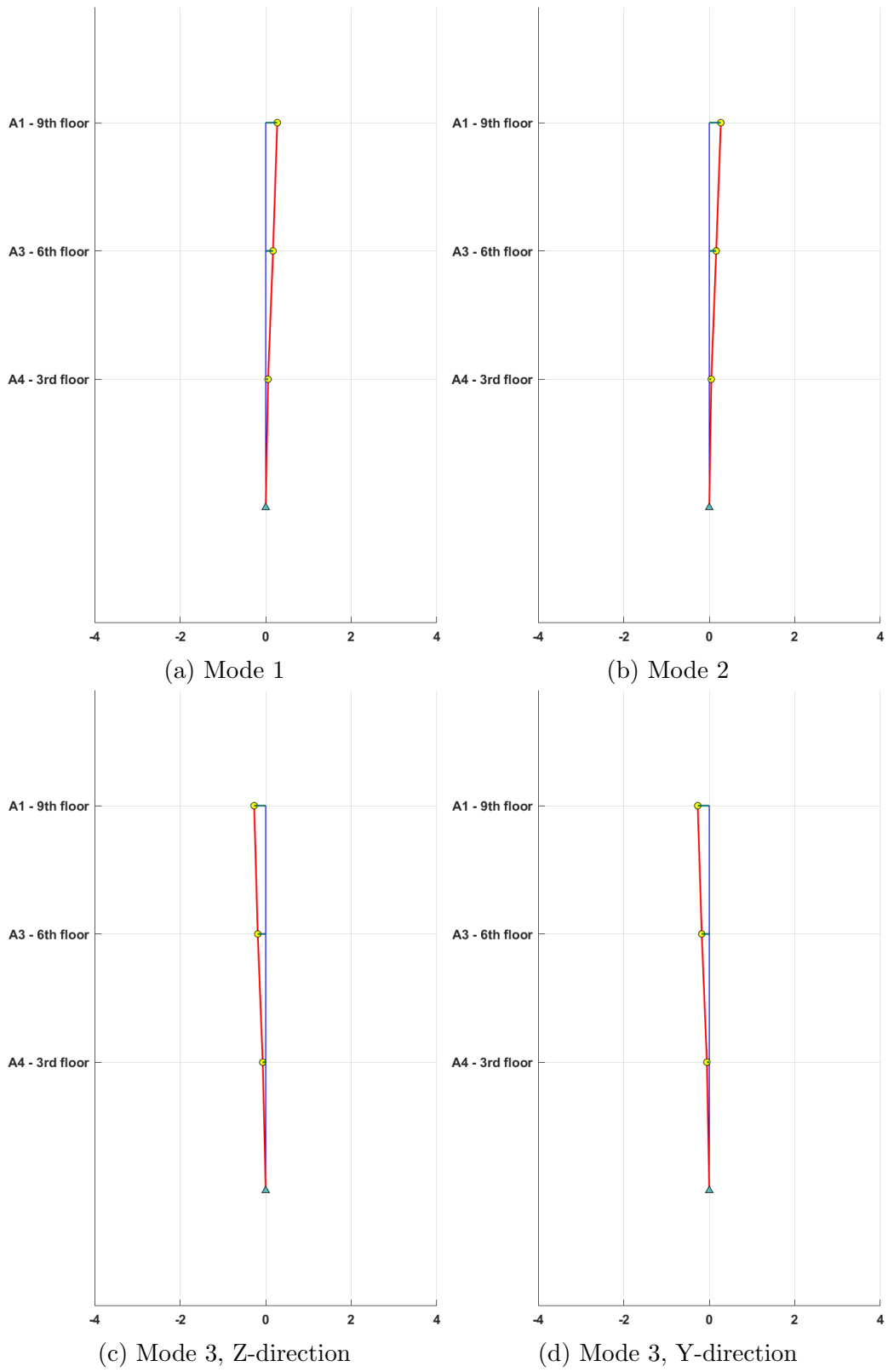
Figure C.3: Illustration of vertical mode shapes at MAL7

(a) Mode 1

(b) Mode 2

(c) Mode 3, Z-direction

(d) Mode 3, Y-direction
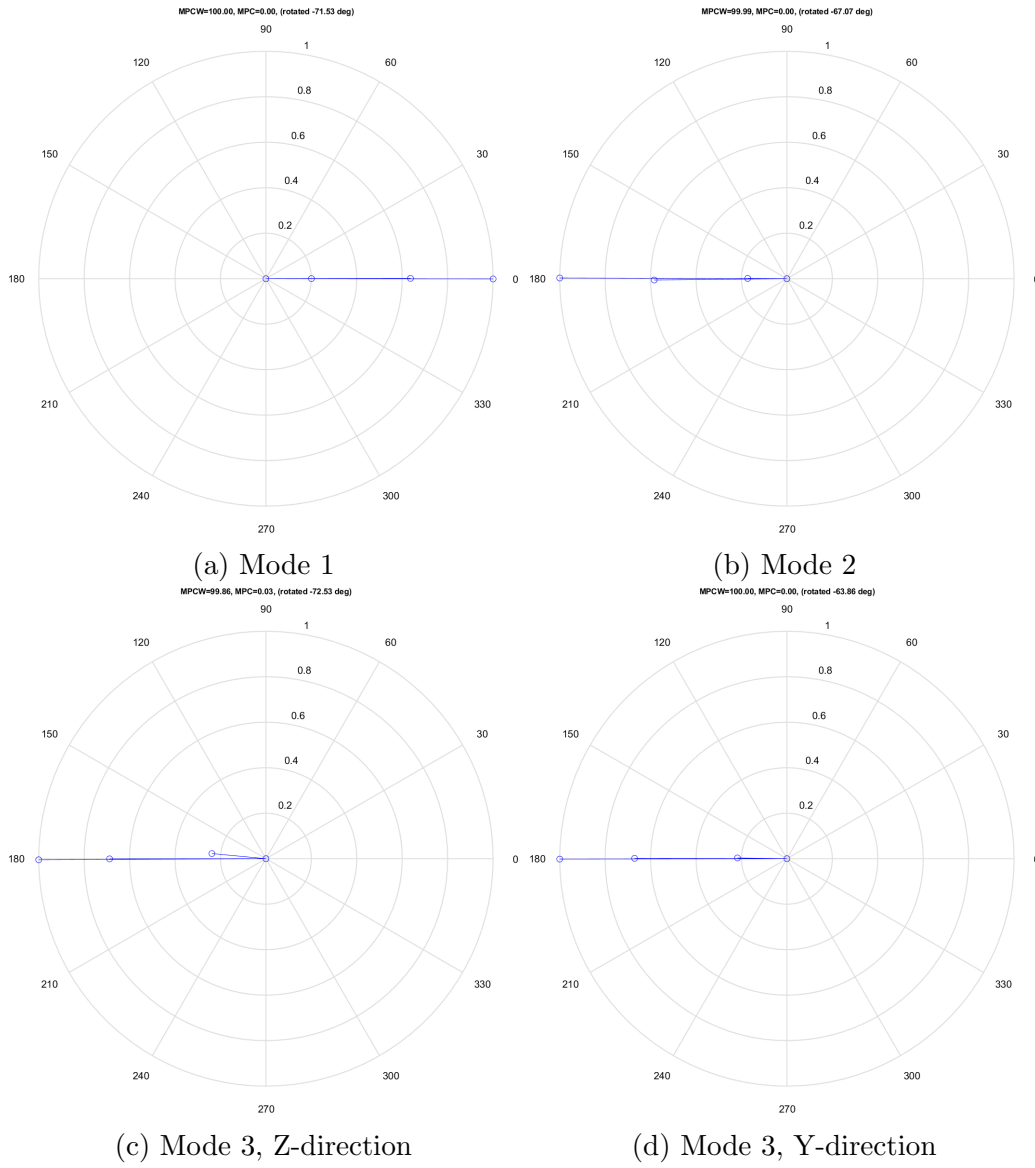
Figure C.4: Plots of the mode shapes in the complex plane

Peak acceleration

Table C.5: Peak accelerations at MAL7 from 6hr recording 2022-03-02-12-00-00Z

Accelerometer	Y-direction$[m/s^2]$	Z-direction$[m/s^2]$
A1	0.0060	0.0083
A2	0.0062	0.0089
A3	0.0038	0.0050
A4	0.0033	0.0040

Appendix D

Moholt Allmenning 8

This appendix presents the results at MAL8. Here there are only two six hour files. The files used for these results are:
- **2022-03-01-18-00-00Z**
- 2022-03-02-00-00-00Z

Stabilisation diagrams
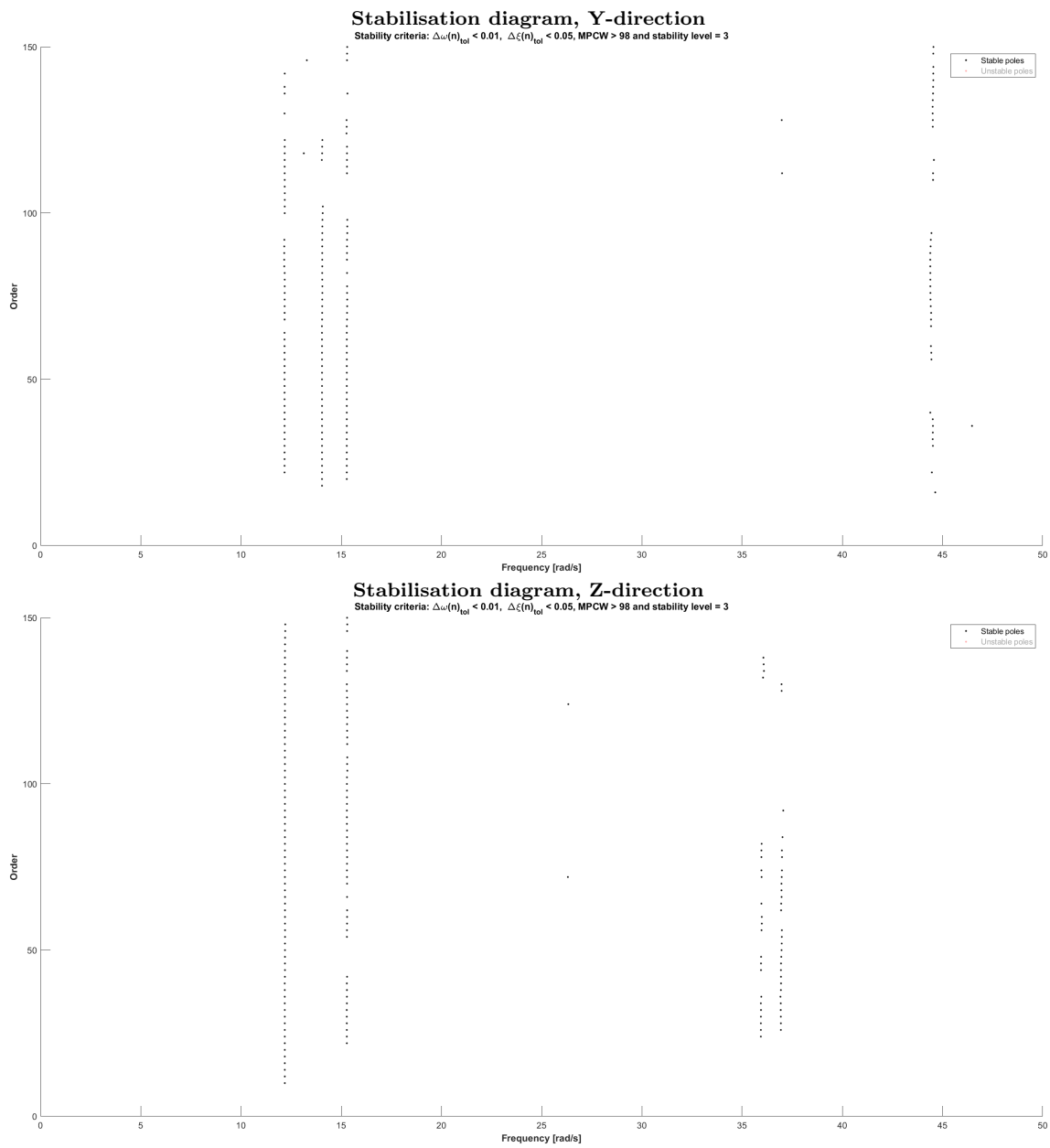
Figure D.1: Stabilisation diagrams from 6hr recording, 2022-03-01-18-00-00Z
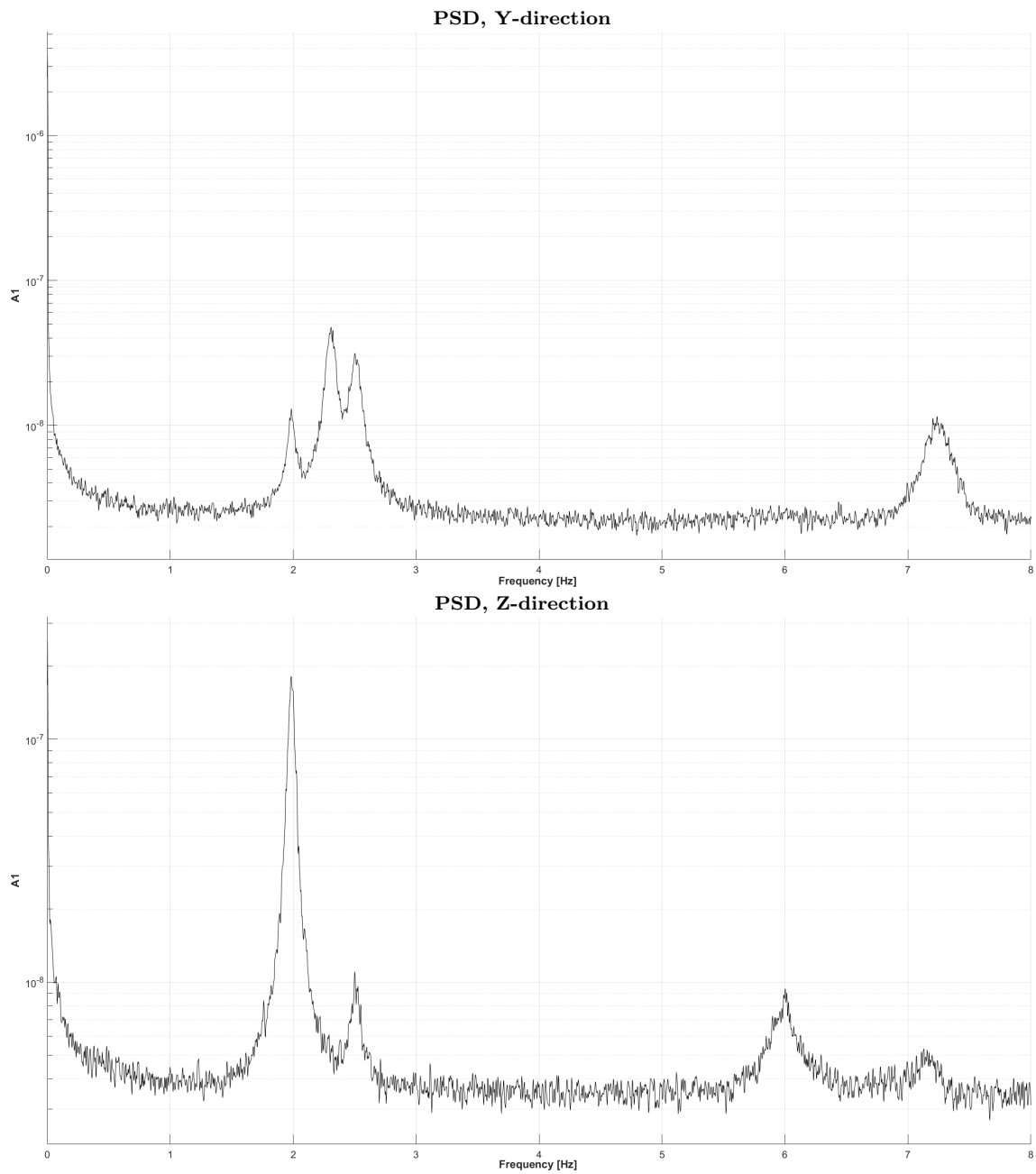
Power spectral densities

PSD, Y-direction

PSD, Z-direction

Figure D.2: Plots of PSD from accelerometer A1, 6hr recording, 2022-03-01-18-00-00Z

Natural frequencies

Table D.1: Natural frequencies at MAL8, including standard deviation and number of stable poles

Mode	$f_n[Hz]$	$\sigma_{f_n}[Hz]$	SP	$f_{n,PSD}[Hz]$
1	1.939	0.0007	256	1.931
2	2.233	0.0012	100	2.227
3	2.427	0.0011	215	2.424

Damping

Table D.2: Damping values for MAL8, including standard deviation and number of stable poles

Mode	$\xi_n[\%]$	$\sigma_{\xi_n}[\%]$	SP
1	1.548	0.0294	256
2	1.779	0.0550	100
3	1.726	0.0485	215

Mode shapes

Table D.3: Normalised mode shape vectors from MAL8

Accelerometer	Mode 1	Mode 2	Mode 3	Mode 3
A1	-1.0000	-1.0000	-1.0000	-1.0000
A3	-0.6113	-0.5552	-0.6432	-0.7169
A4	-0.1972	-0.1590	-0.2088	-0.2905
Direction	Z	Y	Y	Z
Order	60	60	60	60

Table D.4: MAC values from the comparison of MAL8 with the other buildings

Mode	MAL2	MAL5	MAL7	MAL11
1	0.9998	0.9998	0.9993	0.9998
2	0.9991	0.9997	0.9983	0.9984
3_y	0.9985	0.9994	1.0000	0.9992
3_z	0.9989	0.9995	0.9986	0.9824

(a) Mode 1

(b) Mode 2

(c) Mode 3, Z-direction
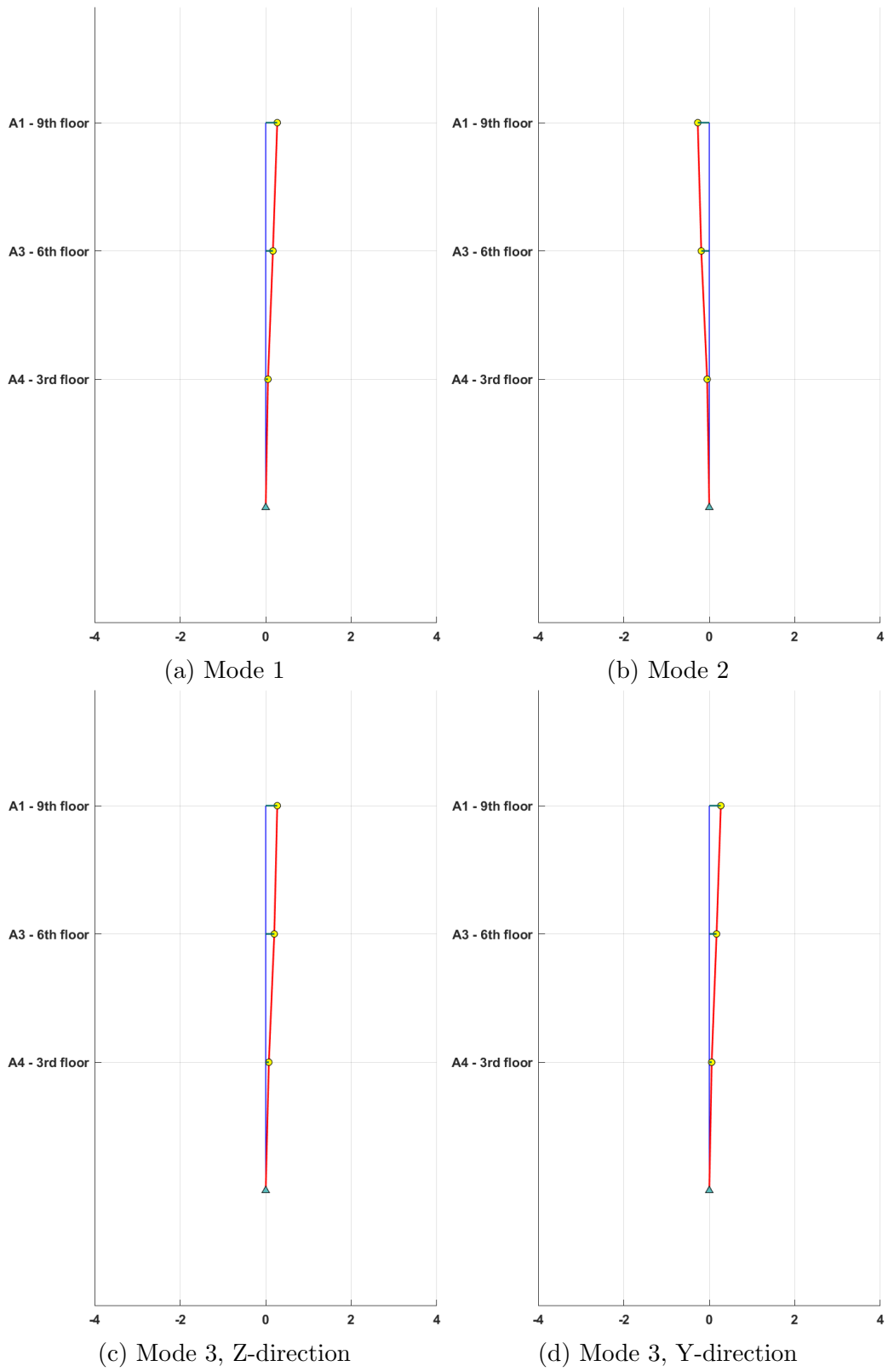
(d) Mode 3, Y-direction

Figure D.3: Illustration of vertical mode shapes at MAL8

(a) Mode 1

(b) Mode 2

(c) Mode 3, Z-direction

(d) Mode 3, Y-direction
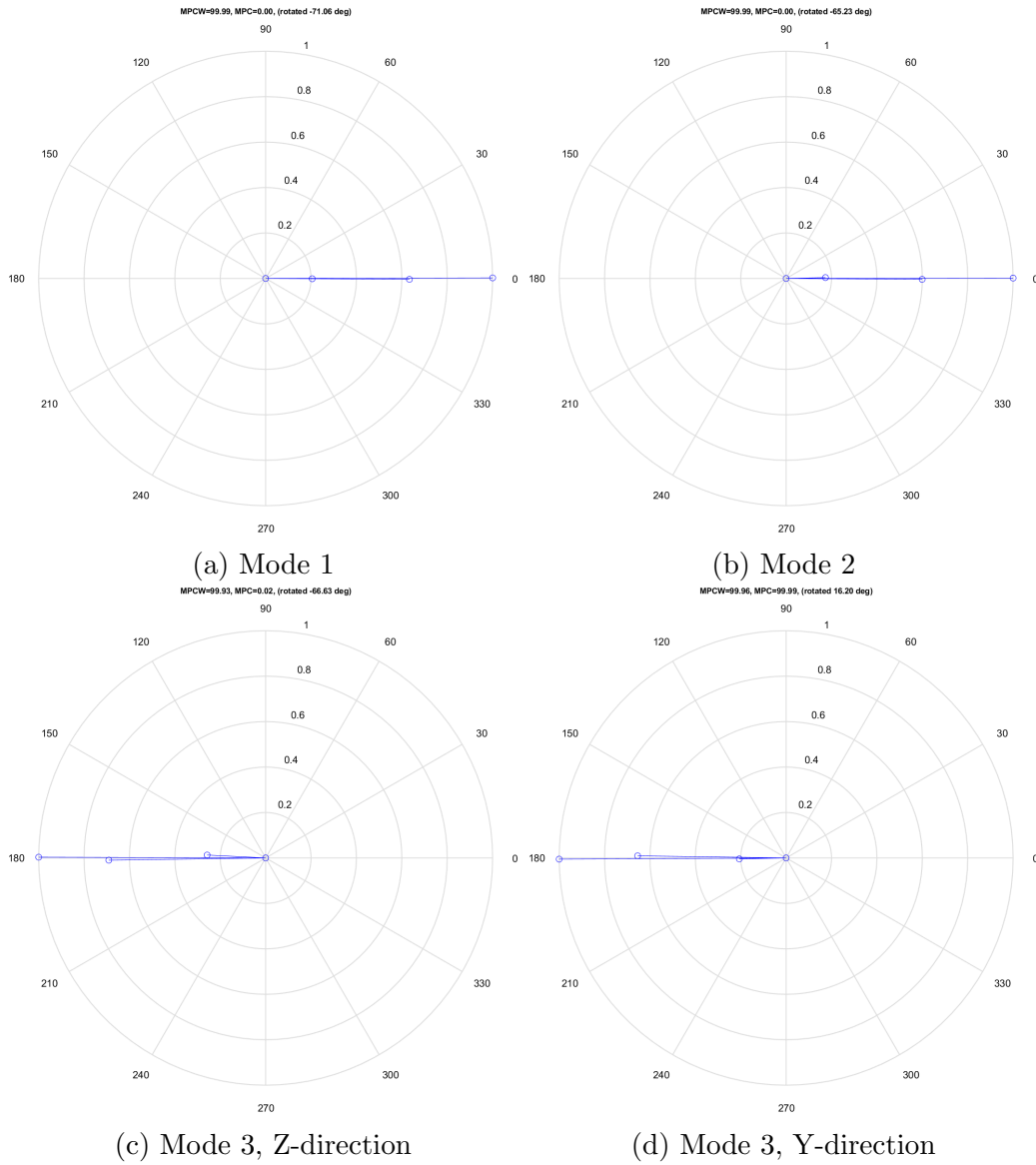
Figure D.4: Plots of the mode shapes in the complex plane

Peak acceleration

Table D.5: Peak accelerations at MAL8 from 6hr recording 2022-03-01-18-00-00Z

Accelerometer	Y-direction$[m/s^2]$	Z-direction$[m/s^2]$
A1	0.0069	0.0097
A2	0.0074	0.0080
A3	0.0045	0.0063
A4	0.0040	0.0041

Appendix E

Moholt Allmenning 11

This appendix presents the results at MAL11. The files used for these results are:
- **2022-02-23-18-00-00Z**
- 2022-02-24-00-00-00Z
- 2022-02-24-06-00-00Z

Stabilisation diagrams
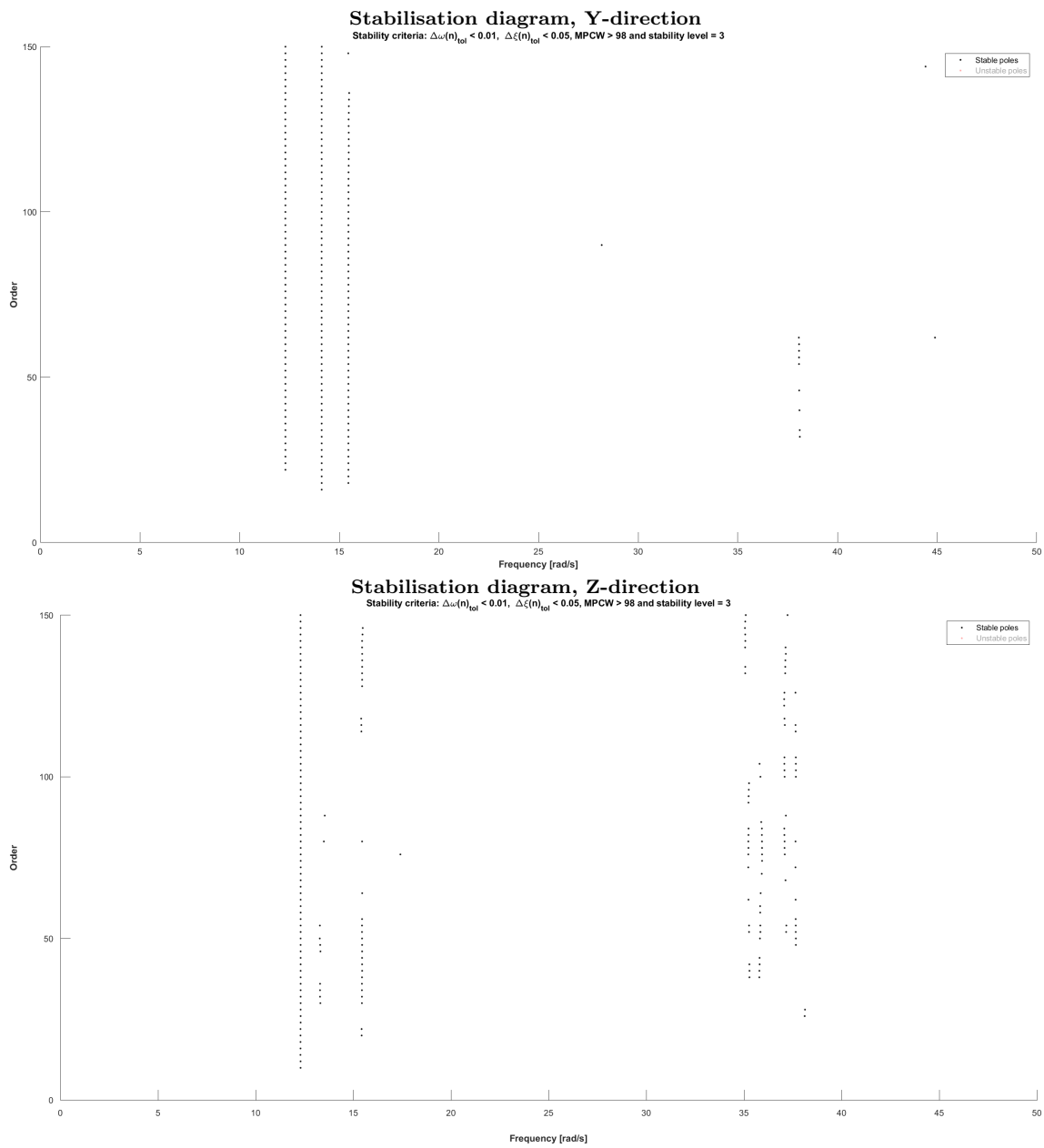
Figure E.1: Stabilisation diagrams from 6hr recording, 2022-02-23-18-00-00Z
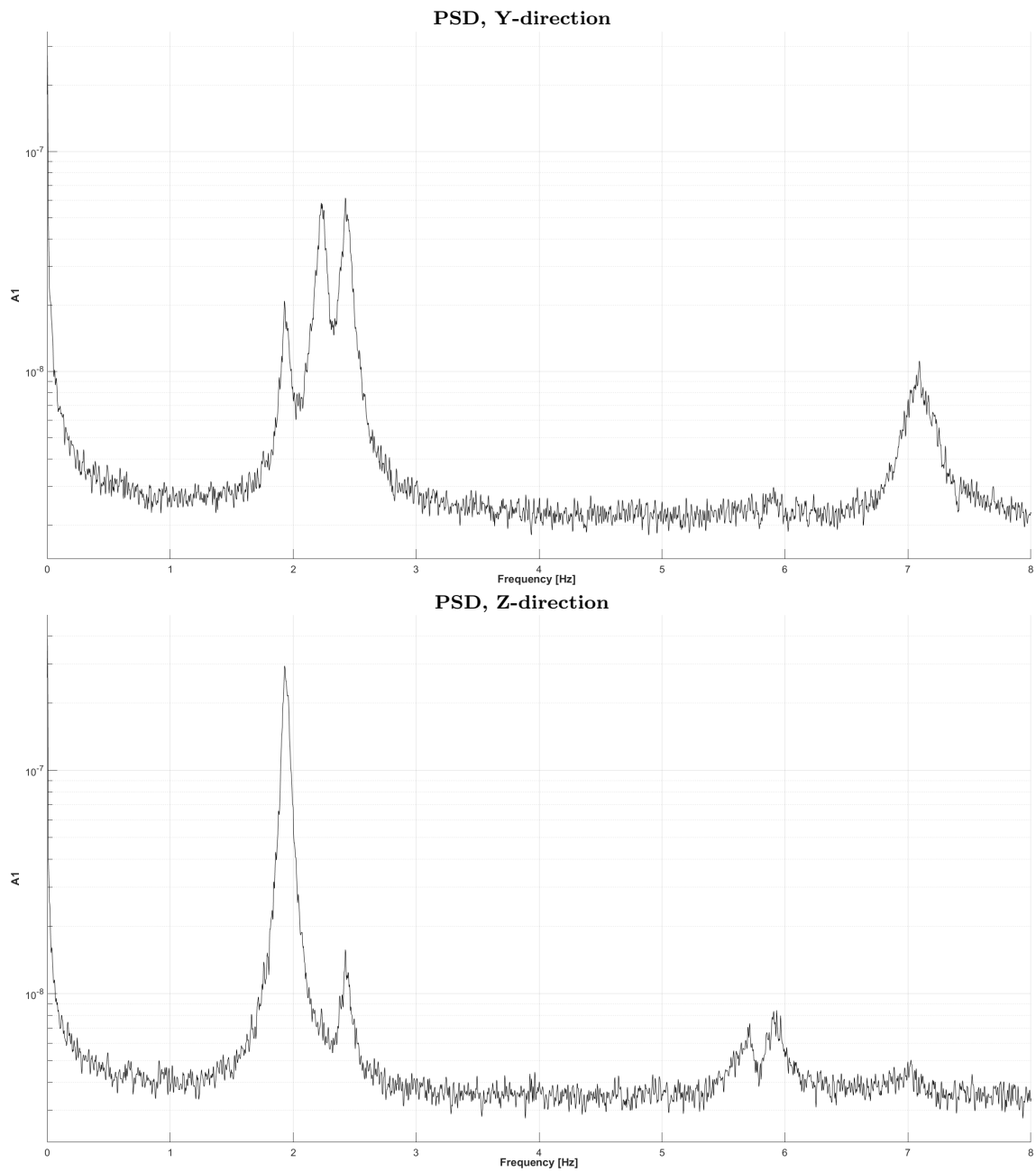
Power spectral densities

PSD, Y-direction

PSD, Z-direction
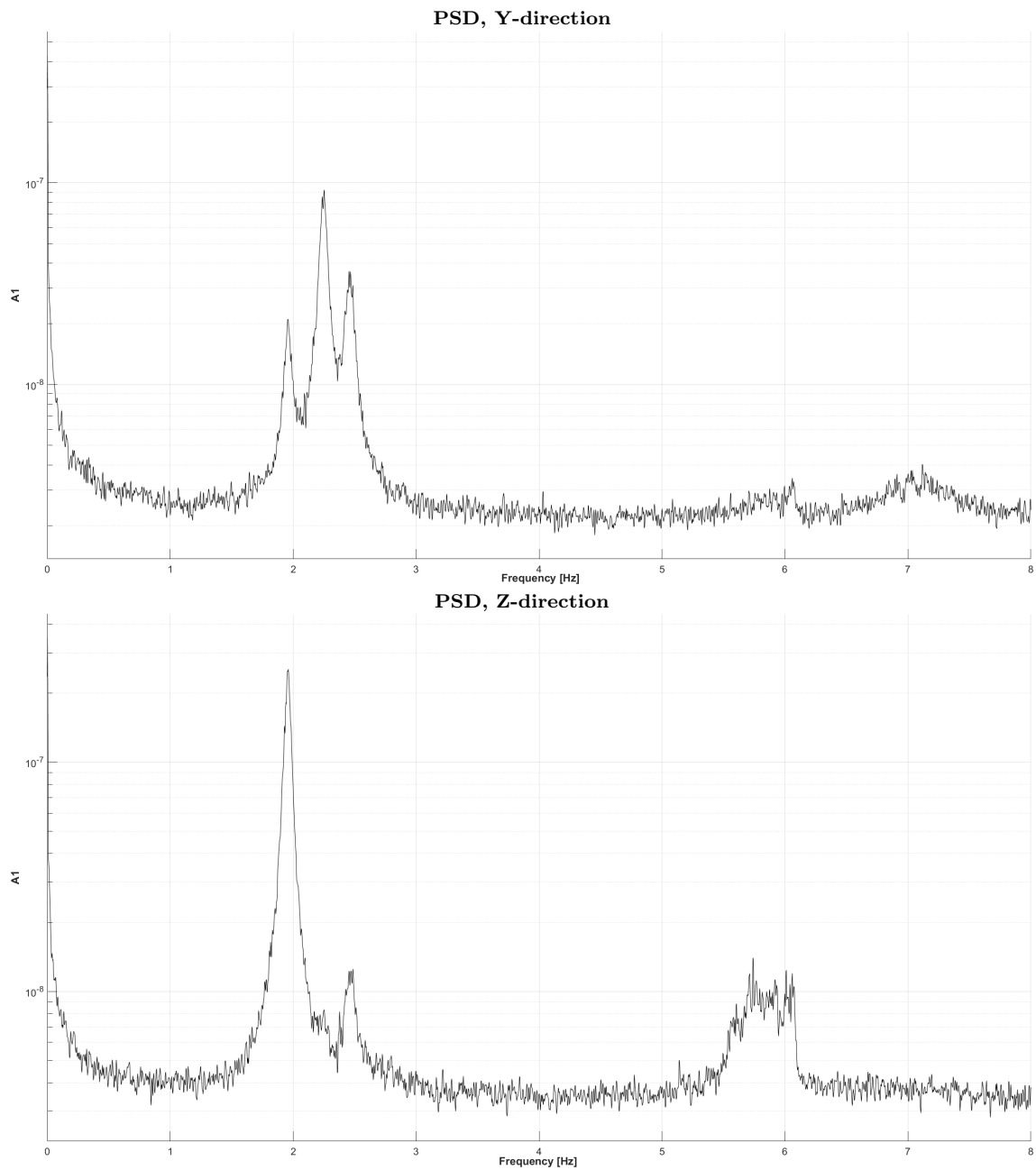
Figure E.2: Plots of PSD from accelerometer A1, 6hr recording, 2022-02-23-18-00-00Z

Natural frequencies

Table E.1: Natural frequencies at MAL11, including standard deviation and number of stable poles

Mode	$f_n[Hz]$	$\sigma_{f_n}[Hz]$	SP	$f_{n,PSD}[Hz]$
1	1.959	0.0004	402	1.960
2	2.251	0.0003	194	2.251
3	2.459	0.0015	289	2.469

Damping

Table E.2: Damping values for MAL11, including standard deviation and number of stable poles

Mode	$\xi_n[\%]$	$\sigma_{\xi_n}[\%]$	SP
1	1.433	0.0234	402
2	1.396	0.0201	194
3	1.624	0.0705	289

Mode shapes

Table E.3: Normalised mode shape vectors from MAL11

Accelerometer	Mode 1	Mode 2	Mode 3	Mode 3
A1	-1.0000	1.0000	-1.0000	-1.0000
A3	-0.6291	0.6006	-0.6727	-0.5279
A4	-0.1948	0.1873	-0.1877	-0.2567
Direction	Z	Y	Y	Z
Order	60	60	60	64

Table E.4: MAC values from the comparison of MAL11 with the other buildings

Mode	MAL2	MAL5	MAL7	MAL8
1	1.0000	1.0000	0.9997	0.9998
2	0.9998	0.9994	0.9995	0.9984
3_y	0.9986	0.9992	0.9991	0.9992
3_z	0.9893	0.9859	0.9908	0.9824

(a) Mode 1

(b) Mode 2

(c) Mode 3, Z-direction
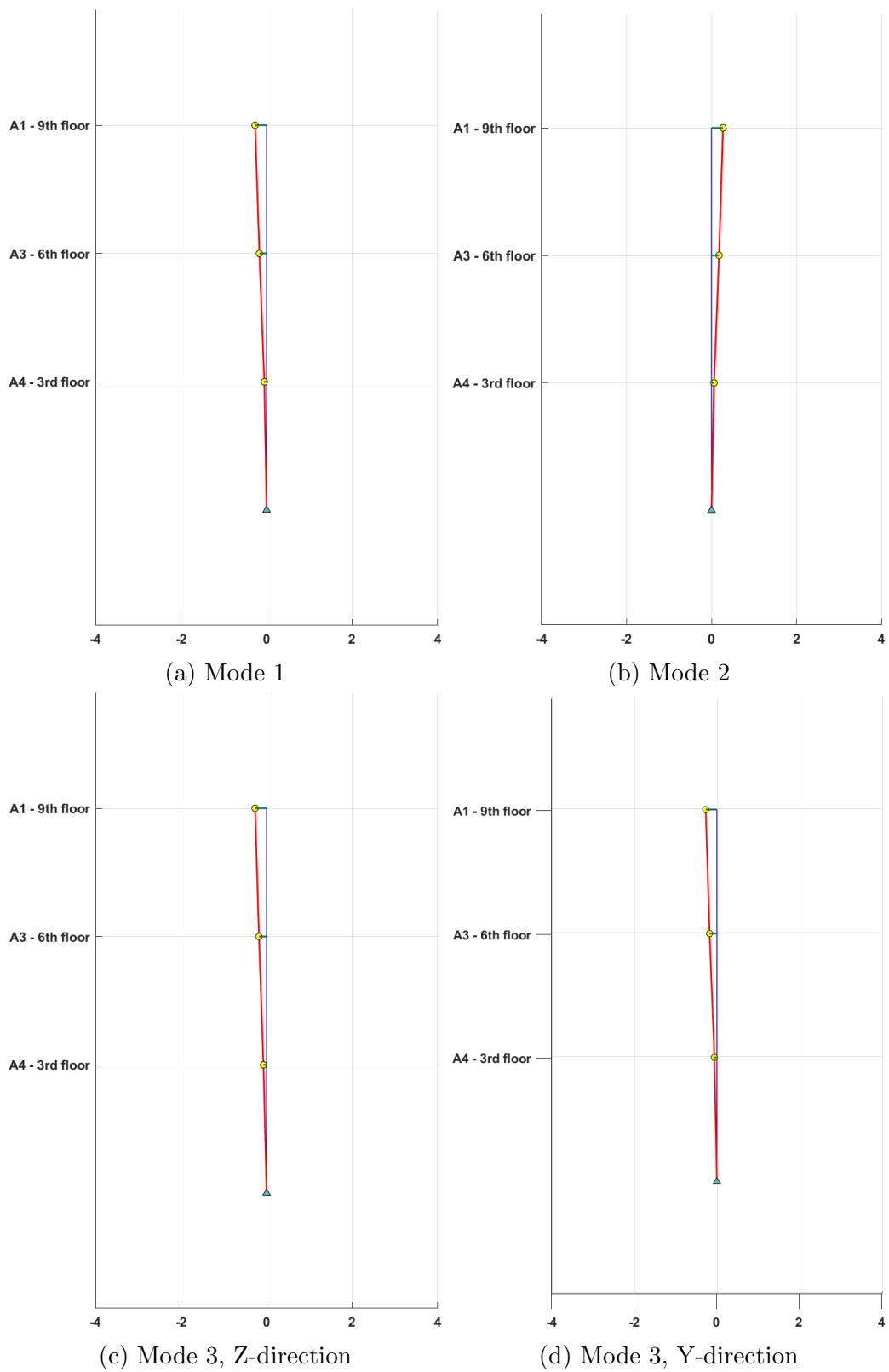
(d) Mode 3, Y-direction

Figure E.3: Illustration of vertical mode shapes at MAL11

(a) Mode 1

(b) Mode 2

(c) Mode 3, Z-direction
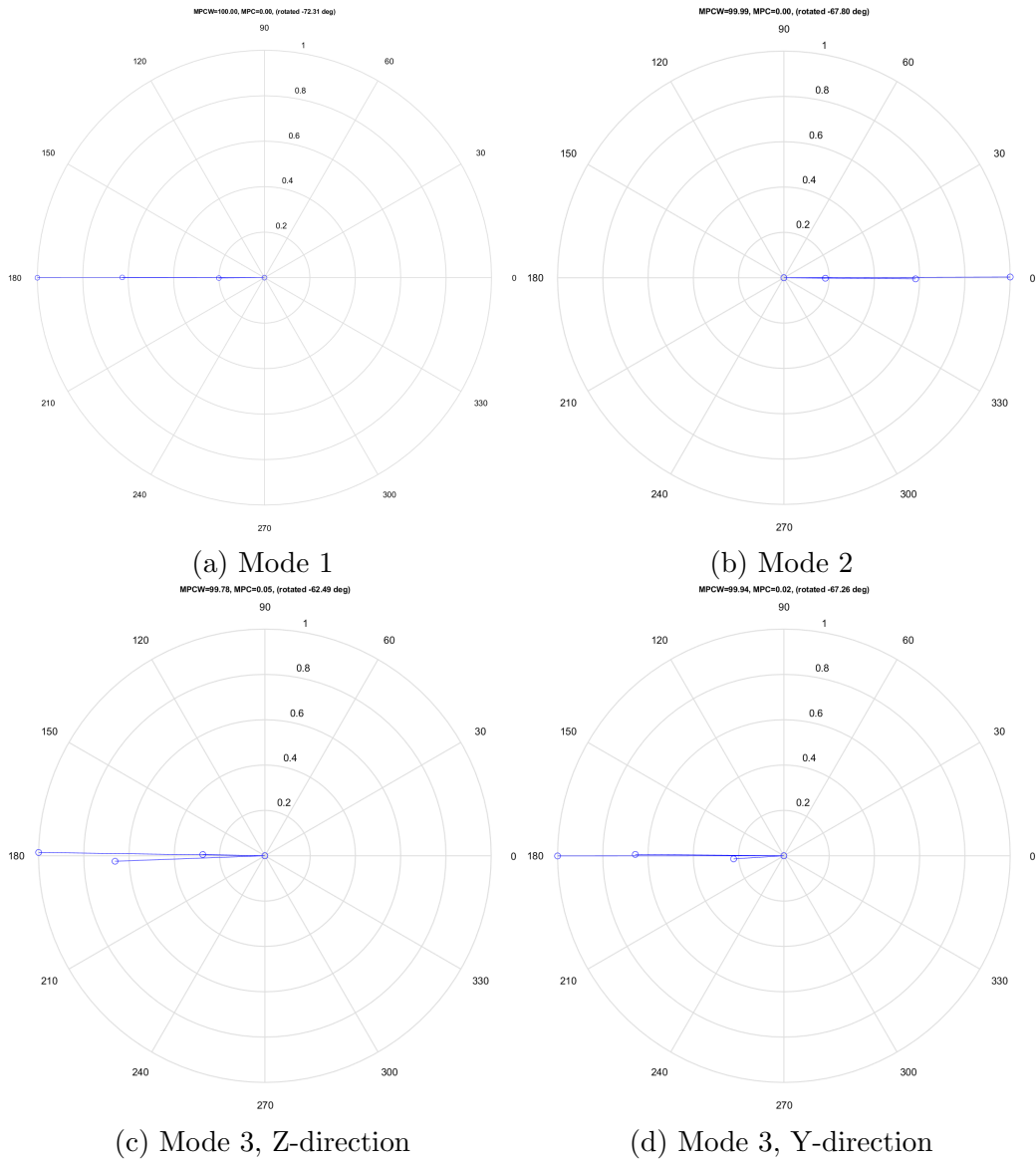
(d) Mode 3, Y-direction
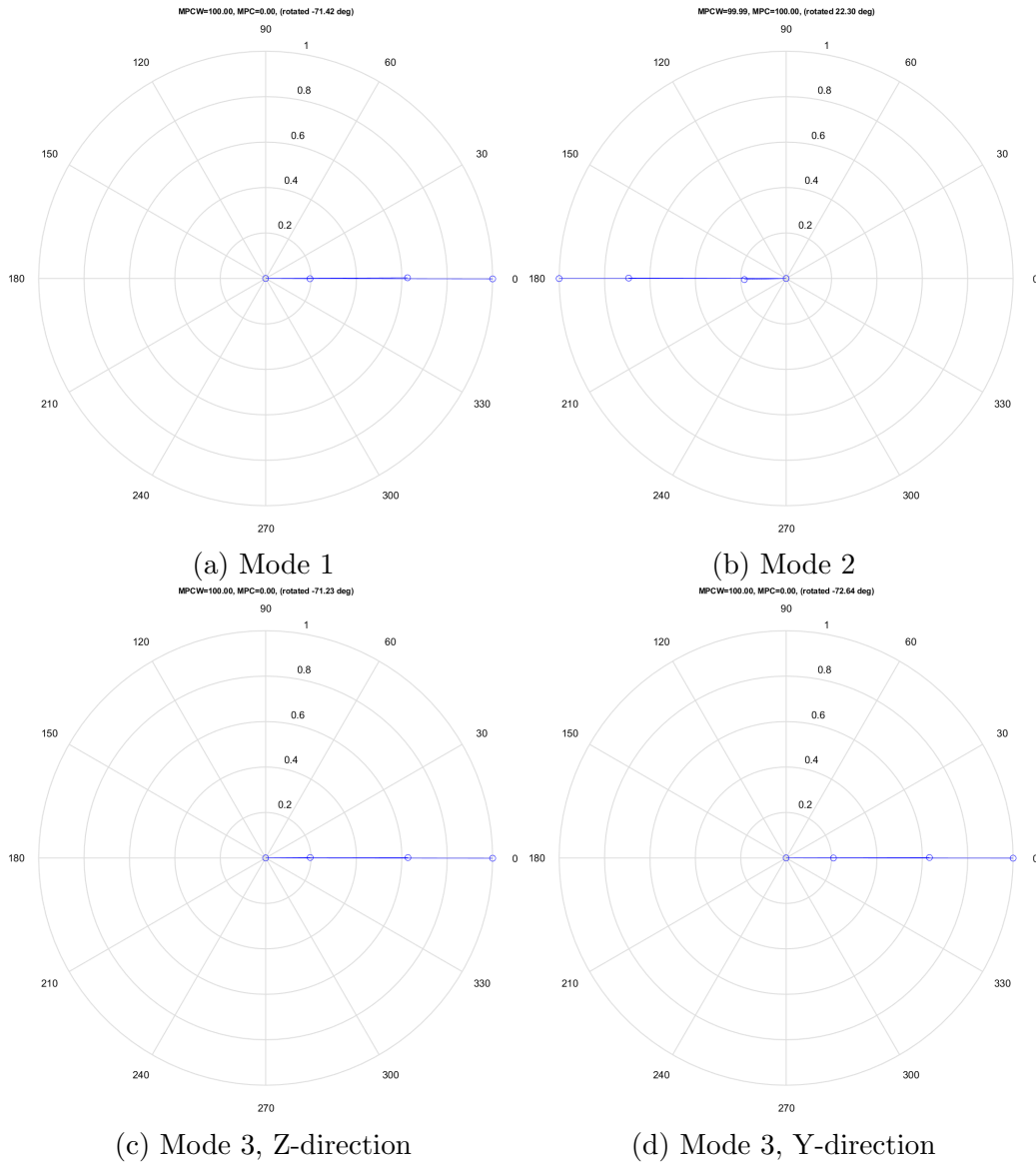
Figure E.4: Plots of the mode shapes in the complex plane

Peak acceleration

Table E.5: Peak accelerations at MAL11 from 6hr recording 2022-02-23-18-00-00Z

Accelerometer	Y-direction[m/s^2]	Z-direction[m/s^2]
A1	0.0055	0.0086
A2	0.0065	0.0078
A3	0.0043	0.0053
A4	0.0034	0.0042

Appendix F

Nonstructural mass

Screed and plaster

Table F.1: Nonstructural mass from CLT floor

Build up	Density [kg/m^3]	Thickness [mm]	Mass [ton]
Screed	2500	70	67
Plaster	600	13	3
Total			70

Dorm

Table F.2: Dorm items

Item	Weight [kg]	Amount	Total [kg]
Mounted wardrobe	55.4	15	831
Mounted shelf with pegs	7.3	15	109.5
Mounted shelf over bed	3.45	15	51.75
Mounted shelf under the windows	3.45	15	51.75
Mounted bed	17.15	15	257.25
Desk	28.8	15	432
Blind	0.21	15	3.15
Suspension for curtains	0.42	15	6.3
Shelf for pictures	1.96	15	29.4
Total			1772.1

Bathroom in dorm

Table F.3: Bathroom modules in dorms

Item	Weight [kg]	Amount	Total [kg]
Bathroom module	800	15	12000
Common area bathroom	800	1	800
Total			12800

Entrance

Table F.4: Entrance items

Item	Weight [kg]	Amount	Total [kg]
Open wardrobe	30	5	150
Shoe rack	4.04	5	20.2
Total			170.2

Hallway

Table F.5: Hallway items

Item	Weight [kg]	Amount	Total [kg]
Firehose	35	1	35
Fire instruction	0	1	-
House rules	0	1	-
Personal slate	8	8	64
Total			100.96

Common area and kitchen

Table F.6: Common area and kitchen items

Item	Weight [kg]	Amount	Total [kg]
Coach	41	2	82
TV-stand with drawers	27	1	27
Dinner table	36	3	108
Chairs	4	15	60
Mounted cabinet	12.58	8	100.64
Drawers	22	6	132
Refrigerator	71	5	355
Microwave oven	9.5	1	9.5
Dishwasher	47.33	1	47.33
Sink and crane	8	2	16
Integrated kettle	2.8	1	2.8
Stove	50.6	2	101.2
Trash cabinet	8	2	16
Cups and trays		2.6	
Total			1050.07

Personal belonging

Table F.7: Estimation of personal belongings

Item	Weight [kg]	Amount	Total [kg]
Humans	65	15	975
Personal belonging	75	15	1125
Total			2100

Windows and doors

Table F.8: Doors and windows

Windows ($30kg/m^2$)	Area [m^2]	Amount	Weight [kg]
Window 1	2.732	15	1229.57
Window 2	1.035	1	31.06
Window 3	2.142	1	64.26
Window 4	3.507	2	210.44
Window 5	4.742	2	284.54
Doors	17kg	15	255
Total			2074.89

Outer claddings

Table F.9: Calculations for outer claddings

	(kg/m^3)	Area $[m^2]$	Thickness $[mm]$	Weight $[kg]$
Kebony Character D-Fals K75 Glatt	570	190.025	123	13322.7
Total				13300

Elevator

The manufactor was contacted, but did not respond. Therefore the weight is estimated based similar elevators.

Table F.10: Estimation for elevator

	Total weight $[kg]$	Storeys	Weight at each storey
Kono Monospace 300 (without engine room)	12000	9	1333.34
Total			

Appendix G

Eurocode calculations

This appendix contains the calculations of peak accelerations according to NS-EN 1991-1-4. Since every building had slight differences in frequencies and damping ratios, the calculations were performed for every building. The 5x1 matrices in the calculations represent values for the five buildings. The place of each buildings value is displayed by equation (G.1), where ( ) is a placeholder for any of the variables where each building has its own value.

$$
( ) = \left[\begin{array}{c} MAL2 \\ MAL5 \\ MAL7 \\ MAL8 \\ MAL11 \end{array} \right] \tag{G.1}
$$

The calculations appear in the following order and on the following pages:
- Annex B, p.124-134
- Annex C - linear mode shape, p.135-145
- Annex C - parabolic mode shape, p.146-156

Calculation of peak acceleration according to NS-EN 1991-1-4, annex B

$$\sigma_{a,x}(z) := \frac{c_f \cdot \rho \cdot b \cdot I_v(z_s) \cdot (v_m)^2 \cdot z_s}{m_{1,x}} \cdot R \cdot K_x \cdot \phi_{1,x}(z) \quad \blacksquare \qquad\qquad (B.10)$$

Known parameters:

Air density: $\qquad\qquad \rho := 1.25 \dfrac{kg}{m^3}$

Values from DD-SSI of the five buildings:

First natural frequencies: $\qquad\qquad$ Structural damping values:

$$f_n := \begin{pmatrix} 2.022 \\ 1.978 \\ 1.985 \\ 1.939 \\ 1.959 \end{pmatrix} Hz \qquad\qquad \xi_n := \begin{pmatrix} 1.357 \\ 1.568 \\ 1.451 \\ 1.548 \\ 1.433 \end{pmatrix}\%$$

Structure height: $\qquad h := 27.06\,m$

Ref. height: $\qquad z_s := 0.6 \cdot h = 16.236\,m$
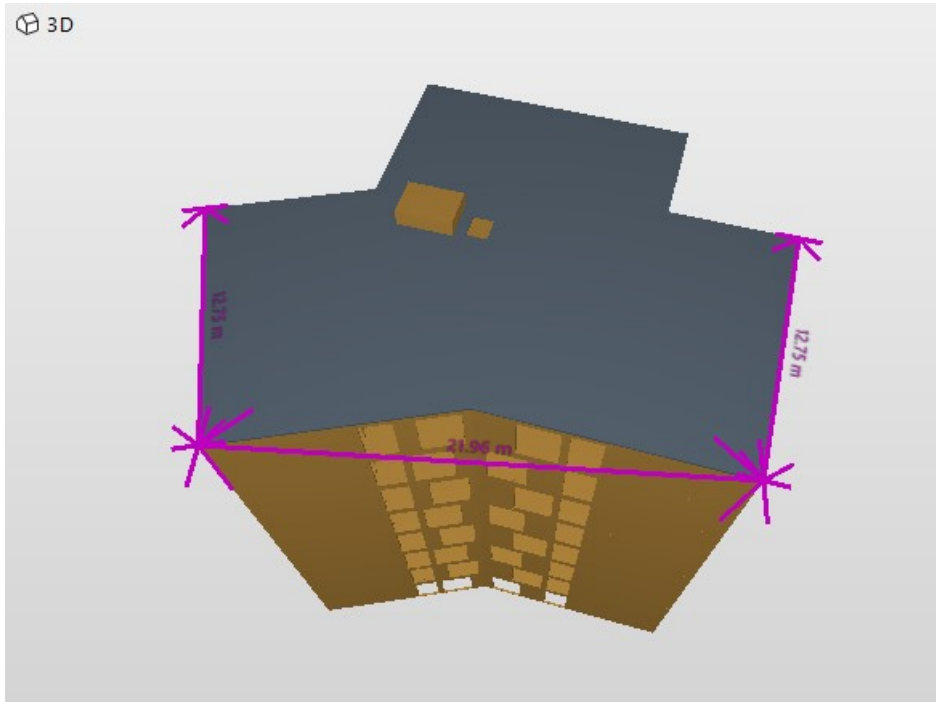
Fundamental mode shape according to section F.3

$\zeta := 1.0$

$\Phi_1 := \left(\dfrac{h}{h}\right)^{\zeta} = 1$

Force coefficient, c_f, given in 7.6(1):

$c_f := c_{f.0} \cdot \psi_r \cdot \psi_\lambda \quad \blacksquare \qquad\qquad\qquad\qquad\qquad\qquad (7.9)$

Note: the coefficient given in this section is meant for rectangular sections, and this building is Y-shaped. However, it has three rectangular shaped "legs" with sharp corners. This force coeffcient is therefore deemed to be the most correct to use, and it also yields the largest peak accelerations, meaning it is considered conservative.

In order to read the force coefficient of rectangular sections, values for width and depth must be decided. In this case, the width, where the wind is perpendicular to the surface, is set to 21.96m, and the depth is set to 12.75m, as seen in the figure above.

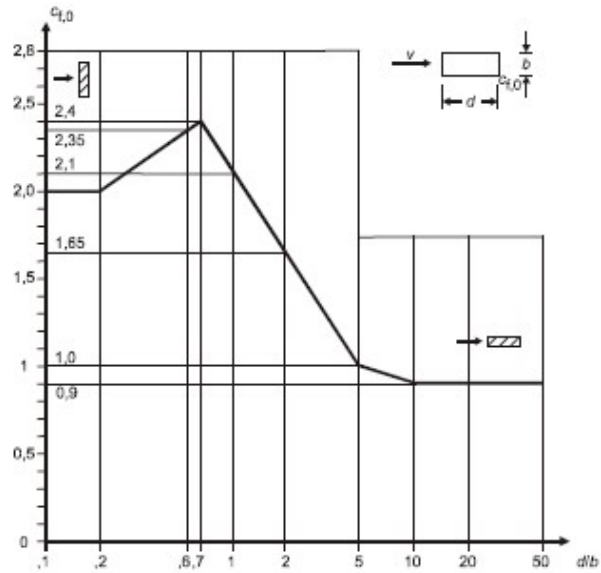$$b := 21.96\text{m} \quad d := 12.75\text{m} \qquad \frac{d}{b} = 0.581$$

Figure 7.23 — Force coefficients $c_{f,0}$ of rectangular sections with sharp corners and without free end flow

With the values given in figure 7.23, the force coefficient of rectangular sections can be found through interpolation:

$$c_{f.0} := 2 + \left(\frac{d}{b} - 0.2\right) \cdot \left[\frac{(2.35 - 2)}{(0.6 - 0.2)}\right] = 2.333$$

Reduction factor for rounded corners, according to figure 7.24:

$$\psi_r := 1.0 \qquad \text{Sharp edges}$$

Effective slenderness:

Table 7.16 — Recommended values of λ for cylinders, polygonal sections, rectangular sections, sharp edged structural sections and lattice structures

No.	Position of the structure, wind normal to the plane of the page	Effective slenderness λ
1		For polygonal, rectangular and sharp edged sections and lattice structures: for $\ell \geq 50$ m, $\lambda = 1.4 \, \ell/b$ or $\lambda = 70$, whichever is smaller for $\ell < 15$ m, $\lambda = 2 \, \ell/b$ or $\lambda = 70$, whichever is smaller
2		For circular cylinders: for $\ell \geq 50$, $\lambda = 0.7 \, \ell/b$ or $\lambda = 70$, whichever is smaller for $\ell < 15$ m, $\lambda = \ell/b$ or $\lambda = 70$, whichever is smaller For intermediate values of ℓ, linear interpolation should be used
3		
4		for $\ell \geq 50$ m, $\lambda = 0.7 \, \ell/b$ or $\lambda = 70$, whichever is larger for $\ell < 15$ m, $\lambda = \ell/b$ or $\lambda = 70$, whichever is larger For intermediate values of ℓ, linear interpolation should be used

Case number two from table 7.16:

$$1 := h$$

$$\lambda_{upper} := 1.4 \cdot \frac{1}{b} = 1.725 \qquad\qquad \lambda_{lower} := 2 \cdot \frac{1}{b} = 2.464$$

Interpolating between values:

$$\lambda := \lambda_{lower} - \frac{\left(\lambda_{lower} - \lambda_{upper}\right) \cdot \left(1 - 15\text{m}\right)}{50\text{m} - 15\text{m}} = 2.21$$

Figure 7.36 — Indicative values of the end-effect factor ψ_λ as a function of solidity ratio φ versus slenderness λ

With $\phi=1.0$ for this structure, the value for ψ_λ can be read from figure 7.36:

$\psi_\lambda := 0.62$

The force coefficient becomes:

$c_f := c_{f.0} \cdot \psi_\lambda = 1.446$

Turbulence intencity I_v and mean wind velocity v_m at height z_s, according to 4.4(1):

$c_{dir} := 1.0 \quad c_{season} := 1.0 \quad c_{alt} := 1.0 \quad c_{prob} := 1.0$ NA.4.2(2)P

The return period in NS-EN 1991-1-4 is usually set to 50 years. Since the measurements only takes place in one day, the return period must be lowered. One year return period is chosen since the recommendations in ISO10137 is for wind-induced vibration for a one year return period.

To approximate the probability, p, the Poisson ratio is used.

Return period for one year:

$K := 0.2 \qquad n := 0.5$ NA.4.2(2)P

$$p(x) := 1 - \exp\left(\frac{-1}{x}\right)$$

$$p := p(1) = 0.632$$

$$c_{prob} := \left(\frac{1 - K \cdot \ln(-\ln(1 - p))}{1 - K \cdot \ln(-\ln(0.98))}\right)^n = 0.749 \qquad\qquad (4.2)$$

$$v_{b.0} := 26\frac{m}{s} \qquad\qquad \text{Table NA.4(901.1)}$$

Basic wind:

$$v_b := c_{dir} \cdot c_{season} \cdot c_{alt} \cdot c_{prob} \cdot v_{b.0} = 19.486\frac{m}{s} \qquad\qquad (NA.4.1)$$

Turbulence category 4, table NA.4.1:

$$k_r := 0.24 \qquad z_0 := 1.0m \qquad z_{min} := 16m$$

$$k_l := 1.0 \qquad c_0 := 1.0 \qquad\qquad 4.3.3$$

$$I_v := \frac{k_l}{c_0 \cdot \ln\left(\dfrac{z_s}{z_0}\right)} = 0.359 \qquad\qquad (4.7)$$

Mean wind velocity:

$$c_r := k_r \cdot \ln\left(\frac{z_s}{z_0}\right) = 0.669 \qquad\qquad (4.4)$$

$$v_m := c_r \cdot c_0 \cdot v_b = 13.035\frac{m}{s} \qquad\qquad (4.3)$$

Square root of the resonant response, R^2, according to B.2(5):

Turbulence length scale:

$$z_t := 200\,\text{m} \quad L_t := 300\,\text{m} \qquad \alpha := 0.67 + 0.05 \cdot \ln\!\left(\frac{z_0}{\text{m}}\right) = 0.67$$

$$L := L_t \cdot \left(\frac{z_s}{z_t}\right)^{\alpha} = 55.777\,\text{m} \tag{B.1}$$

Non-dimensional frequency:

$$f_L := \frac{f_n \cdot L}{v_m} = \begin{pmatrix} 8.652 \\ 8.464 \\ 8.494 \\ 8.297 \\ 8.383 \end{pmatrix}$$

Wind power spectral density function, S_L, given in B.1(2):

$$S_L := \frac{6.8 \cdot f_L}{\left(1 + 10.2 \cdot f_L\right)^{\frac{5}{3}}} = \begin{pmatrix} 0.033 \\ 0.033 \\ 0.033 \\ 0.034 \\ 0.034 \end{pmatrix} \tag{B.2}$$

Aerodynamic admittance functions, R_h and R_b, given in B.2(6):

$$\eta_h := \frac{4.6 \cdot h}{L} \cdot f_L = \begin{pmatrix} 19.309 \\ 18.889 \\ 18.956 \\ 18.517 \\ 18.708 \end{pmatrix} \quad R_h := \frac{1}{\eta_h} - \frac{1}{2 \cdot \left(\overrightarrow{\eta_h}\right)^2} + \frac{1}{2 \cdot \left(\overrightarrow{\eta_h}\right)^2} \cdot \exp\!\left(-2 \cdot \overrightarrow{\eta_h}\right) = \begin{pmatrix} 0.05 \\ 0.052 \\ 0.051 \\ 0.053 \\ 0.052 \end{pmatrix}$$

$$\tag{B.7}$$

$$\eta_b := \frac{4.6 \cdot b}{L} \cdot f_L = \begin{pmatrix} 15.67 \\ 15.329 \\ 15.383 \\ 15.027 \\ 15.182 \end{pmatrix} \quad R_b := \frac{1}{\eta_b} - \frac{1}{2 \cdot \left(\vec{\eta_b}\right)^2} + \frac{1}{2 \cdot \left(\vec{\eta_b}\right)^2} \cdot \exp\left(-2 \cdot \vec{\eta_b}\right) = \begin{pmatrix} 0.062 \\ 0.063 \\ 0.063 \\ 0.064 \\ 0.064 \end{pmatrix}$$

<div align="right">(B.8)</div>

Total logarithmic decrement of damping, $\delta = \delta_a + \delta_s$, given by the aerodynamic damping and structural damping respectively, as per F.5:

F.4(2) states: "*For cantilevered structures with a varying mass distribution, the equivalent mass per unit length, may be approximated by the average value of m over the upper third of the structure, h_3*"

$$h_3 := \frac{h}{3} = 9.02\,\text{m}$$

Extracting the mass of the top three floors from the ABAQUS model, yields the following mass per length:

$$m_e := \frac{526.81\,\text{tonne}}{h_3} = 5.84 \times 10^4\,\frac{\text{kg}}{\text{m}}$$

By setting equation (F.16) and (F.18) equal to each other, and solving for μ_e, we get the equivalent mass per unit area:

$$\mu_e := \frac{m_e}{b} = 2.66 \times 10^3\,\frac{\text{kg}}{\text{m}^2}$$

Logarithmic decrement of aerodynamic damping, according to (F.16) and (F.18):

$$\delta_{a.1} := \frac{c_f \cdot \rho \cdot v_m}{2 \cdot f_n \cdot \mu_e} = \begin{pmatrix} 2.191 \times 10^{-3} \\ 2.24 \times 10^{-3} \\ 2.232 \times 10^{-3} \\ 2.285 \times 10^{-3} \\ 2.262 \times 10^{-3} \end{pmatrix} \tag{F.16}$$

$$\delta_{a.2} := \frac{c_f \cdot \rho \cdot b \cdot v_m}{2 \cdot f_n \cdot m_e} = \begin{pmatrix} 2.191 \times 10^{-3} \\ 2.24 \times 10^{-3} \\ 2.232 \times 10^{-3} \\ 2.285 \times 10^{-3} \\ 2.262 \times 10^{-3} \end{pmatrix} \tag{F.18}$$

Logarithmic decrement of structural damping, averages from measurements of the buildings:

$$\delta_s := \xi_n \cdot 2 \cdot \pi = \begin{pmatrix} 0.085 \\ 0.099 \\ 0.091 \\ 0.097 \\ 0.09 \end{pmatrix}$$

Thus, the total damping is:

$$\delta := \delta_{a.1} + \delta_s = \begin{pmatrix} 0.087 \\ 0.101 \\ 0.093 \\ 0.1 \\ 0.092 \end{pmatrix} \tag{F.15}$$

Square root of resonant response can now be found, given in B.2(5):

$$R := \sqrt{\frac{\pi^2}{2} \cdot \overrightarrow{\left(\frac{S_L \cdot R_h \cdot R_b}{\delta}\right)}} = \begin{pmatrix} 0.076 \\ 0.073 \\ 0.076 \\ 0.075 \\ 0.077 \end{pmatrix} \quad \text{(B.6)}$$

The non dimensional coefficient can be approximated as the following, from (B.12):

$$K_x := \frac{(2 \cdot \zeta + 1)\left[(\zeta + 1) \cdot \left(\ln\left(\frac{z_s}{z_0}\right) + 0.5\right) - 1\right]}{(\zeta + 1)^2 \cdot \ln\left(\frac{z_s}{z_0}\right)} = 1.5 \quad \text{(B.12)}$$

The standard deviation can now be calculated, as per (B.10):

$$\sigma_{a.x} := \frac{c_f \cdot \rho \cdot b \cdot I_v \cdot v_m^2}{m_e} \cdot R \cdot K_x \cdot \Phi_1 = \begin{pmatrix} 4.736 \times 10^{-3} \\ 4.54 \times 10^{-3} \\ 4.694 \times 10^{-3} \\ 4.686 \times 10^{-3} \\ 4.803 \times 10^{-3} \end{pmatrix} \frac{m}{s^2} \quad \text{(B.10)}$$

B.4(4) states: "*The characteristic peak accelerations are obtained by multiplying the standard deviation in B.4(2) by the peak factor in B.2(3) using the frequency as upcrossing frequency, i.e. $v=n_{1,x}$*"

Peak factor, k_p, as per B.2(3):

$$T := 600s$$

$$k_p := \sqrt{2 \cdot \ln(f_n \cdot T)} + \frac{0.6}{\sqrt{2 \ln(f_n \cdot T)}} = \begin{pmatrix} 3.928 \\ 3.922 \\ 3.923 \\ 3.917 \\ 3.92 \end{pmatrix} \qquad \text{All values > 3, OK!} \qquad \text{(B.4)}$$

Peak acceleration:

$$a_{peak} := \overrightarrow{(\sigma_{a.x} \cdot k_p)} = \begin{pmatrix} 0.019 \\ 0.018 \\ 0.018 \\ 0.018 \\ 0.019 \end{pmatrix} \frac{m}{s^2}$$

Calculation of peak acceleration according to NS-EN 1-4-1991, annex C with linear mode shape

C.4(3) states: "*The characteristic peak accelerations are obtained by multiplying the standard deviation in C.4(2) by the peak factor in B.2(3) using the natural frequency as upcrossing frequency, i.e. v = n_{1,x}*"

The standard deviation is given in C.4(2):

$$\sigma_{a.x}(y,z) := c_f \cdot \rho \cdot I_v(z_s) \cdot v_m^2(z_s) \cdot R \cdot \frac{K_y \cdot K_z \cdot \Phi(y,z)^{\blacksquare}}{\mu_{ref} \cdot \Phi_{max}}$$

(C.4)

Known parameters:

Air density:
$$\rho := 1.25 \frac{kg}{m^3}$$

First natural frequencies:

$$f_n := \begin{pmatrix} 2.022 \\ 1.978 \\ 1.985 \\ 1.939 \\ 1.959 \end{pmatrix} Hz$$

Structural damping values:

$$\xi_n := \begin{pmatrix} 1.357 \\ 1.568 \\ 1.451 \\ 1.548 \\ 1.433 \end{pmatrix} \%$$

Structure height: $h := 27.06\,m$

Ref. height: $z_s := 0.6 \cdot h = 16.236\,m$

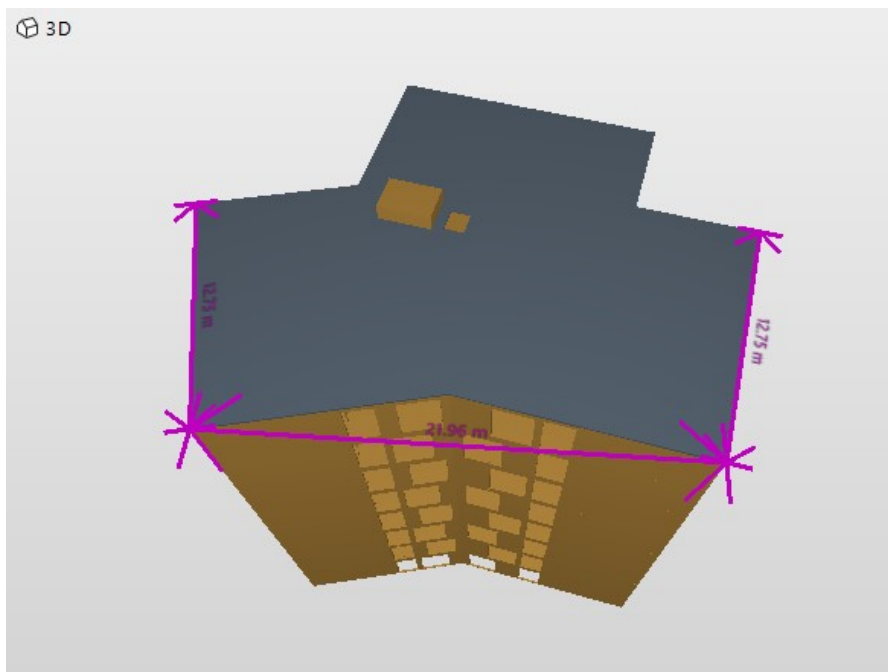Fundamental mode shape according to section F.3

$$\zeta := 1.0$$

$$\Phi_1 := \left(\frac{h}{h}\right)^\zeta = 1$$

Force coefficient, c_f, given in 7.6(1):

$$c_f := c_{f.0} \cdot \psi_r \cdot \psi_\lambda^{\blacksquare}$$
<div align="right">(7.9)</div>

Note: the coefficient given in this section is meant for rectangular sections, and this building is Y-shaped. However, it has three rectangular shaped "legs" with sharp corners. This force coeffcient is therefore deemed to be the most correct to use, and it also yields the largest peak accelerations, meaning it is considered conservative.

In order to read the force coefficient of rectangular sections, values for width and depth must be decided. In this case, the width, where the wind is perpendicular to the surface, is set to 21.96m, and the depth is set to 12.75m, as seen in the figure above.

$$b := 21.96m \quad d := 12.75m \quad \frac{d}{b} = 0.581$$
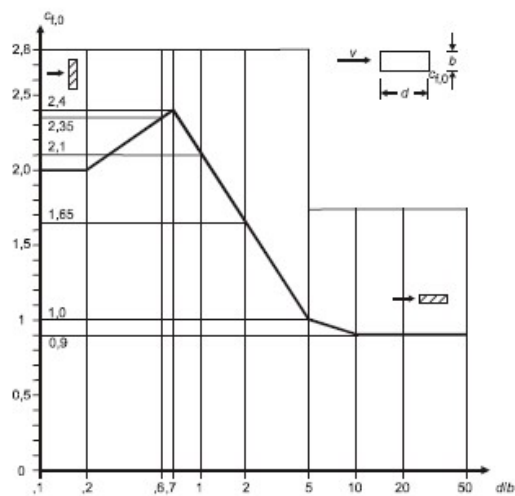

Figure 7.23 — Force coefficients $c_{f,0}$ of rectangular sections with sharp corners and without free end flow

With the values given in figure 7.23, the force coefficient of rectangular sections can be found through interpolation:

$$c_{f.0} := 2 + \left(\frac{d}{b} - 0.2\right) \cdot \left[\frac{(2.35 - 2)}{(0.6 - 0.2)}\right] = 2.333$$

Reduction factor for rounded corners, according to figure 7.24:

$$\psi_r := 1.0 \quad \text{Sharp edges}$$

Effective slenderness:

Table 7.16 — Recommended values of λ for cylinders, polygonal sections, rectangular sections, sharp edged structural sections and lattice structures

Case number two from table 7.16:

$l := h$

$$\lambda_{upper} := 1.4 \cdot \frac{l}{b} = 1.725 \qquad\qquad \lambda_{lower} := 2 \cdot \frac{l}{b} = 2.464$$

Interpolating between values:

$$\lambda := \lambda_{lower} - \frac{\left(\lambda_{lower} - \lambda_{upper}\right) \cdot (l - 15m)}{50m - 15m} = 2.21$$

Figure 7.36 — Indicative values of the end-effect factor ψ_λ as a function of solidity ratio φ versus slenderness λ

With φ=1.0 for this structure, the value for ψ_λ can be read from figure 7.36:

$$\psi_\lambda := 0.62$$

The force coefficient becomes:

$$c_f := c_{f.0} \cdot \psi_r \cdot \psi_\lambda = 1.446 \tag{7.9}$$

Turbulence intencity I_v and mean wind velocity v_m at height z_s, according to 4.4(1):

$$c_{dir} := 1.0 \quad c_{season} := 1.0 \quad c_{alt} := 1.0 \quad c_{prob} := 1.0 \qquad \text{NA.4.2(2)P}$$

The return period in NS-EN 1-4-1991, is usually set to 50 years. Since the measurements only takes place in one day, the return period must be lowered. The return period is set to one year to represent best the probability of faster gusts of wind on the day of measuring.

To approximate the probability, p, the Poisson ratio is used.

Return period for one year:

$$K := 0.2 \qquad n := 0.5 \qquad\qquad\qquad\qquad \text{NA.4.2(2)P}$$

$$p(x) := 1 - \exp\left(\frac{-1}{x}\right)$$

$$p := p(1) = 0.632$$

$$c_{prob} := \left(\frac{1 - K \cdot \ln(-\ln(1 - p))}{1 - K \cdot \ln(-\ln(0.98))}\right)^n = 0.749 \qquad\qquad (4.2)$$

$$v_{b.0} := 26 \frac{m}{s} \qquad\qquad\qquad\qquad \text{Table NA.4(901.1)}$$

Basic wind:

$$v_b := c_{dir} \cdot c_{season} \cdot c_{alt} \cdot c_{prob} \cdot v_{b.0} = 19.486 \frac{m}{s} \qquad\qquad \text{(NA.4.1)}$$

Turbulence category 4, table NA.4.1:

$$k_r := 0.24 \qquad z_0 := 1.0m \qquad z_{min} := 16m$$

$$k_l := 1.0 \qquad c_0 := 1.0 \qquad\qquad\qquad\qquad 4.3.3$$

$$I_v := \frac{k_l}{c_0 \cdot \ln\left(\dfrac{z_s}{z_0}\right)} = 0.359 \qquad\qquad (4.7)$$

Mean wind velocity:

$$c_r := k_r \cdot \ln\left(\frac{z_s}{z_0}\right) = 0.669 \qquad\qquad (4.4)$$

$$v_m := c_r \cdot c_0 \cdot v_b = 13.035 \frac{m}{s} \qquad\qquad (4.3)$$

Square root of the resonant response, R^2, given in C.2(4):

$$R := \sqrt{\frac{\pi^2}{2 \cdot \delta} \cdot S_L(z_s, n_{1.x}) \cdot K_s(n_{1.x})}$$

(C.2)

Reduction factor, K_s, given in equation (C.3):

$$c_y := 11.5 \qquad\qquad c_z := 11.5$$

$$\phi_y := \frac{c_y \cdot b \cdot f_n}{v_m} = \begin{pmatrix} 39.175 \\ 38.323 \\ 38.458 \\ 37.567 \\ 37.955 \end{pmatrix} \qquad\qquad \phi_z := \frac{c_z \cdot h \cdot f_n}{v_m} = \begin{pmatrix} 48.273 \\ 47.223 \\ 47.39 \\ 46.292 \\ 46.769 \end{pmatrix}$$

Table C.1 — G and K as a function of mode shape

Mode shape	Uniform	Linear	Parabolic	Sinusoidal
G:	1/2	3/8	5/18	$4/\pi^2$
K:	1	3/2	5/3	$4/\pi$

NOTE 1 For buildings with a uniform horizontal mode shape variation and a linear vertical mode shape variation $\phi(y,z) = z/h$, $G_y = 1/2$, $G_z = 3/8$, $K_y = 1$ and $K_z = 3/2$.

NOTE 2 For chimneys with a uniform horizontal mode shape variation and a parabolic vertical mode shape variation $\phi(y,z) = z^2/h^2$, $G_y = 1/2$, $G_z = 5/18$, $K_y = 1$ and $K_z = 5/3$.

NOTE 3 For bridges with a sinusoidal horizontal mode shape variation $\phi(y,z) = \sin(\pi \cdot y/b)$, $G_y = 4/\pi^2$, $G_z = 1/2$, $K_y = 4/\pi$ and $K_z = 1$.

Table C.1 gives the factors G_y, G_z, K_y, and K_z, depending on whether linear or parabolic mode shape variation is chosen.

Mode :=
Linear
Parabolic

Linear mode shape chosen

$$\left(G_y \ \ G_z \ \ K_y \ \ K_z \right) := \begin{vmatrix} \left(\dfrac{1}{2} \quad \dfrac{3}{8} \quad 1 \quad \dfrac{3}{2} \right) & \text{if } \text{Mode} < 2 \\[2em] \left(\dfrac{1}{2} \quad \dfrac{5}{18} \quad 1 \quad \dfrac{5}{3} \right) & \text{otherwise} \end{vmatrix}$$

$$G_y = 0.5 \quad G_z = 0.375 \quad K_y = 1 \quad K_z = 1.5$$

$$K_s := \cfrac{1}{1 + \sqrt{\left[\overrightarrow{(G_y \cdot \phi_y)}\right]^2 + \left[\overrightarrow{(G_z \cdot \phi_z)}\right]^2 + \left[\dfrac{2}{\pi} \cdot \overrightarrow{(G_y \cdot \phi_y \cdot G_z \cdot \phi_z)}\right]^2}} = \begin{pmatrix} 4.38 \times 10^{-3} \\ 4.575 \times 10^{-3} \\ 4.543 \times 10^{-3} \\ 4.758 \times 10^{-3} \\ 4.663 \times 10^{-3} \end{pmatrix} \quad \text{(C.3)}$$

Turbulence length scale:

$$z_t := 200\,\mathrm{m} \quad L_t := 300\,\mathrm{m} \qquad \alpha := 0.67 + 0.05 \cdot \ln\left(\frac{z_0}{\mathrm{m}}\right) = 0.67$$

$$L := L_t \cdot \left(\frac{z_s}{z_t}\right)^{\alpha} = 55.777\,\mathrm{m} \qquad\qquad \text{(B.1)}$$

Non-dimensional frequency:

$$f_L := \frac{f_n \cdot L}{v_m} = \begin{pmatrix} 8.652 \\ 8.464 \\ 8.494 \\ 8.297 \\ 8.383 \end{pmatrix}$$

Wind power spectral density function, S_L, given in B.1(2):

$$S_L := \frac{6.8 \cdot f_L}{\left(1 + 10.2 \cdot f_L\right)^{\frac{5}{3}}} = \begin{pmatrix} 0.033 \\ 0.033 \\ 0.033 \\ 0.034 \\ 0.034 \end{pmatrix} \qquad\qquad \text{(B.2)}$$

Total logarithmic decrement of damping, $\delta = \delta_a + \delta_s$, given by the aerodynamic damping and structural damping respectively, as per F.5:

F.4(2) states: "*For cantilevered structures with a varying mass distribution, the equivalent mass per unit length, may be approximated by the average value of m over the upper third of the structure, h$_3$*"

$$h_3 := \frac{h}{3} = 9.02\,\text{m}$$

Extracting the mass of the top three floors from the ABAQUS model, yields the following mass per length:

$$m_e := \frac{526.81\,\text{tonne}}{h_3} = 5.84 \times 10^4\,\frac{\text{kg}}{\text{m}}$$

By setting equation (F.16) and (F.18) equal to each other, and solving for μ_e, we get the equivalent mass per unit area:

$$\mu_e := \frac{m_e}{b} = 2.66 \times 10^3\,\frac{\text{kg}}{\text{m}^2}$$

Logarithmic decrement of aerodynamic damping, according to (F.16) and (F.18):

$$\delta_{a.1} := \frac{c_f \cdot \rho \cdot v_m}{2 \cdot f_n \cdot \mu_e} = \begin{pmatrix} 2.191 \times 10^{-3} \\ 2.24 \times 10^{-3} \\ 2.232 \times 10^{-3} \\ 2.285 \times 10^{-3} \\ 2.262 \times 10^{-3} \end{pmatrix} \qquad \text{(F.16)}$$

$$\delta_{a.2} := \frac{c_f \cdot \rho \cdot b \cdot v_m}{2 \cdot f_n \cdot m_e} = \begin{pmatrix} 2.191 \times 10^{-3} \\ 2.24 \times 10^{-3} \\ 2.232 \times 10^{-3} \\ 2.285 \times 10^{-3} \\ 2.262 \times 10^{-3} \end{pmatrix} \quad\quad (F.18)$$

Logarithmic decrement of structural damping, average from measurements of MAL2:

$$\delta_s := \xi_n \cdot 2 \cdot \pi = \begin{pmatrix} 0.085 \\ 0.099 \\ 0.091 \\ 0.097 \\ 0.09 \end{pmatrix}$$

Thus, the total damping is:

$$\delta_t := \delta_{a.1} + \delta_s = \begin{pmatrix} 0.087 \\ 0.101 \\ 0.093 \\ 0.1 \\ 0.092 \end{pmatrix} \quad\quad (F.15)$$

Square root of resonant response can now be found, given in C.2(4):

$$R := \sqrt{\frac{\pi^2}{2} \cdot \overrightarrow{\left(\frac{S_L \cdot K_s}{\delta_t} \right)}} = \begin{pmatrix} 0.09 \\ 0.087 \\ 0.09 \\ 0.089 \\ 0.092 \end{pmatrix} \quad\quad (C.2)$$

The standard deviation can now be found by the equation given in C.4(2)

$$\mu_{ref} := \mu_e$$

$$\sigma_{a.x} := c_f \cdot \rho \cdot I_v \cdot v_m^2 \cdot R \cdot \frac{K_y \cdot K_z \cdot \Phi_1}{\mu_{ref} \cdot \Phi_1} = \begin{pmatrix} 5.614 \times 10^{-3} \\ 5.384 \times 10^{-3} \\ 5.566 \times 10^{-3} \\ 5.56 \times 10^{-3} \\ 5.697 \times 10^{-3} \end{pmatrix} \frac{m}{s^2} \qquad \text{(C.4)}$$

Peak factor, k_p, as per B.2(3):

$$T := 600s$$

$$k_p := \left[\sqrt{2 \cdot \ln\left[\overrightarrow{(f_n)} \cdot T\right]} + \frac{0.6}{\sqrt{2 \ln\left[\overrightarrow{(f_n)} \cdot T\right]}} \right] = \begin{pmatrix} 3.928 \\ 3.922 \\ 3.923 \\ 3.917 \\ 3.92 \end{pmatrix} \qquad \text{All values > 3, OK!} \qquad \text{(B.4)}$$

Peak acceleration:

$$a_{peak} := \overrightarrow{\left(\sigma_{a.x} \cdot k_p\right)} = \begin{pmatrix} 0.022 \\ 0.021 \\ 0.022 \\ 0.022 \\ 0.022 \end{pmatrix} \frac{m}{s^2}$$

Calculation of peak acceleration according to NS-EN 1-4-1991, annex C with parabolic mode shape

C.4(3) states: "*The characteristic peak accelerations are obtained by multiplying the standard deviation in C.4(2) by the peak factor in B.2(3) using the natural frequency as upcrossing frequency, i.e. $v = n_{1,x}$*"

The standard deviation is given in C.4(2):

$$\sigma_{a.x}(y,z) := c_f \cdot \rho \cdot I_v(z_s) \cdot v_m^2(z_s) \cdot R \cdot \frac{K_y \cdot K_z \cdot \Phi(y,z)^{\blacksquare}}{\mu_{ref} \cdot \Phi_{max}} \tag{C.4}$$

Known parameters:

Air density: $\qquad \rho := 1.25 \dfrac{kg}{m^3}$

First natural frequencies: $\qquad\qquad\qquad\qquad$ Structural damping values:

$$f_n := \begin{pmatrix} 2.022 \\ 1.978 \\ 1.985 \\ 1.939 \\ 1.959 \end{pmatrix} Hz \qquad\qquad\qquad \xi_n := \begin{pmatrix} 1.357 \\ 1.568 \\ 1.451 \\ 1.548 \\ 1.433 \end{pmatrix} \%$$

Structure height: $\qquad h := 27.06\,m$

Ref. height: $\qquad z_s := 0.6 \cdot h = 16.236\,m$

Fundamental mode shape according to section F.3

$\zeta := 1.0$

$\Phi_1 := \left(\dfrac{h}{h}\right)^{\zeta} = 1$

Force coefficient, c_f, given in 7.6(1):

$$c_f := c_{f.0} \cdot \psi_r \cdot \psi_\lambda{}^{\blacksquare} \qquad (7.9)$$

Note: the coefficient given in this section is meant for rectangular sections, and this building is Y-shaped. However, it has three rectangular shaped "legs" with sharp corners. This force coeffcient is therefore deemed to be the most correct to use, and it also yields the largest peak accelerations, meaning it is considered conservative.

In order to read the force coefficient of rectangular sections, values for width and depth must be decided. In this case, the width, where the wind is perpendicular to the surface, is set to 21.96m, and the depth is set to 12.75m, as seen in the figure above.

$$b := 21.96\text{m} \quad d := 12.75\text{m} \quad \frac{d}{b} = 0.581$$

Figure 7.23 — Force coefficients $c_{f,0}$ of rectangular sections with sharp corners and without free end flow

With the values given in figure 7.23, the force coefficient of rectangular sections can be found through interpolation:

$$c_{f.0} := 2 + \left(\frac{d}{b} - 0.2\right) \cdot \left[\frac{(2.35 - 2)}{(0.6 - 0.2)}\right] = 2.333$$

Reduction factor for rounded corners, according to figure 7.24:

$$\psi_r := 1.0 \qquad \text{Sharp edges}$$

Effective slenderness:

Table 7.16 — Recommended values of λ for cylinders, polygonal sections, rectangular sections, sharp edged structural sections and lattice structures

No.	Position of the structure, wind normal to the plane of the page	Effective slenderness λ
1	$z_g \geq b$ $z_g \geq 2b$ for $b \leq \ell$	For polygonal, rectangular and sharp edged sections and lattice structures: for $\ell \geq 50$ m, $\lambda = 1{,}4\ \ell/b$ or $\lambda = 70$, whichever is smaller
2	$b_1 \leq 1{,}5b$ $b_1 \leq 1{,}5b$ $b \leq \ell$ $b_0 \geq 2{,}5b$	for $\ell < 15$ m, $\lambda = 2\ \ell/b$ or $\lambda = 70$, whichever is smaller. For circular cylinders: for $\ell \geq 50$, $\lambda = 0{,}7\ \ell/b$ or $\lambda = 70$, whichever is smaller for $\ell < 15$ m, $\lambda = \ell/b$ or $\lambda = 70$, whichever is smaller
3	$\frac{\ell}{2}$ $\frac{b}{2}$ b ℓ	For intermediate values of ℓ, linear interpolation should be used
4	b ℓ ℓ b $b_1 \geq 2{,}5b$ b ℓ $z_g \geq 2b$	for $\ell \geq 50$ m, $\lambda = 0{,}7\ \ell/b$ or $\lambda = 70$, whichever is larger for $\ell < 15$ m, $\lambda = \ell/b$ or $\lambda = 70$, whichever is larger For intermediate values of ℓ, linear interpolation should be used

Case number two from table 7.16:

$$l := h$$

$$\lambda_{upper} := 1.4 \cdot \frac{l}{b} = 1.725 \qquad\qquad \lambda_{lower} := 2 \cdot \frac{l}{b} = 2.464$$

Interpolating between values:

$$\lambda := \lambda_{lower} - \frac{\left(\lambda_{lower} - \lambda_{upper}\right) \cdot (l - 15m)}{50m - 15m} = 2.21$$

Figure 7.36 — Indicative values of the end-effect factor ψ_λ as a function of solidity ratio φ versus slenderness λ

With φ=1.0 for this structure, the value for ψ_λ can be read from figure 7.36:

$$\psi_\lambda := 0.62$$

The force coefficient becomes:

$$c_f := c_{f.0} \cdot \psi_r \cdot \psi_\lambda = 1.446 \tag{7.9}$$

Turbulence intencity I_v and mean wind velocity v_m at height z_s, according to 4.4(1):

$$c_{dir} := 1.0 \quad c_{season} := 1.0 \quad c_{alt} := 1.0 \quad c_{prob} := 1.0 \qquad \text{NA.4.2(2)P}$$

The return period in NS-EN 1-4-1991, is usually set to 50 years. Since the measurements only takes place in one day, the return period must be lowered. The return period is set to one year to represent best the probability of faster gusts of wind on the day of measuring.

To approximate the probability, p, the Poisson ratio is used.

Return period for one year:

$$K := 0.2 \qquad n := 0.5 \qquad\qquad\qquad\qquad \text{NA.4.2(2)P}$$

$$p(x) := 1 - \exp\left(\frac{-1}{x}\right)$$

$$p := p(1) = 0.632$$

$$c_{prob} := \left(\frac{1 - K \cdot \ln(-\ln(1 - p))}{1 - K \cdot \ln(-\ln(0.98))}\right)^n = 0.749 \qquad\qquad (4.2)$$

$$v_{b.0} := 26 \frac{m}{s} \qquad\qquad\qquad\qquad \text{Table NA.4(901.1)}$$

Basic wind:

$$v_b := c_{dir} \cdot c_{season} \cdot c_{alt} \cdot c_{prob} \cdot v_{b.0} = 19.486 \frac{m}{s} \qquad\qquad (NA.4.1)$$

Turbulence category 4, table NA.4.1:

$$k_r := 0.24 \qquad z_0 := 1.0m \qquad z_{min} := 16m$$

$$k_l := 1.0 \qquad c_0 := 1.0 \qquad\qquad\qquad\qquad 4.3.3$$

$$I_v := \frac{k_l}{c_0 \cdot \ln\left(\frac{z_s}{z_0}\right)} = 0.359 \qquad\qquad (4.7)$$

Mean wind velocity:

$$c_r := k_r \cdot \ln\left(\frac{z_s}{z_0}\right) = 0.669 \qquad\qquad (4.4)$$

$$v_m := c_r \cdot c_0 \cdot v_b = 13.035 \frac{m}{s} \qquad\qquad (4.3)$$

Square root of the resonant response, R^2, given in C.2(4):

$$R := \sqrt{\frac{\pi^2}{2 \cdot \delta} \cdot S_L(z_s, n_{1.x}) \cdot K_s(n_{1.x})} \qquad\blacksquare$$

(C.2)

Reduction factor, K_s, given in equation (C.3):

$$c_y := 11.5 \qquad\qquad c_z := 11.5$$

$$\phi_y := \frac{c_y \cdot b \cdot f_n}{v_m} = \begin{pmatrix} 39.175 \\ 38.323 \\ 38.458 \\ 37.567 \\ 37.955 \end{pmatrix} \qquad\qquad \phi_z := \frac{c_z \cdot h \cdot f_n}{v_m} = \begin{pmatrix} 48.273 \\ 47.223 \\ 47.39 \\ 46.292 \\ 46.769 \end{pmatrix}$$

Table C.1 — G and K as a function of mode shape

Mode shape	Uniform	Linear	Parabolic	Sinusoidal
G:	1/2	3/8	5/18	$4/\pi^2$
K:	1	3/2	5/3	$4/\pi$

NOTE 1   For buildings with a uniform horizontal mode shape variation and a linear vertical mode shape variation $\phi(y,z) = z/h$, $G_y = 1/2$, $G_z = 3/8$, $K_y = 1$ and $K_z = 3/2$.

NOTE 2   For chimneys with a uniform horizontal mode shape variation and a parabolic vertical mode shape variation $\phi(y,z) = z^2/h^2$, $G_y = 1/2$, $G_z = 5/18$, $K_y = 1$ and $K_z = 5/3$.

NOTE 3   For bridges with a sinusoidal horizontal mode shape variation $\phi(y,z) = \sin(\pi \cdot y/b)$, $G_y = 4/\pi^2$, $G_z = 1/2$, $K_y = 4/\pi$ and $K_z = 1$.

Table C.1 gives the factors G_y, G_z, K_y, and K_z, depending on whether linear or parabolic mode shape variation is chosen.

Mode :=
| Linear |
| Parabolic |

Parabolic mode shape chosen

$$\begin{pmatrix} G_y & G_z & K_y & K_z \end{pmatrix} := \begin{vmatrix} \left(\dfrac{1}{2} & \dfrac{3}{8} & 1 & \dfrac{3}{2} \right) & \text{if } Mode < 2 \\[2ex] \left(\dfrac{1}{2} & \dfrac{5}{18} & 1 & \dfrac{5}{3} \right) & \text{otherwise} \end{vmatrix}$$

$$G_y = 0.5 \quad G_z = 0.278 \quad K_y = 1 \quad K_z = 1.667$$

$$K_s := \frac{1}{1 + \sqrt{\left[\overrightarrow{(G_y \cdot \phi_y)}\right]^2 + \left[\overrightarrow{(G_z \cdot \phi_z)}\right]^2 + \left[\frac{2}{\pi} \cdot \overrightarrow{(G_y \cdot \phi_y \cdot G_z \cdot \phi_z)}\right]^2}} = \begin{pmatrix} 5.886 \times 10^{-3} \\ 6.147 \times 10^{-3} \\ 6.104 \times 10^{-3} \\ 6.392 \times 10^{-3} \\ 6.264 \times 10^{-3} \end{pmatrix} \quad (C.3)$$

Turbulence length scale:

$$z_t := 200 \, m \quad L_t := 300 \, m \quad \alpha := 0.67 + 0.05 \cdot \ln\left(\frac{z_0}{m}\right) = 0.67$$

$$L := L_t \cdot \left(\frac{z_s}{z_t}\right)^\alpha = 55.777 \, m \quad (B.1)$$

Non-dimensional frequency:

$$f_L := \frac{f_n \cdot L}{v_m} = \begin{pmatrix} 8.652 \\ 8.464 \\ 8.494 \\ 8.297 \\ 8.383 \end{pmatrix}$$

Wind power spectral density function, S_L, given in B.1(2):

$$S_L := \frac{6.8 \cdot f_L}{\left(1 + 10.2 \cdot f_L\right)^{\frac{5}{3}}} = \begin{pmatrix} 0.033 \\ 0.033 \\ 0.033 \\ 0.034 \\ 0.034 \end{pmatrix} \quad (B.2)$$

Total logarithmic decrement of damping, $\delta = \delta_a + \delta_s$, given by the aerodynamic damping and structural damping respectively, as per F.5:

F.4(2) states: "*For cantilevered structures with a varying mass distribution, the equivalent mass per unit length, may be approximated by the average value of m over the upper third of the structure, h_3*"

$$h_3 := \frac{h}{3} = 9.02\,m$$

Extracting the mass of the top three floors from the ABAQUS model, yields the following mass per length:

$$m_e := \frac{526.81\,tonne}{h_3} = 5.84 \times 10^4 \frac{kg}{m}$$

By setting equation (F.16) and (F.18) equal to each other, and solving for μ_e, we get the equivalent mass per unit area:

$$\mu_e := \frac{m_e}{b} = 2.66 \times 10^3 \frac{kg}{m^2}$$

Logarithmic decrement of aerodynamic damping, according to (F.16) and (F.18):

$$\delta_{a.1} := \frac{c_f \cdot \rho \cdot v_m}{2 \cdot f_n \cdot \mu_e} = \begin{pmatrix} 2.191 \times 10^{-3} \\ 2.24 \times 10^{-3} \\ 2.232 \times 10^{-3} \\ 2.285 \times 10^{-3} \\ 2.262 \times 10^{-3} \end{pmatrix} \tag{F.16}$$

$$\delta_{a.2} := \frac{c_f \cdot \rho \cdot b \cdot v_m}{2 \cdot f_n \cdot m_e} = \begin{pmatrix} 2.191 \times 10^{-3} \\ 2.24 \times 10^{-3} \\ 2.232 \times 10^{-3} \\ 2.285 \times 10^{-3} \\ 2.262 \times 10^{-3} \end{pmatrix}$$ (F.18)

Logarithmic decrement of structural damping, average from measurements of MAL2:

$$\delta_s := \xi_n \cdot 2 \cdot \pi = \begin{pmatrix} 0.085 \\ 0.099 \\ 0.091 \\ 0.097 \\ 0.09 \end{pmatrix}$$

Thus, the total damping is:

$$\delta_t := \delta_{a.1} + \delta_s = \begin{pmatrix} 0.087 \\ 0.101 \\ 0.093 \\ 0.1 \\ 0.092 \end{pmatrix}$$ (F.15)

Square root of resonant response can now be found, given in C.2(4):

$$R := \sqrt{\frac{\pi^2}{2} \cdot \overrightarrow{\left(\frac{S_L \cdot K_s}{\delta_t}\right)}} = \begin{pmatrix} 0.105 \\ 0.1 \\ 0.104 \\ 0.104 \\ 0.106 \end{pmatrix}$$ (C.2)

The standard deviation can now be found by the equation given in C.4(2)

$$\mu_{ref} := \mu_e$$

$$\sigma_{a.x} := c_f \cdot \rho \cdot I_v \cdot v_m^{\ 2} \cdot R \cdot \frac{K_y \cdot K_z \cdot \Phi_1}{\mu_{ref} \cdot \Phi_1} = \begin{pmatrix} 7.232 \times 10^{-3} \\ 6.934 \times 10^{-3} \\ 7.169 \times 10^{-3} \\ 7.16 \times 10^{-3} \\ 7.337 \times 10^{-3} \end{pmatrix} \frac{m}{s^2} \qquad (C.4)$$

Peak factor, k_p, as per B.2(3):

$$T := 600s$$

$$k_p := \left[\sqrt{2 \cdot \ln\left[\overrightarrow{\left(f_n \right)} \cdot T \right]} + \frac{0.6}{\sqrt{2 \ln\left[\overrightarrow{\left(f_n \right)} \cdot T \right]}} \right] = \begin{pmatrix} 3.928 \\ 3.922 \\ 3.923 \\ 3.917 \\ 3.92 \end{pmatrix} \qquad \text{All values > 3, OK!} \qquad (B.4)$$

Peak acceleration:

$$a_{peak} := \overrightarrow{\left(\sigma_{a.x} \cdot k_p \right)} = \begin{pmatrix} 0.028 \\ 0.027 \\ 0.028 \\ 0.028 \\ 0.029 \end{pmatrix} \frac{m}{s^2}$$

Appendix H

Explanation of essential MATLAB scripts

This appendix briefly explains the essential MATLAB scripts used to obtain the results of this thesis. Each headline refers to the name of the script, which can be found in a digital appendix delivered to the Department of Structural Engineering at NTNU.

MoholtMeasVert2.m

This script was used to run the DD-SSI on the data obtained from the vertical measurements. In this script, the data processing described in chapter 5 is performed on the .mat-files of the measurements. It uses a script made by Postdoc at NTNU Knut Andreas Kvåle to perform the DD-SSI and a script called "stabPlot3" to plot the stabilization diagrams. A few lines of code were added to this script to extract the data of interest from the stable poles in a simple fashion. The data contained the model order, frequency and damping ratio.

FilteringSpuriousStablePoles.m

This script was used for two purposes: to filter the spurious stable poles from the stabilization diagrams and two find the mean values and standard deviations of natural frequencies and damping for one six hour recording. The first step was to filter the poles. This was done by choosing the frequencies that were visibly related to a mode. When the correct frequencies were chosen, the spurious stable poles were filtered out with the following criteria:

$$\omega_i - 0.1 < \omega_n < \omega_i + 0.1 \qquad \text{(H.1)}$$

where ω_n is the frequency of each individual pole and ω_i is the frequency related to each mode set from visual inspection of the stabilization diagram. This filtering process only left poles visually in line with each other in the stabilization diagram. The limit ± 0.1 was chosen from visual inspection of the stabilization diagram.

After the spurious poles were filtered out, the mean and standard deviation of all the poles' natural frequencies and damping ratios was found for each six hour recording. The final step to get the averaged frequencies and damping ratios presented in this thesis, was by taking the mean of the data obtained from all recordings. The following list describes the process:

1. Filter the spurious poles. All irrelevant poles are discarded by the criteria in (H.1).

2. Finding mean value and standard deviation of the frequencies and damping ratios of every pole for one six hour recording.

3. Finding the mean value of the mean values and standard deviations obtained in step 2.

MoholtMeas.m

This script was used to run the Cov-SSI on the data obtained from the in-plane measurements on the 7th and 9th floor. In this script, the data processing described in chapter 5 is performed on the .mat-files of the measurements. The script is based on a script made for the measurements of Mjøstårnet. This script's main purpose was to extract and plot the in-plane mode shapes displayed in section 7.2.

PeakAcceleration.m

This script was used to find the peak accelerations from the measurement data. The data processing described in chapter 5 was also performed in this script.

Final remarks

In order to run these scripts, some additional functions are needed. For MoholtMeas-Vert2.m, the Department provided this set of support functions. For MoholtMeas.m the functions needed can be found by googling "Ooma Toolbox".

Rolf Bjordal, Henrik Rekdal Eidheim

Master's thesis

NTNU
Norwegian University of
Science and Technology